Contributions to the FEL'99 Conference, August 23-28, 1999 in Hamburg, Germany

Contents

Coherent Effects of a Macro Bunch in an Undulator

M.Dohlus, A.Kabel, T.Limberg
Deutsches Elektronen Synchrotron DESY, Notkestr. 85, D-22607 Hamburg

Abstract

The longitudinal radiative force of an electron bunch moving in an undulator has been investigated in [1] assuming an 1D density distribution. To obtain the contribution of pure curvature effects and to avoid singular fields, the 1D linear motion field was subtracted. To relate these results to the 3D case we present analytical and numerical field calculations using the field solver of TRAFIC4. The 1D and 3D cases have been calculated in the transient regime, the steady state regime and the steady state regime averaged over one undulator period for the 1GeV parameter set of the TESLA FEL.

1. Introduction

There are 2 effects caused by the macroscopic charge distribution in an undulator which increase the energy spread and the emittance of a bunch and may therefore disturb the FEL process: one is caused by the fields due to the undulator motion [1, 2, this paper], the other is related to the finite conductivity and roughness of the beam pipe [3,4,5]. The fields of the macro bunch undulator motion have been considered earlier, using the model of a one dimensional bunch excluding singular field contributions [1], and by the model of a rectangular bunch in circular motion [2]. In this paper we take into account all field contributions for one and three dimensional Gaussian charge distributions. The 1D theory considers a transverse observer offset while the 3D theory is valid for observation points without offset. It is confirmed, that the effect of the 1D singularity can be described by the superposition of the field of a 1D bunch in linear motion and a smooth non singular field [1]. The longitudinal and transverse component show a strong dependency on both the longitudinal position in the undulator and the transverse offset. In comparison to this, the field averaged over one undulator period is small and depends only weakly on the offset of the observer particle. Our analytical results agree well with the fully 3D computations using the TRAFIC4 field solver. Additionally we present calculations of the transient process of a bunch which enters the undulator. Although the local field develops its strong spatial dependency after one or few undulator periods, the one period averaged field is far from the steady state condition until the core of the *retarded* bunch is in the undulator.

2. Theory

The motion of charged particles in the magnetic field of an undulator

$$\mathbf{H}(s) = K\frac{mc_0^2}{eZ_0}\frac{2\pi}{\lambda_s}\frac{\partial s}{\partial z}\cos\left(\frac{2\pi}{\lambda_s}s\right)\mathbf{e}_x \approx K\frac{mc_0^2}{eZ_0}\frac{2\pi}{\lambda_z}\cos\left(\frac{2\pi}{\lambda_z}z\right)\mathbf{e}_x \qquad (1)$$

is described by the path

$$\mathbf{r}_u(s) = \frac{u}{k_s}\left(1-\cos(k_s s)\right)\mathbf{e}_y + \left(Us + \left(\frac{u}{2}\right)^2\frac{\sin(2k_s s)}{2k_s}\right)\mathbf{e}_z + O\left(u^4\right), \qquad (2)$$

with K the undulator parameter, λ_s the period length of the path, λ_z the undulator period, $u = K/\gamma\beta$ the maximal angle of the undulator path to $\mathbf{e}_z$ the undulator axis, $U = 1-(u/2)^2$ the relation between the z-period and the path period and $k_s = 2\pi/\lambda_s$. We assume a Gaussian line charge density $\lambda(s-vt)$ for one dimensional calculations with $\lambda(s) = g(s/\sigma)q/\sigma$, $v = \beta c_0$ the bunch velocity, q the bunch charge, σ

the RMS bunch length and $g(x)$ the Gaussian normal distribution. The charge density used for three dimensional calculations is

$$\rho(\mathbf{r}=\mathbf{r}_u(s)+x\mathbf{e}_x+y\mathbf{e}_y,t)=\lambda(s-vt)\frac{g(x/\sigma_r)}{\sigma_r}\frac{g(y/\sigma_r)}{\sigma_r}\frac{1}{\mathbf{e}_z\cdot\partial_s\mathbf{r}_u}, \qquad (3)$$

with σ_r the RMS bunch radius. The longitudinal electric field E is calculated for a test particle at the location $\mathbf{r}_t(S=vt)=\mathbf{r}_u(S+\delta S)+y\mathbf{e}_y$ with δS the longitudinal offset to the bunch center, y the transverse offset and $\mathbf{e}_t=\partial_S\mathbf{r}_t$ the longitudinal direction. The longitudinal electric field can be expressed by the scalar and vector potential Θ, $\mathbf{A}$ as

$$E=\mathbf{E}\cdot\mathbf{e}_t=-\left(\nabla\Theta+\dot{\mathbf{A}}\right)\cdot\mathbf{e}_t=-\frac{d\Theta}{dvt}+\frac{\partial}{\partial vt}\left(\Theta-\mathbf{A}\cdot\mathbf{v}\right). \qquad (4)$$

The term $E_1=-d\Theta/dvt$ describes the field that is needed to change the potential energy. The mean value of E_1 vanishes because the scalar potential in the undulator is a periodic function. The second term, which is not conservative, is singular for one dimensional source distributions. To obtain a finite and smooth distribution E_2 we divide the field artificially into

$$E=\underbrace{-\frac{d\Theta}{dvt}}_{E_1}+\underbrace{\frac{\partial}{\partial vt}\left(\Theta-\frac{\Theta_{LM}}{\gamma^2}-\mathbf{A}\cdot\mathbf{v}\right)}_{E_2}+\underbrace{\frac{\partial}{\partial vt}\frac{\Theta_{LM}}{\gamma^2}}_{E_3}, \qquad (5)$$

with Θ_{LM} the potential of a bunch in linear motion. Θ_{LM} is calculated in the same way as Θ, but with the source path $\mathbf{r}_{LM}(s)=s\mathbf{e}_z$ and the observer position $\mathbf{r}_{t,LM}(S)=\mathbf{r}_{LM}(S+\delta S)+y\mathbf{e}_y$. The field of a line charge density is given by the one dimensional integration of the retarded sources:

$$E_1=\frac{-1}{4\pi\varepsilon_0}\int_{-\infty}^{\infty}\frac{\partial}{\partial R}\left(\frac{\lambda(s+\delta S+\beta R)}{R}\right)\frac{\partial R}{\partial S}ds \qquad (6a)$$

$$\begin{aligned}E_2=&\frac{-\beta^2}{4\pi\varepsilon_0}\int_{-\infty}^{\infty}\frac{\lambda'(s+\delta S+\beta R)}{R_{LM}}\left(1-\mathbf{e}(s_0)\cdot\mathbf{e}(s_1)\right)ds\\&-\frac{1}{4\pi\varepsilon_0\gamma^2}\int_{-\infty}^{\infty}\frac{\lambda'(s+\delta S+\beta R)-\lambda'(s+\delta S+\beta R_{LM})}{R_{LM}}ds\\&+\frac{1}{4\pi\varepsilon_0}\int_{-\infty}^{\infty}\lambda'(s+\delta S+\beta R)\left(\frac{1}{R_{LM}}-\frac{1}{R}\right)\left(1-\beta^2\mathbf{e}(s_0)\cdot\mathbf{e}(s_1)\right)ds\end{aligned} \qquad (6b)$$

$$E_3=\frac{-1}{4\pi\varepsilon_0\gamma^2}\int_{-\infty}^{\infty}\frac{\lambda'(s+\delta S+\beta R_{LM})}{R_{LM}}ds \qquad (6c)$$

with $s_0 = S + \delta S$, $s_1 = S + \delta S + s$, $\mathbf{R} = \mathbf{r}_t(S) - \mathbf{r}_u(S + \delta S + s)$, $R = \|\mathbf{R}\|$, $\mathbf{n} = \frac{\mathbf{R}}{R}$, $R_{LM} = \sqrt{s^2 + y^2}$, $\mathbf{e}(s) = \partial_s \mathbf{r}(s)$. The last term of Eq. 6b is of the order $qK^2\left(2 + K^2\right)/\left(\gamma^4 16\pi\varepsilon_0\sigma^2\right)$ and therefore neglected in the following. The distance R between source and observer is in first order approximated by $R_0 = \sqrt{(Us)^2 + y^2}$. For the integration of Eq. 6 for macro bunches (bunch length >> photon wavelength) we take into account the corrections $\delta R = R - R_0$ and approximate all integrands by their first order Taylor expansion with respect to δR:

$$E_1 = \frac{-1}{4\pi\varepsilon_0}\int_{-\infty}^{\infty} \frac{\partial}{\partial R_0}\left(\frac{\lambda_0}{R_0}\right)\frac{\partial \delta R}{\partial S}\,ds, \tag{7a}$$

$$\begin{aligned} E_2 = {} & \frac{-1}{4\pi\varepsilon_0}\int_{-\infty}^{\infty}\left\{\beta^2\frac{\lambda_0'}{R_{LM}}\left(1 - \mathbf{e}(s_0)\cdot\mathbf{e}(s_1)\right) + \frac{\lambda_0' - \lambda_{LM}'}{\gamma^2 R_{LM}}\right\}ds \\ & - \frac{1}{4\pi\varepsilon_0}\int_{-\infty}^{\infty}\frac{\lambda_0''\beta\delta R}{R_{LM}}\left(1 - \beta^2\mathbf{e}(s_0)\cdot\mathbf{e}(s_1)\right)ds \end{aligned} \tag{7b}$$

with $\lambda_0 = \lambda(s + \delta S + \beta R_0)$, $\lambda_{LM} = \lambda(s + \delta S + \beta R_{LM})$ and

$$\begin{aligned} \delta R = {} & \frac{\cos(k_s s_1) - \cos(k_s s_0)}{R_0 k_s}uy - \frac{1}{2R_0}\left[\frac{\cos(k_s s_1) - \cos(k_s s_0)}{R_0 k_s}uy\right]^2 \\ & + \left[\frac{\left(\cos(k_s s_1) - \cos(k_s s_0)\right)^2 + \frac{1}{4}Uk_s s\left(\sin(2k_s s_1) - \sin(2k_s s_0)\right)}{R_0 k_s}\right]\frac{u^2}{2k_s} + O\left(u^3\right) \end{aligned} \tag{8a}$$

$$1 - \mathbf{e}(s_0)\cdot\mathbf{e}(s_1) = \tfrac{1}{2}u^2\left(\sin\left(k_s s_1\right) - \sin\left(k_s s_0\right)\right)^2 + O(u^4). \tag{8b}$$

2.1 Mid Offset Range Approximation

The mid offset range approximation estimates δR by the first term of Eq. 8a and neglects second order terms of *y*. Therefore it is valid for $u/k_s << |y| << \sqrt{\sigma\lambda_u}$. Although the mean value of E_1 (with respect to time) vanishes, it causes a large oscillating contribution for particles with an offset of the order of the bunch length:

$$E_1 = \frac{uy}{4\pi\varepsilon_0}\left[f_{1s}(\delta S, y)\sin\left(k_s(S + \delta S)\right) + f_{1c}(\delta S, y)\cos\left(k_s(S + \delta S)\right)\right] \tag{9a}$$

$$f_{1s}(\delta S, y) = \int_{-\infty}^{\infty}\frac{\partial}{\partial R_0}\left(\frac{\lambda_0}{R_0}\right)\frac{\cos(k_s s) - 1}{R_0}\,ds \tag{9b}$$

$$f_{1c}(\delta S, y) = \int_{-\infty}^{\infty}\frac{\partial}{\partial R_0}\left(\frac{\lambda_0}{R_0}\right)\frac{\sin(k_s s)}{R_0}\,ds \tag{9c}$$

The offset dependency of E_2 is almost negligible in comparison to E_1. Therefore we specify here only the offset independent part of this term and neglect the positive part of the integration range (which is of the order of $qK^2/\left(\gamma^4 16\pi\varepsilon_0\sigma^2\right)$):

$$E_2 = \frac{qK^2}{4\pi\varepsilon_0\gamma^2\sigma^2}\left[g_1(\delta S) + g_{1s}(\delta S)\sin\left(2k_s(S+\delta S)\right) + g_{1c}(\delta S)\cos\left(2k_s(S+\delta S)\right) + g_2(\delta S)\right] \tag{10a}$$

$$g_1(\delta S) = \int_{-\infty}^{0} \frac{g'\left(x+\delta S/\sigma\right)}{x}\sin^2\left(\frac{\omega \mathrm{x}}{2}\right)dx, \tag{10b}$$

$$g_{1s}(\delta S) = \int_{-\infty}^{0} \frac{-g'\left(x+\delta S/\sigma\right)}{x}\sin^2\left(\frac{\omega \mathrm{x}}{2}\right)\sin\left(\omega \mathrm{x}\right)dx, \tag{10c}$$

$$g_{1c}(\delta S) = \int_{-\infty}^{0} \frac{g'\left(x+\delta S/\sigma\right)}{x}\sin^2\left(\frac{\omega \mathrm{x}}{2}\right)\cos\left(\omega \mathrm{x}\right)dx, \tag{10d}$$

$$g_2(\delta S) = \int_{-\infty}^{0} \frac{g'\left(x+\delta S/\sigma\right) - g'\left(x/(1+0.5K^2)+\delta S/\sigma\right)}{xK^2}ds, \tag{10e}$$

with $\omega = \dfrac{2k_s\sigma\gamma^2}{1+K^2/2}$. The validity of this approach is demonstrated in section 3 for the case of the TESLA FEL undulator.

2.2 Approximation for the Time Averaged Field of a 3D Beam

The time averaged field $\langle E\rangle$ of a 3D beam (Eq. 3) is the sum of the time averaged term $\langle E_2\rangle$ and the time independent field E_3. For the calculation of $\langle E_2\rangle$ we make the assumption that the field is independent of the transverse offset and estimate δR by the third term of equation 8a:

$$\langle E_2\rangle = \frac{qK^2}{4\pi\varepsilon_0\gamma^2\sigma^2}\left[g_1(\delta S) + g_2(\delta S) + \frac{g_3(\delta S) + K^2 g_4(\delta S)}{\sigma k_s\beta\gamma^2}\right], \tag{11a}$$

$$g_3(\delta S) = \int_{-\infty}^{0} \frac{\cos(x\omega)-1}{2x\omega}\frac{g''(x+\delta S/\sigma)}{x}dx, \tag{11b}$$

$$g_4(\delta S) = \int_{-\infty}^{0} \left\{\frac{8\cos(x\omega) - 2\cos(2x\omega) - 6}{x\omega} + \sin(2x\omega) - 2\sin(x\omega)\right\}\frac{g''\left(x+\delta S/\sigma\right)}{32x}ds. \tag{11c}$$

This equation differs from the time averaged field calculated with the mid range approximation (10) by the terms $g_3(\delta S)$ and $g_4(\delta S)$. Therefore the assumption of a negligible offset dependency is only consistent

under the condition $1+K^2 << \sigma k_s \gamma^2$ (weak influence of g_3 and g_4). The linear motion contribution E_3 for a particle without transverse offset is

$$E_3 = \frac{-q}{4\pi\varepsilon_0 \gamma \sigma_r \sigma} \int_{-\infty}^{\infty} g'(x + \delta S/\sigma) \mathrm{F}(x\gamma\sigma/\sigma_r) dx \,, \tag{12a}$$

$$F(\xi) = \sqrt{\frac{\pi}{2}} \exp\left(\frac{\xi^2}{2}\right)\left(1 - \mathrm{erf}\left(\frac{|\xi|}{\sqrt{2}}\right)\right) \approx \frac{1}{\sqrt{1+\xi^2}} \text{ for } |\xi| >> 1. \tag{12b}$$

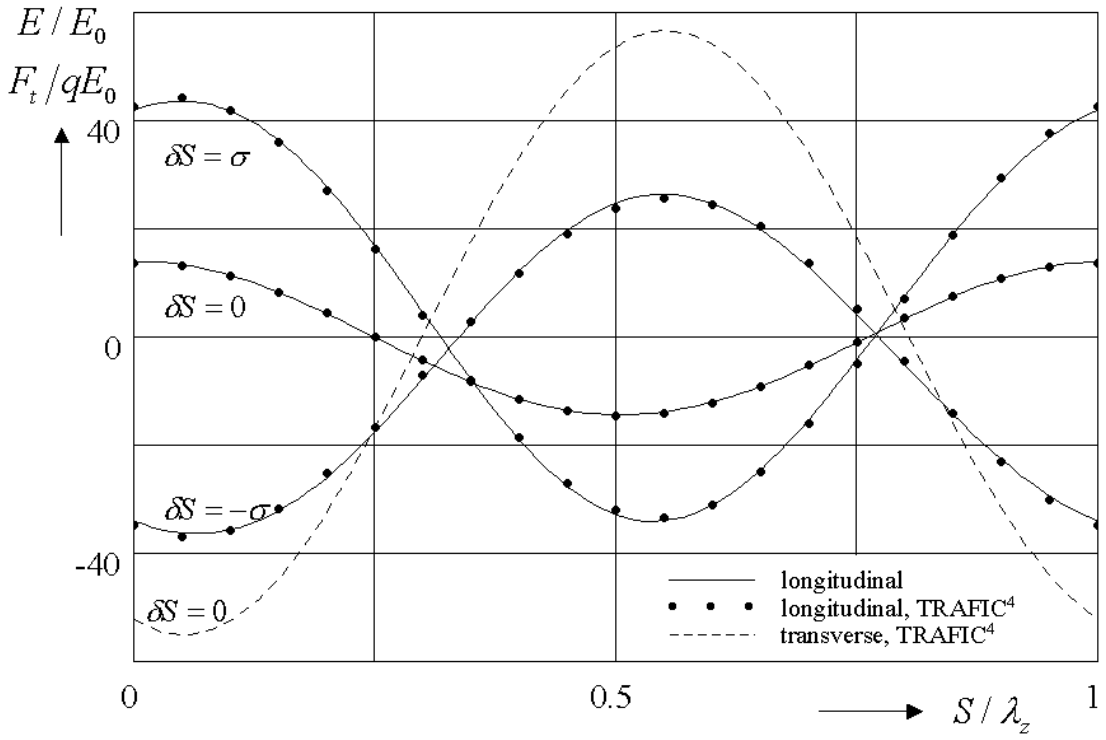

Fig. 1: Longitudinal electric field for test particles with y = 50µm and δS = 0, -σ, +σ and transverse component ($\partial_S \mathbf{r}_t \times \mathbf{e}_x$) of the Lorentz force for a test particle with y = 50µm, δS = 0.

3. Calculations

The following calculations were carried out for the parameters of the 1GeV parameter set of the TESLA FEL (K = 1.27, λ_z = 2.73cm, γ= 1957, σ = 50µm) with the formulas described above and by the TRAFIC4 field solver [6] which integrates Eq. 4 numerically without any approximations. All fields are normalized to $E_0 = q/4\pi\varepsilon_0\gamma^2\sigma^2$ which is 939 V/m for a bunch charge of 1 nC. We distinguish between the steady state regime that assumes an infinite undulator and the transient regime.

	$eE_{\mathrm{mean}} L_u / \gamma mc_0^2$	$eE_{\mathrm{rms}} L_u / \gamma mc_0^2$
1D approach without E_3, [1]	$-5.14\cdot10^{-6}$	$3.59\cdot10^{-5}$
1D approach without E_3, Eq. 11	$-5.11\cdot10^{-6}$	$3.57\cdot10^{-5}$
round beam, TRAFIC4	$-5.16\cdot10^{-6}$	$10.0\cdot10^{-5}$

Table 1: The mean energy offset and the rms energy spread for the parameters of the 1GeV parameter set of the TESLA FEL (K = 1.27, λ_z = 2.73cm, γ= 1957, σ = 50µm, length=27m).

3.1 Steady State

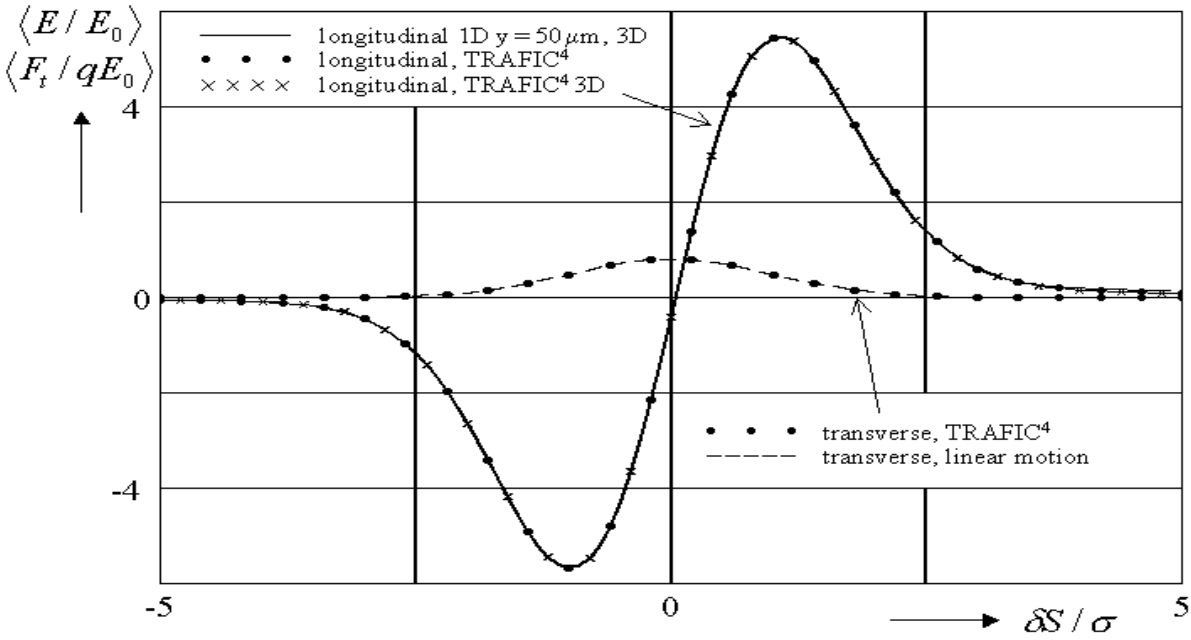

Fig. 2: Longitudinal electric field and transverse component ($\partial_S \mathbf{r}_t \times \mathbf{e}_x$) of the Lorentz force averaged over one undulator period. The comparison is between the 1D longitudinal field for a test particle with y = 50μm (calculated by mid range approach and TRAFIC4) and the 3D longitudinal field (calculated by Eq. 11&12 and TRAFIC4). Further the averaged transverse field (1D, y = 50μm) is compared with the linear motion field.

The time dependent field of particles with a transverse offset y = 50μm and δS = 0, $-\sigma$, $+\sigma$ is shown in Fig. 1. The slight deviation between the mid range approximation and the TRAFIC4 points is essentially caused by neglecting the third term of Eq. (8a) in the factor $\partial_S \delta R$ which is needed for the calculation of E_1 by Eq. (7b). The major contribution to the strong oscillation of $E(S, \delta S = \text{const})$ comes from the variation of the potential energy $-d\Theta/dS$. It was proposed in [2] to estimate this oscillation by a circular motion model with the local curvature radius. In the given case this would overestimate the amplitude of the $+\sigma$ particle by a factor of 3/2. The transverse component (perpendicular to the magnetic field) of the Lorentz force is the space charge force of a beam in linear motion superimposed by the centrifugal space charge force. Averaged over one undulator period the strong oscillations cancel (see Fig. **2**). The averaged longitudinal fields for an observer offset y = 50μm and a round beam σ_r = 50 μm without offset calculated by this theory are plotted on the same line. This result is also in good agreement with the fully three dimensional calculation of TRAFIC4. The deviation between $\langle E_2 \rangle$ calculated by Eq. 11 and $\langle E - E_3 \rangle$ calculated by TRAFIC4 (3D) is less then $0.05 \cdot E_0$ for all positions in the bunch ($|\delta S| < 5\sigma$, $|y| < 5\sigma_r$). This confirms that $\langle E_2 \rangle$ is really insensitive to the transverse position of the test particle. The averaged transverse component of the Lorentz force is almost identical to the transverse field of a bunch in longitudinal motion. The mean energy offset and the rms energy spread are listed in Tab. 1 (undulator length L_u = 27 m).

3.2 Transient

The transient behavior of the longitudinal E-field of a 1D bunch that enters an undulator has been calculated by TRAFIC4. Therefore it is assumed that the magnetic field (Eq.1) vanishes for $z < 0$ and the path (Eq. 2) is linear for negative path coordinates: $\mathbf{r}_u(s < 0) = -s\,\mathbf{e}_z$. The field observed by test particles with a transverse

offset y = 50μm and δS = 0, $-\sigma$, $+\sigma$ is shown in Fig. **3**. The instantaneous field $E(S,\delta S)$ (left diagram) after half an undulator period looks almost like the steady state field in Fig. 1. Nevertheless the averaged field $\langle E(S,\delta S)\rangle = 1/\lambda_s \int_{S-\lambda_s/2}^{S-\lambda_s/2} E(\xi,\delta S)\, d\xi$ (right diagram) needs several hundred undulator periods to approach the steady state condition as calculated in Fig. **2**.

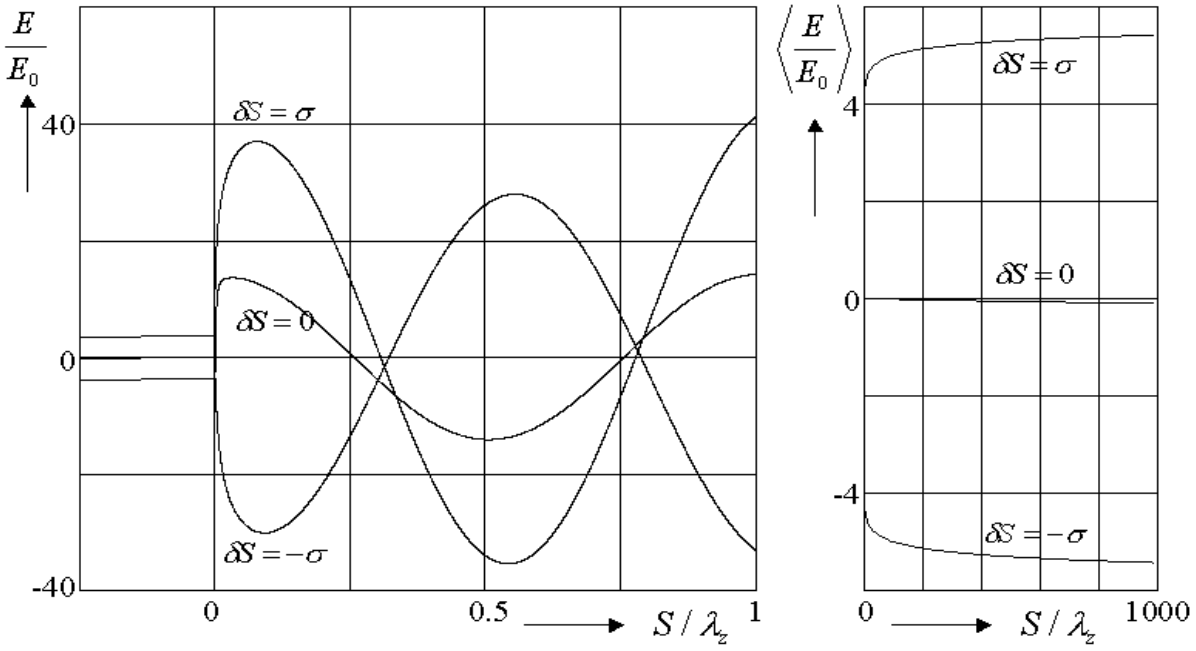

Fig. 3: Transient longitudinal electric field for test particles with y = 50μm and δS = 0, $-\sigma$, $+\sigma$. The left picture shows the field in the first undulator period (compare Fig. 1). The right picture shows the averaged field $\langle E\rangle = 1/\lambda_s \int_{S-\lambda_s/2}^{S+\lambda_s/2} E(\xi) d\xi$ for 1000 periods.

4. Conclusion

The longitudinal as well as the transverse component of the Lorentz force caused by a macrobunch in the TESLA FEL undulator at 1GeV can be one to two orders larger than the forces of the same bunch in linear motion. Averaged versus one undulator period these components are of the same order as for linear motion.

Acknowledgement

We wish to thank E.L. Saldin, E.A. Schneidmiller and J. Rossbach for many useful discussions.

References

[1] E.L.Saldin, E.A.Schneidmiller, M.V.Yurkov: Radiative Interaction of an Electron Moving in an Undulator. TESLA-FEL 97-08, October 1997.

[2] B.Carlsten, J.Goldstein: Emittance Growth of a Short Electron Bunch in Circular Motion. Nuclear Instruments and Methods in Physics Research, A 393, p 490-493, 1997.

[3] K.Bane, C.Ng, A.Chao: Estimate of the Impedance due to Wall Surface Roughness. SLAC-PUB-7514, 1997.

[4] G.Stupakov: Impedance of Small Obstacles and Rough Surfaces. SLAC-PUB-7908, Aug. 1998.

[5] M.Dohlus, R.Lorentz, Th.Kamps, H.Schlarb, R.Wanzenberg: Estimation of Longitudinal Wakefield Effects in the TESLA-TTF FEL Undulator Beam Pipe and Diagnostic Section. TESLA-FEL 98-02, March 1988.

[6] M.Dohlus, T.Limberg: Emittance Growth Due to Wake Fields on Curved Bunch Trajectories. FEL Conference, Rome, Aug. 1996, printed in Nuclear Instruments and Methods in Physics Research, A 393, p 494-499, 1997.

Efficient Field Calculation of 3D Bunches on General Trajectories

M.Dohlus, A.Kabel, T.Limberg

Deutsches Elektronen Synchrotron DESY, Notkestr. 85, D-22607 Hamburg

Abstract

The program TRAFIC4 calculates the effects of space charge forces and coherent synchrotron radiation on bunches moving on curved trajectories. It calculates the fields acting on the particles, as they travel along the beamline, from first principles. The bunch is modeled by small overlapping 1d, 2d or 3d continuous gaussian sub-bunches. Previously a 1d or 2d integration of the retarded source distribution was used to calculate the fields of 1d and 2d sub-bunches. A new approximation is proposed to avoid the effort of multi-dimensional integration: a 2d or 3d sub-bunch can be interpreted as the convolution of a 1d sub-bunch with a transverse density function. In the same way the field can be obtained by a convolution of the 1d-field with the transverse density function. The near field of a 1d sub-bunch can be split into a singular part which is dominated by local effects and the residual part, which depends essentially on long range interactions. As the singular part can be described by analytical functions, the convolution can be performed efficiently. The residual part depends weakly on the transverse offset. Therefore only one or few sampling points are needed for the convolution, which significantly reduces the numerical effort.

1. Introduction

Dispersive bunch compressors are used to achieve the required bunch properties for some FEL applications, e.g. ~50μm bunch length, normalized emittance of few 10^{-6} rad for the TESLA-TTF SASE FEL [1]. For this type of compressor a linear, length-correlated energy spread is superimposed by a phase shift of the accelerating RF and transformed into a length reduction by a dispersive magnet arrangement. Due to the curved trajectories and the shape variations during the compression processes transient EM fields are generated [2] which have to be taken into account for an appropriate analysis of the beam dynamic. The program TRAFIC4 [3,4,5] splits the real bunch - with time dependent shape - into a set of sub-bunches with fixed shapes, but with individual energies and paths. The fields of these sub-bunches are calculated by a retarded potential approach and considered together with the external fields in the tracking calculation for an ensemble of test particles. To obtain finite fields, the sub-bunches have to be at least two dimensional and smooth fields are generated only by three dimensional charge distributions. The numerical effort for a two or even three dimensional source integration limits the capability to simulate many arrangements under various operation conditions.

To solve this problem a new approximation is proposed which avoids multi-dimensional integration: for a particular type of two and three dimensional charge distributions, which can be described by a convolution of a 1D distribution with a transverse density function, the field quantities can be obtained by a convolution of the 1D field quantities with the density function. The near field of a 1d bunch can be split into a singular part that is dominated by local effects and the residual part, which depends essentially on long range interactions. As the singular part can be described by analytical functions, the convolution can be performed efficiently. The residual part depends weakly on the transverse offset, so that only one or few sampling points are needed for the convolution.

2. Theory

The 1d field solver of TRAFIC4 calculates the magnetic flux density $\mathbf{B}$ and the normalized Lorentz force $\mathbf{W} = \mathbf{E} + \mathbf{v}_t \times \mathbf{B}$ for a line charge density $\lambda(s,t)$ traveling along the path $\mathbf{r}_s(s)$ by a numerical integration of

$$4\pi\varepsilon_0 c_0 \mathbf{B} = \int_{-\infty}^{\infty} \mathbf{e}_s \times \mathbf{G}\beta_s ds\,, \tag{1a}$$

$$4\pi\varepsilon_0\mathbf{W}(\mathbf{r},t) = \int_{-\infty}^{\infty}(\mathbf{e}_t-\mathbf{e}_s)\times\mathbf{e}_s\times\mathbf{G}\beta_s\beta_t ds \;+\; \int_{-\infty}^{\infty}\mathbf{G}\;(1-\beta_s\beta_t)ds$$
$$-\int_{-\infty}^{\infty}\frac{\lambda(s,t')}{R}\beta_s\beta_t\,\partial_s\mathbf{e}_s\,ds+\int_{-\infty}^{\infty}\frac{\dot\lambda(s,t')}{c_0R}(\beta_t-\beta_s)\;\mathbf{e}_s ds \quad , \qquad (\mathbf{1}\text{b}),$$

$$\mathbf{G} = -\nabla\frac{\lambda(s,t')}{R} = \nabla R\left(\frac{\lambda(s,t')}{R^2}+\frac{\dot\lambda(s,t')}{c_0R}\right) \quad , \qquad (\mathbf{1}\text{c})$$

with $\mathbf{R}=\mathbf{r}-\mathbf{r}_s(s)$, $R=\|\mathbf{R}\|$, $t'=t-R/c_0$, $\mathbf{v}_t=\beta_t c_0\mathbf{e}_t$ and $\mathbf{e}_s=\partial_s\mathbf{r}_s$. The line charge density is derived from the current flow $i(s,t):=c_0\lambda_i(t-t_c(s))$ by $\lambda(s,t):=\lambda_i(t-t_c(s))/\beta_s(s)$ with $\beta_s=(c_0\partial_s t_c)^{-1}$. A class of two and three dimensional source distributions can be obtained by the convolution of the one dimensional density with a transverse density function $\eta(x_1,x_2)$ which is defined for an arbitrary plane $\mathbf{r}_\eta(x_1,x_2)=x_1\mathbf{e}_1+x_2\mathbf{e}_2$ with $\mathbf{e}_1\cdot\mathbf{e}_2=0$ and $\int\eta(x_1,x_2)dx_1dx_2=1$. Therefore the 3d charge density is described by

$$\rho(\mathbf{r}=\mathbf{r}_s(s)+x_1\mathbf{e}_1+x_2\mathbf{e}_2,t)=\lambda(s,t)\frac{\eta(x_1,x_2)}{\left|(\mathbf{e}_1\times\mathbf{e}_2)\cdot\partial_s\mathbf{r}_s\right|} \quad . \qquad (2)$$

Of course this class is not sufficient to model more general shape variations as they happen in a bunch compressor, but it is adequate for an efficient sub-bunch approach. In the present version of TRAFIC4 [3] the Lorentz force and the magnetic flux density are computed by the convolution of the corresponding 1d quantities ($\mathbf{X}=\mathbf{W}$ or $\mathbf{B}$) with the transverse density:

$$\mathbf{X}_\eta(\mathbf{r},t)=\int\mathbf{X}(\mathbf{r}-\mathbf{r}_\eta(x_1,x_2),t)\eta(x_1,x_2)dx_1dx_2 \quad . \qquad (3)$$

This convolution is very time consuming as two (three) dimensional integrations have to be carried out for the calculation of two (three) dimensional source distributions.

2.1 One Dimensional Integration with Pole Extraction

As the integrands and integrals of Eq. **1** are singular for observer positions on the path $\mathbf{r}_s(s)$ a pole extraction technique is used for the numerical integration. Therefore the path point $\mathbf{r}_0=\mathbf{r}_s(s_0)$ with minimal distance to the observer is searched for. In the following we calculate the normalized Lorentz force for the case $\mathbf{v}_t=\mathbf{v}_0:=c_0\beta_s(s_0)\mathbf{e}_s(s_0)$ of an observer velociy identical to the source velocity at the closest path point. A different velocity can be taken into account by adding $(\mathbf{v}_t-\mathbf{v}_0)\times\mathbf{B}$. The normalized Lorentz force and the magnetic flux density are split into a singular and a non-singular part $\mathbf{W}=\mathbf{W}_{\mathrm{SP}}+\mathbf{W}_{\mathrm{NS}}$, $\mathbf{B}=\mathbf{B}_{\mathrm{SP}}+\mathbf{B}_{\mathrm{NS}}$ where the non-singular part (index NS) can be calculated numerically for any observation point. The singular part (index SP) is analytically known:

$$4\pi\varepsilon_0\mathbf{B}_{\mathrm{SP}}=\frac{2\beta_0}{c_0}\left[(\mathbf{e}_0\lambda_0)\times\mathbf{w}_1(\Delta\mathbf{r})+\left(\frac{1}{2}\mathbf{d}_0\times\mathbf{e}_0\lambda_0\right)w_2(\Delta\mathbf{r})-(\mathbf{d}_0\lambda'_0)\times\mathbf{w}_3(\Delta\mathbf{r})\right] \quad , \quad (4\text{a})$$

$$\begin{aligned}4\pi\varepsilon_0\mathbf{W}_{\mathrm{SP}} &= 2\beta_0^2\mathbf{d}_0\times(\mathbf{e}_0\lambda'_0+\mathbf{d}_0\lambda_0)\times\mathbf{w}_3(\Delta\mathbf{r})\\ &+\frac{2}{\gamma_0^2}\left[\lambda_0\mathbf{w}_1(\Delta\mathbf{r})+\left(\mathbf{e}_0\lambda'_0+\frac{1}{2}\mathbf{d}_0\lambda_0\right)w_2(\Delta\mathbf{r})\right], \qquad (4\text{b})\\ &+2\beta_0^2\mathbf{d}_0\lambda_0 w_2(\Delta\mathbf{r})\end{aligned}$$

with

$$\mathbf{w}_1(\Delta\mathbf{r})=\Delta\mathbf{r}/\|\Delta\mathbf{r}\|^2 \quad , \qquad (5\text{a})$$

$$w_2(\Delta\mathbf{r}) = \ln\left(\|\Delta\mathbf{r}\|/R_{\text{ref}}\right) \quad , \tag{5b}$$

$$\mathbf{w}_3(\Delta\mathbf{r}) = \Delta\mathbf{r}\ln\left(\|\Delta\mathbf{r}\|/R_{\text{ref}}\right) \quad , \tag{5c}$$

$\Delta\mathbf{r} = \mathbf{r} - \mathbf{r}_0, \mathbf{e}_0 = \mathbf{e}_s(s_0)$, $\mathbf{d}_0 = \partial_s \mathbf{e}_s(s_0)$, $\beta_0 = \beta_s(s_0)$, $\lambda_0 = \lambda(s_0,t)$, $\lambda_0' = \partial_s \lambda(s_0,t)$ and R_{ref} an arbitrary normalisation length.

2.2 Convolution Method

For the calculation of the fields $\mathbf{W}_\eta(\mathbf{r},t)$ and $\mathbf{B}_\eta(\mathbf{r},t)$ of a bunch with the transverse density function $\eta(x_1,x_2)$ the convolution integral Eq. 3 has to be solved. As the non singular parts of $\mathbf{W}$ and $\mathbf{B}$ are smooth functions of $\mathbf{r}$ and the singular parts are analytically given, the numerical effort for the convolution can be significantly reduced. This is especially true if the 2d plane $\mathbf{r}_\eta(x_1,x_2)$ of the transverse density function is perpendicular to the path at the point $\mathbf{r}_0 = \mathbf{r}_s(s_0)$. For this case, and for transverse bunch dimensions which are of the same order or smaller than the longitudinal dimension, the non singular parts are almost sampled by the convolution: $\mathbf{B}_{\text{NS},\eta} \approx \mathbf{B}_{\text{NS}}$, $\mathbf{W}_{\text{NS},\eta} \approx \mathbf{W}_{\text{NS}}$. For bunches with larger transverse dimensions only few points of $\mathbf{B}_{\text{NS}}$ and $\mathbf{W}_{\text{NS}}$ have to be evaluated and fitted to compute the convolution. The condition that the 2d plane $\mathbf{r}_\eta(x_1,x_2)$ is perpendicular to the path at the closest point $\mathbf{r}_0$ has some further advantages: the observation point lies in the plane $\mathbf{r}_0 - \mathbf{r}_\eta(x_1,x_2)$ and all other observation points in this plane have the same closest path point $\mathbf{r}_0 = \mathbf{r}_s(s_0)$. Therefore the coefficients $s_0, \mathbf{e}_0, \mathbf{d}_0, \beta_0, \lambda_0, \lambda_0'$ in Eq. 4 are constant for all arguments $(\mathbf{r} - \mathbf{r}_\eta(x_1,x_2), t)$ of $\mathbf{B}_{\text{SP}}$ and $\mathbf{W}_{\text{SP}}$ in the convolution integral Eq. 3. The convoluted singular parts $\mathbf{B}_{\text{SP},\eta}, \mathbf{W}_{\text{SP},\eta}$ are obtained from Eq. 4 by replacing the functions $\mathbf{w}_1, w_2, \mathbf{w}_3$ by

$$\mathbf{w}_{1,\eta}(\Delta\mathbf{r}) = \int \mathbf{w}_1(\Delta\mathbf{r} - \mathbf{r}_\eta(x_1,x_2))\eta(x_1,x_2)dx_1dx_2 \, , \tag{6a}$$

$$w_{2,\eta}(\Delta\mathbf{r}) = \int w_2(\Delta\mathbf{r} - \mathbf{r}_\eta(x_1,x_2))\eta(x_1,x_2)dx_1dx_2 \, , \tag{6b}$$

$$\mathbf{w}_{3,\eta}(\Delta\mathbf{r}) = \int \mathbf{w}_3(\Delta\mathbf{r} - \mathbf{r}_\eta(x_1,x_2))\eta(x_1,x_2)dx_1dx_2 \, . \tag{6c}$$

a) 2D Bunches

For 2d bunches the transverse density function $\eta(x_1)$ depends only on one parameter and and the convolution integrals are reduced to a 1d integration over x_1 with $\mathbf{r}_\eta(x_1) = x_1\mathbf{e}_1$. Therefore only few scalar integrals have to be computed to obtain the functions

$$\mathbf{w}_{1,\eta}(\Delta\mathbf{r}) = \frac{\mathbf{a}}{a}I_1 + \mathbf{e}_1 I_2, \; w_{2,\eta}(\Delta\mathbf{r}) = \frac{1}{2a}I_3, \; \mathbf{w}_{3,\eta}(\Delta\mathbf{r}) = \frac{1}{2}\frac{\mathbf{a}}{a}I_3 + \frac{1}{2}\mathbf{e}_1 I_4 \tag{7}$$

with

$$I_1(a,b) = \int_{-\infty}^{\infty} \frac{a}{a^2+x^2}\eta(b-x)dx, \; I_2(a,b) = \int_{-\infty}^{\infty} \frac{x}{a^2+x^2}\eta(b-x)dx,$$

$$I_3(a,b) = \int_{-\infty}^{\infty} a\ln\left(\frac{a^2+x^2}{R_{\text{ref}}^2}\right)\eta(b-x)dx, \; I_4(a,b) = \int_{-\infty}^{\infty} x\ln\left(\frac{a^2+x^2}{R_{\text{ref}}^2}\right)\eta(b-x)dx \tag{8}$$

and $b = \mathbf{e}_1 \cdot \Delta\mathbf{r}$, $\mathbf{a} = \Delta\mathbf{r} - b\mathbf{e}_1$, $a = \|\mathbf{a}\|$. The substitution of these functions into Eq. 4 leads to the contributions $\mathbf{B}_{\text{SP},\eta}, \mathbf{W}_{\text{SP},\eta}$ and together with $\mathbf{B}_{\text{NS},\eta} \approx \mathbf{B}_{\text{NS}}$, $\mathbf{W}_{\text{NS},\eta} \approx \mathbf{W}_{\text{NS}}$ a numerically efficient approximation is obatined.

b) Round 3d Gaussian bunches

The 2d convolutions Eq. 6 for three dimensional beams with a round Gaussian transverse density function $\eta(x_1, x_2) = g\left(\sqrt{x_1^2 + x_2^2}\,/\sigma_r\right)\Big/\left(\sqrt{2\pi}\sigma_r^2\right)$ can be reduced to the computation of three scalar functions of one parameter:

$$\mathbf{w}_{1,\eta}\left(\Delta\mathbf{r} = r_\Delta \mathbf{e}_\Delta\right) = \frac{\mathbf{e}_\Delta}{r_\Delta} H_1(r_\Delta/\sigma_r)\,, \tag{9a}$$

$$w_{2,\eta}\left(\Delta\mathbf{r} = r_\Delta \mathbf{e}_\Delta\right) = H_2(r_\Delta/\sigma_r) + \ln\left(\frac{r_\Delta}{R_{\mathrm{ref}}}\right), \tag{9b}$$

$$\mathbf{w}_{3,\eta}\left(\Delta\mathbf{r} = r_\Delta \mathbf{e}_\Delta\right) = \Delta\mathbf{r}\left\{H_3(r_\Delta/\sigma_r) + \ln\left(\frac{r_\Delta}{R_{\mathrm{ref}}}\right)\right\} \tag{9c}$$

with

$$H_1(x) = \sqrt{2\pi}\, x \int_0^\infty \mathrm{I}_1(\rho x)\exp(-\rho x) g\left(x-\rho\right) d\rho\,, \tag{10a}$$

$$H_2(x) = \sqrt{2\pi} \int_0^\infty \rho \ln\left(\frac{\rho}{x}\right) \mathrm{I}_0(\rho x)\exp(-\rho x)\, g\left(x-\rho\right) d\rho\,, \tag{10b}$$

$$H_3(x) = \frac{\sqrt{2\pi}}{x} \int_0^\infty \rho^2 \ln\left(\frac{\rho}{x}\right) \mathrm{I}_1(x)\exp(-\rho x) g\left(x-\rho\right) d\rho\,, \tag{10c}$$

and $g(x) = \exp\left(-x^2/2\right)\Big/\sqrt{2\pi}$. The functions $H_1(x)$, $H_2(x)$, $H_3(x)$ have been calculated numerically and are approximated by Chebychev polinomials.

3. Calculations

To verify the presented singularity convolution method $\mathbf{W}_\eta \approx \mathbf{W}_{\mathrm{NS}} + \mathbf{W}_{\mathrm{NS},\eta}$ we compare this method with a direct multi-dimensional integration for a bunch in circular motion. Fig. 1 shows the longitudinal and radial component of the normalized Lorentz force for 2d and 3d bunches with q = 1nC, γ= 100 and the radius of curvature R_c = 10 m. The 2d bunch is a round Gaussian disc in the longitudinal-radial plane with σ= 50 µm, the 3d bunch is a spherical Gaussian distribution with the same σ. The ordinate in Fig. 1 is the longitudinal bunch coordinate (from head to tail for increasing s). All curves are in good agreement, while the numerical effort for the singularity convolution method is about two orders smaller than for the multidimensional integration.

Acknowledgement

We wish to thank E.L. Saldin, E.A. Schneidmiller and J. Rossbach for many useful discussions.

References

[1] R.Brinkmann: Conceptual Design of a 500 GeV e+e- Linear Collider with Integrated X-ray Laser Facility. DESY 1997-048, ECFA 1997-192.

[2] E.Saldin, E.Schneidmiller, M.Yurkov: On the Coherent Radiation of an Electron Bunch Moving in an Arc of a Circle. TESLA-FEL 96-14.

[3] M.Dohlus, A.Kabel, T.Limberg: Wake Fields of a Bunch on a General Trajectory due to Coherent Synchrotron Radiation. PAC97

[4] M.Dohlus, A.Kabel, T.Limberg: Uncorrelated Emittance Growth in the TTF-FEL Bunch Compression Sections Due to Coherent Synchrotron Radiation and Space Charge Effects. EPAC98.

[5] K.Rothemund, M.Dohlus, U.v.Rienen: Calculation of Coherent Fields of Charged Particle Bunches on General Trajectories. FEL99 (same Conference)

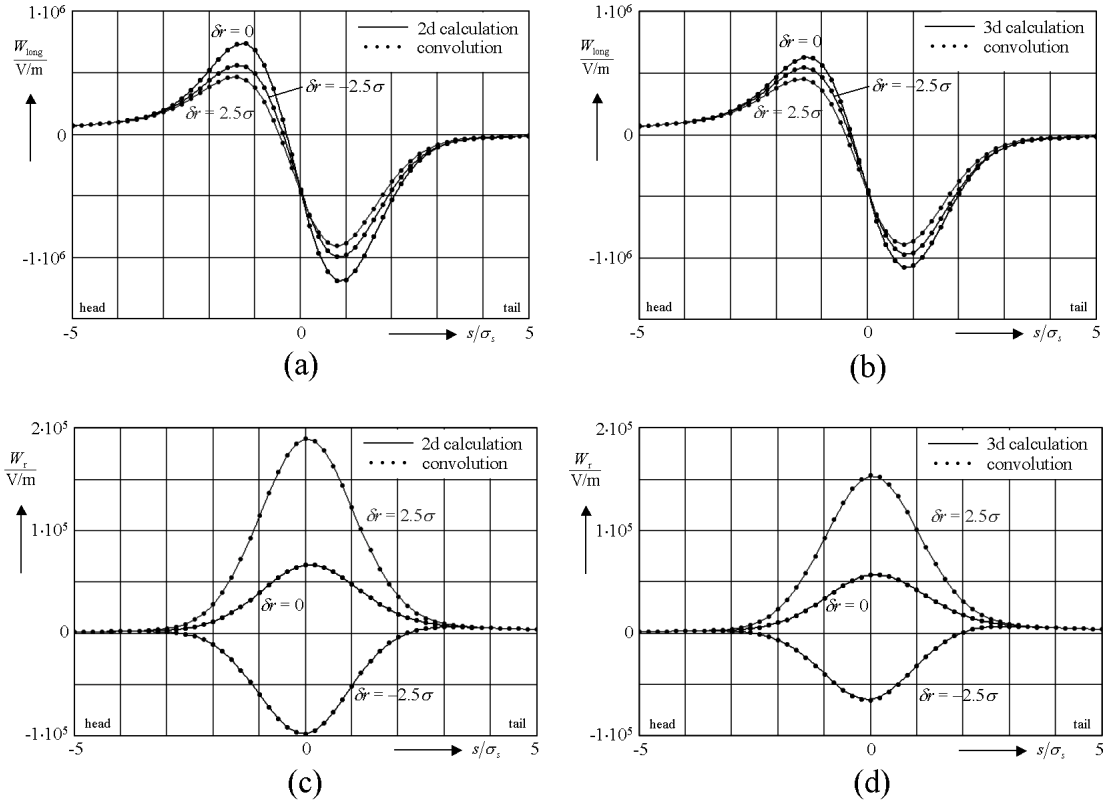

Fig. 1: Longitudinal and radial component of $\mathbf{W} = \mathbf{E} + \mathbf{v}_t \times \mathbf{B}$ for a bunch in circular motion (parameters: curvature radius 10 m, bunch charge 1 nC, bunch length σ = 50 µm, γ = 100). All figures compare the results of a direct multidimensional integration (solid lines) and the singularity convolution method (dotted lines). The fields of a 2d disc shaped bunch are shown in (a) and (c) and of a 3d spherical bunch in (b) and (d). The disc shaped bunch lies in the plane of curvature.

MULTI-DIMENSIONAL FREE-ELECTRON LASER SIMULATION CODES: A COMPARISON STUDY*

S.G Biedron[1], Y.C. Chae, R.J. Dejus, B. Faatz[2], H.P. Freund,[3]
S.V. Milton, H-D. Nuhn[4], S. Reiche[2]

Advanced Photon Source, Argonne National Laboratory, Argonne, Illinois 60439 USA

Abstract: A self-amplified spontaneous emission (SASE) free-electron laser (FEL) is under construction at the Advanced Photon Source (APS). Five FEL simulation codes were used in the design phase: GENESIS, GINGER, MEDUSA, RON, and TDA3D. Initial comparisons between each of these independent formulations show good agreement for the parameters of the APS SASE FEL.

1. INTRODUCTION

The Advanced Photon Source (APS) at Argonne National Laboratory (ANL) is currently commissioning a free-electron laser (FEL) based on the self-amplified spontaneous emission (SASE) process [1]. The design parameters were based on capabilities of the existing APS linear accelerator, as well as on the results of various linear and nonlinear theoretical analyses. In this paper, we present a comparison of the results from linear theory [2], and five simulation codes. The codes used in the design include GENESIS [3], GINGER [4], MEDUSA [5], RON [6], and TDA3D [7,8]. Comparative simulations were performed for the parameters of the APS SASE FEL.

2. CODE DESCRIPTIONS

Before proceeding with the specific comparisons, a brief specification of the characteristics and capabilities of each of the simulation codes is necessary. Table 1 contains a brief listing of the more important properties of each of these codes. Of the five codes under consideration, only RON is limited to the linear regime; the other four are fully nonlinear. Three of the codes (GENESIS, GINGER, and MEDUSA) are fully polychromatic and can treat the full SASE spectrum. MEDUSA is also capable of treating an arbitrarily large spectrum of harmonics. All of the codes except MEDUSA use a wiggler-average to treat particle dynamics; MEDUSA integrates the trajectories using the complete Lorentz force equations. The radiation field is obtained from a 3D (2D) field solver (FS) in TDA3D and GENESIS (GINGER) and from a 3D source-dependent expansion (SDE) in MEDUSA. Finally, all of the codes except GINGER are able to treat wiggler errors. Detailed descriptions of the codes are listed in the References section.

---

*Work supported by U.S. Department of Energy, Office of Basic Energy Sciences, under Contract Nos. W-31-109-ENG-38 and DE-AC03-76SF00515.

[1] Email: biedron@aps.anl.gov

[2] Deutsches Elektronen Synchrotron, Notkestrasse 85, 22603 Hamburg, Germany.

[3]Permanent Address: Science Applications International Corporation, McLean, VA 22101, USA.

[4]Stanford Linear Accelerator Center, Stanford, California 94309, USA.

Table 1: Code Properties

Code	Nonlinear	Poly-chromatic	Averaged Orbits	Radiation Field	Wiggler Errors
GENESIS	Yes	Yes	Yes	3D FS	Yes
GINGER	Yes	Yes	Yes	2D FS	No
MEDUSA	Yes	Yes	No	3D SDE	Yes
RON	No	No	Yes	3D FS	Yes
TDA3D	Yes	No	Yes	3D FS	Yes

3. CODE COMPARISONS

The APS SASE FEL uses either a thermionic rf or photocathode rf gun, the 650-MeV, 2856-MHz APS linac, two new transfer lines, and a new undulator hall with an optical diagnostics end station. The project will evolve over three phases, to reach saturation in the visible, UV, and VUV wavelength regimes, respectively. The design is based on known gun performance, constraints imposed by the APS linac, and the characteristics of currently available undulators. Tuning of the undulators has been optimized to meet the performance tolerances of the FEL. A set of parameters for the first phase was used for this comparison, and a Gaussian electron beam distribution was assumed. The specific parameters are summarized in Table 2.

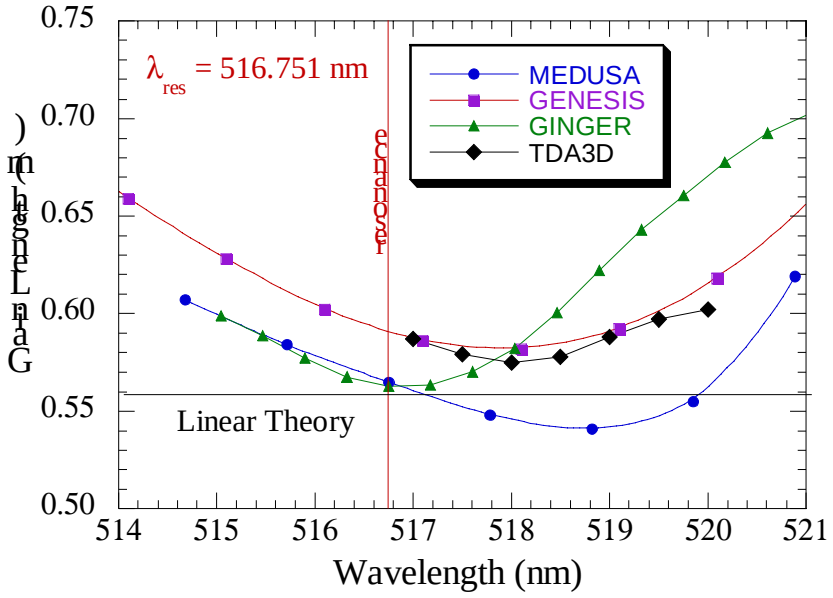

Fig. 1 Gain length versus wavelength for the nonlinear codes.

The optimum wavelength, corresponding to the minimum gain length, was obtained for each code by scanning in wavelength near the resonance. Note that the familiar 1D resonance formula [$\lambda = \lambda_w(1 + K^2/2)/2\gamma^2$] yields a wavelength of 516.75 nm. The results are shown in Fig. 1, where the gain length versus wavelength from MEDUSA, GENESIS, TDA3D, and GINGER are plotted. Such a scan is not available using RON. The optimal wavelengths for all five codes, however, are given in Table 3. Note that growth is not purely exponential in any of the nonlinear codes, and the gain length is dependent on the axial region chosen for the exponential fit. As a result, there is some uncertainty in the gain length and in the optimum wavelength, which impacts the saturated power. Nevertheless, the optimum wavelengths in GENESIS and TDA3D agree to within the accuracy of the procedure. The optimum wavelengths in RON and MEDUSA are also in close agreement and are slightly higher than in GENESIS and TDA3D (by ~ 0.2%). Note that in

each of these codes, the optimum wavelength is slightly longer than the resonant wavelength. GINGER differs in that the optimum wavelength is very close to the 1D resonance.

Table 2: Simulation and Undulator Cell Parameters

Parameter	Value
γ	430.529
Normalized emittance	5π mm-mrad
Peak current	150 A
Undulator period	3.3 cm
Undulator strength (K)	3.1
Energy spread	0.1%
Input start-up power	1.0 W
Undulator length	2.4 m
Focusing/diagnostics gap	36 cm
Quadrupole strength	20 m^{-2}
Quadrupole length	5 cm

Table 3: Optimum Wavelengths

Code	Optimum λ (nm)
GENESIS	517.78
GINGER	516.80
MEDUSA	518.82
RON	518.80
TDA3D	517.78

We consider a single-segment undulator with parabolic pole faces. The actual design uses multiple 2.763-m undulator "cells," each of which is composed of a 2.4-m magnetic segment and a 0.363-m section

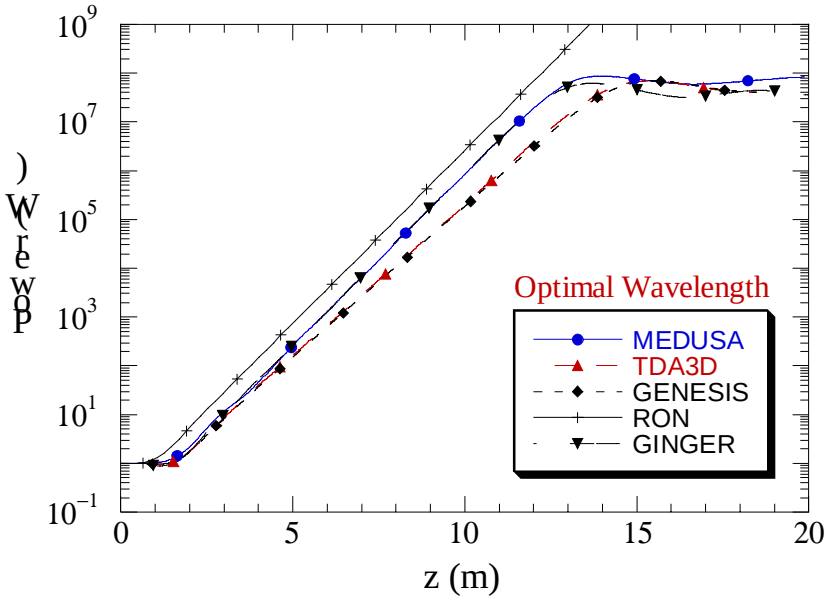

Fig. 2 Single segment case.

for diagnostics, a combined quadrupole/corrector magnet, and drift space (see Table 2). The power versus distance along the undulator at the optimal wavelengths is shown in Fig. 2. The curves for GINGER and MEDUSA are almost identical and differ primarily in that GINGER predicts a somewhat lower saturated power. The calculated radiated power for RON is scaled from the bunched beam current density that is valid for the behavior in the exponential growth regime only where the radiated power is self-similar to the beam current. Thus, only the gain length in RON should be compared with the other codes. The gain length is almost identical in GINGER, MEDUSA, and RON. TDA3D and GENESIS yield nearly identical results, but the gain lengths are slightly longer than found with the other codes.

It should be noted that determining the gain length is not an unambiguous process in the nonlinear codes since these codes do not predict pure exponential growth (i.e., the derivative of the power versus distance is not precisely a constant along the length of the undulator). As a result, it is necessary to obtain a "best fit" to exponential growth that requires consideration of what length to choose; this introduces some

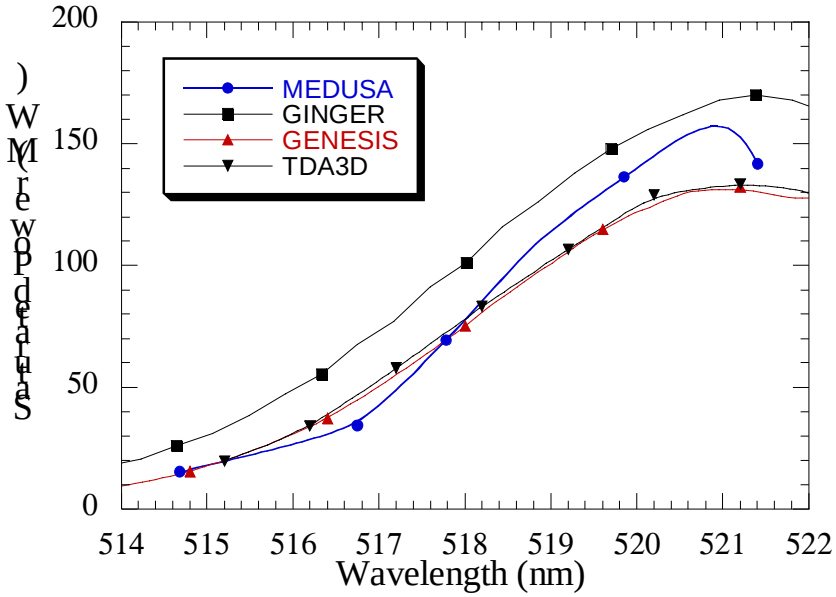

Fig. 3 Saturated power versus wavelength for the nonlinear codes.

uncertainty into the process. Differences of the order of 10-15% in the gain length from the different codes are within the range of uncertainty.

Some care should be used in interpreting the differences in the saturated power found between the codes at the optimum wavelength. The saturated power is a sensitive function of wavelength within the gain band, and small differences in the choices for the wavelength can result in relatively large variations in saturated power. This is illustrated in Fig. 3 where we plot the saturated power versus wavelength for the nonlinear codes. As shown in the figure, the nonlinear codes are in reasonable agreement, and the power increases from 10-20 MW at short wavelengths to between 120-170 MW at long wavelengths. Of the four codes, GINGER predicts the highest power at any given wavelength, while GENESIS and TDA3D predict the lowest. MEDUSA typically yields powers intermediate to those generated by the other three codes.

We now simulate the actual undulator design (less corrector fields) with flat pole face undulators and quadrupoles (Table 2) at the optimal wavelength found in the single-segment case. The power versus distance for the multi-segment case is shown in Fig. 4. Here, the shortest gain lengths are predicted by RON and GINGER, the longest by MEDUSA, while GENESIS and TDA3D predict intermediate gain lengths. In addition, the saturation powers in TDA3D and GENESIS are very close in this case, as are those predicted by GINGER and MEDUSA.

Table 4 summarizes the saturation point and power for the single- and multiple-segment cases as determined by the nonlinear codes at the optimal wavelengths listed in Table 3. Note that the saturated powers found in TDA3D and GENESIS, although not identical, are very close, while MEDUSA predicts somewhat higher and GINGER somewhat lower powers. It is not clear at this time why the saturated power predicted by GINGER and MEDUSA for the multi-segment case is so much higher than that found in TDA3D and GENESIS or why it is higher than the power found in the single-segment case. However, the saturated power is very sensitive to wavelength, and we speculate that there is some small retuning of the interaction for the multi-segment case due to differences in the beam dynamics.

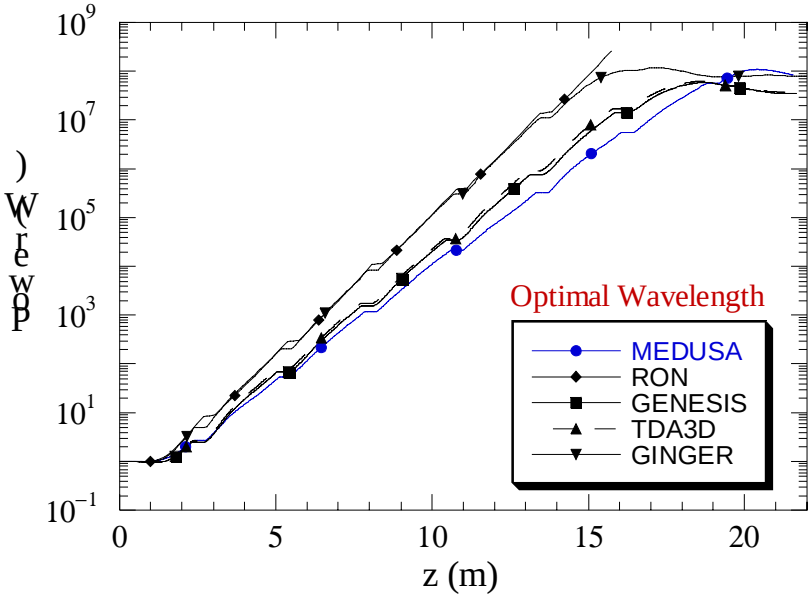

Fig. 4 Multiple segment case.

Table 4: Saturation Points and Power

Code	Single-Segment		Multi-Segment	
	L_{SAT}	P_{SAT}	L_{SAT}	P_{SAT}
GENESIS	15.5	69.4 MW	18.8	58.0 MW
GINGER	13.7	61.7 MW	17.2	118 MW
MEDUSA	14.0	87.4 MW	20.8	109 MW
TDA3D	15.4	68.9 MW	18.7	61.2 MW

Wiggler imperfections have been simulated using TDA3D, MEDUSA, and GENESIS for the single-segment undulator. GINGER was omitted from this comparison because it cannot as yet treat wiggler imperfections, and RON was omitted because it was decided to study the effect of wiggler imperfections on the saturated power, and RON treats only the linear regime. In Figure 5, the efficiency found using the TDA3D, MEDUSA, and GENESIS is plotted versus the rms magnitude of the wiggler imperfections. A series of runs was made at a given $(\Delta B_w/B_w)_{rms}$, each with a different error distribution. The number of runs used was determined by the requirement that the average efficiency converges to within 1% accuracy. The dots in the figure denote the ensemble average and the error bars denote the standard deviations about the average values. Of the three codes, GENESIS predicted the slowest decline in efficiency with increasing $(\Delta B_w/B_w)_{rms}$, and TDA3D predicted the fastest. One reason why the decline is so rapid in TDA3D may be because it was run using the lowest order modes, which may not treat the required beam displacements with sufficient accuracy. However, the results from actual undulators constructed without careful sorting procedures can be expected to lie anywhere within the range indicated by the error

bars. It is important to note that the ensemble averages found using the codes fall largely within the error bars; hence, substantial agreement is found in the description of wiggler imperfections.

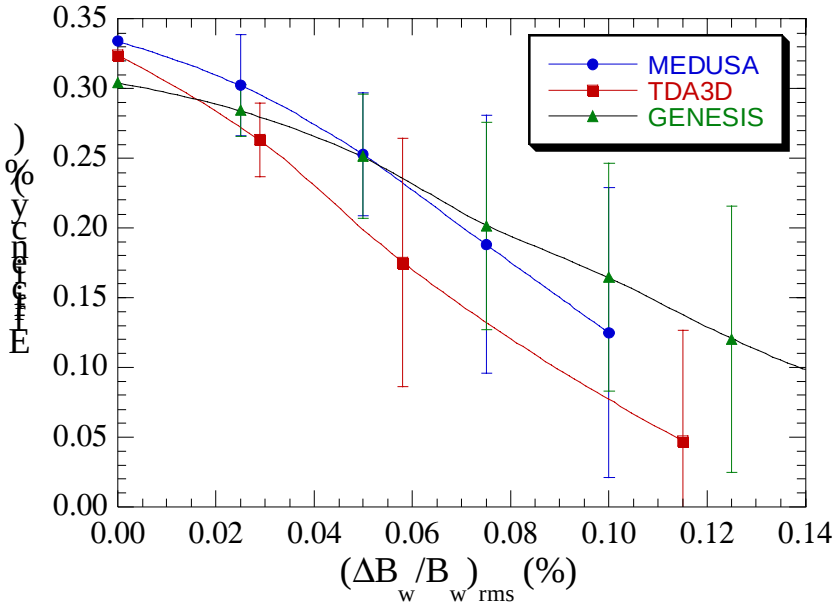

Fig. 5 Efficiency versus rms wiggler error.

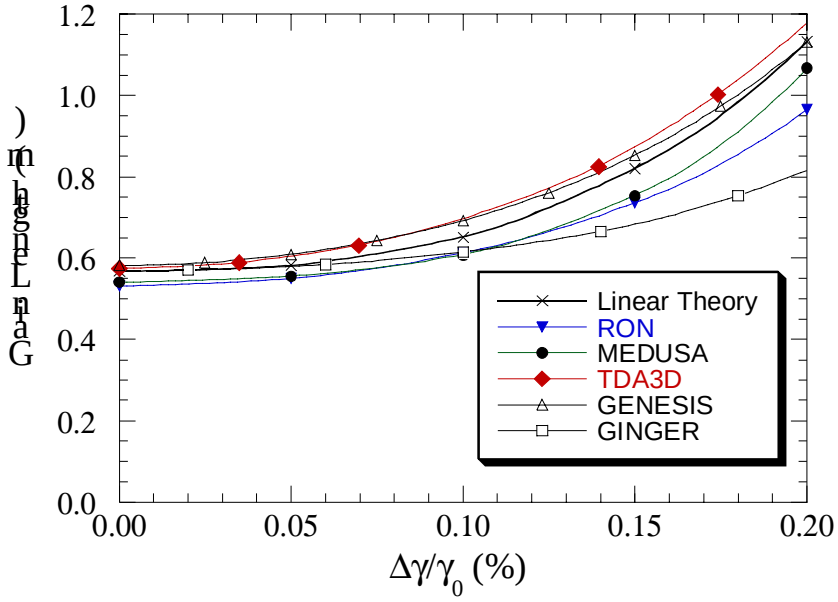

Fig. 6 Gain length versus energy spread.

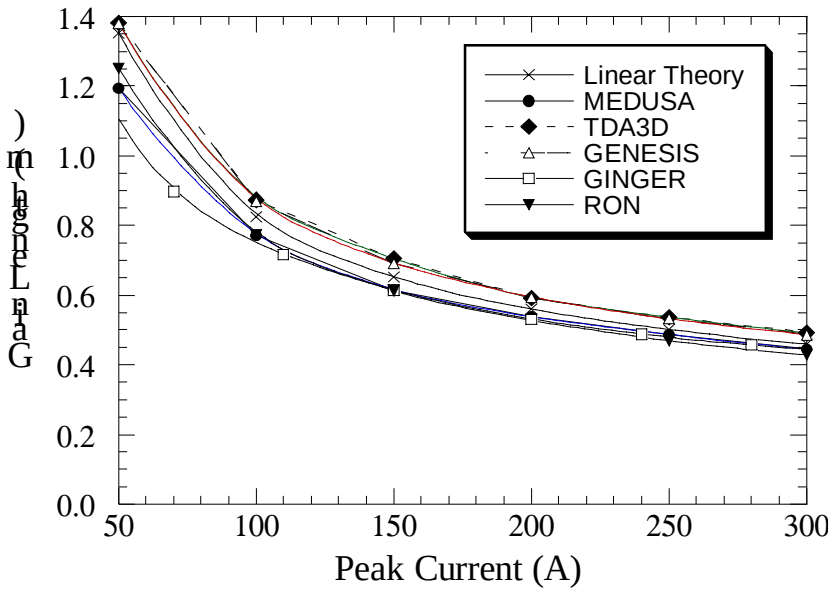

Fig. 7 Gain length versus peak current.

Comparisons of the gain length predicted by the codes and the linear theory for the single-segment case were also made. The energy spread was varied between 0.0-0.2%, the peak current between 50-300 A, and the normalized emittance between 1-10 π mm-mrad. Figures 6, 7, and 8 show these variations. The codes are in reasonable agreement over the entire range of parameters studied. In general, it appears that GENESIS and TDA3D predict slightly longer gain lengths than the linear theory, while GINGER, MEDUSA, and RON predict slightly shorter gain lengths. Note that the linear theory is used for comparison purposes only, and should not be assumed as "perfect" but considered as an additional model. While the maximum discrepancies are of the order of 20% at some of the extremes of these parameter ranges, the maximum discrepancies are typically less than 15% for the parameters of interest in the APS SASE FEL.

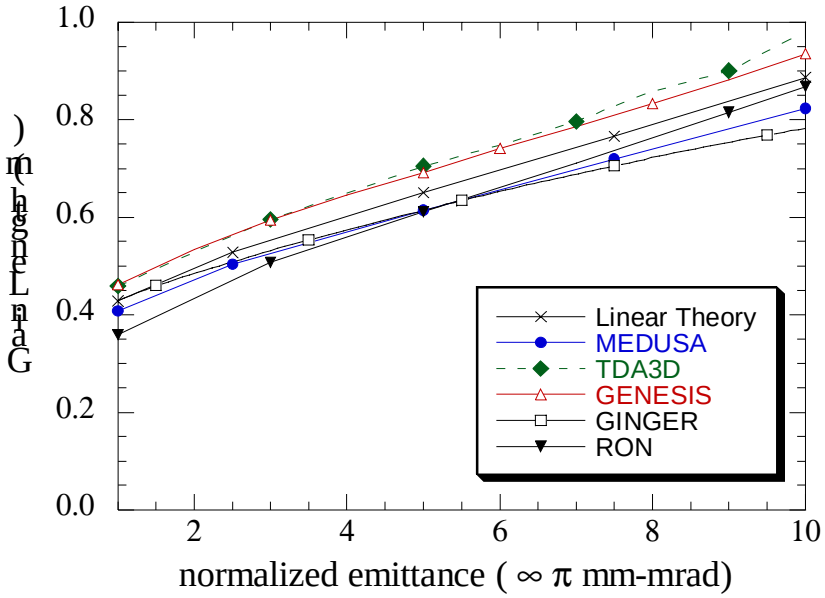

Fig. 8 Gain length versus normalized emittance.

4. Conclusions

In summary, GENESIS, GINGER, MEDUSA, RON, and TDA3D all show reasonable agreement with each other and with the linear theory for the first-phase APS SASE FEL parameters, giving greater confidence to the required length of undulator needed to reach full saturation.

REFERENCES

1. S.V. Milton et al., "FEL Development at the APS: The APS SASE FEL," in *Free-Electron Laser Challenges II*, Harold E. Bennett, David H. Dowell, Editors, Proceedings of SPIE, Vol. 3614, 86-95 (1999).
2. L.-H. Yu et al., Phys. Rev. Lett. **64**, 3011 (1990); M. Xie, in Proceedings of the IEEE1995 Particle Accelerator Conference, 183 (1995).
3. S. Reiche, in NIM Proceedings of the 20th International FEL Conference (FEL98), Williamsburg, VA, USA, to be published.
4. W.M. Fawley, "An Informal Manual for GINGER and its post-processor XPLOTGIN," LBID-2141, CBP Tech Note-104, UC-414 (1995).
5. H.P. Freund and T.M. Antonsen, Jr., *Principles of Free-electron Lasers* (Chapman & Hall, London, 1986), 2nd edition; H.P. Freund, Phys. Rev. E, **52**, 5401 (1995).
6. R.J. Dejus et al., in NIM Proceedings of the 20th International FEL Conference (FEL98), Williamsburg, VA, USA, to be published.
7. T.M. Tran and J.S. Wurtele, Computer Physics Communications **54**, 263-272 (1989); S. Reiche and B. Faatz, in NIM Proceedings of the 20th International FEL Conference (FEL98), Williamsburg, VA, USA, to be published.
8. H.-D.Nuhn, "Overview of SASE Free-Electron Laser Simulation Codes," in *Free-Electron Laser Challenges II*, Harold E. Bennett, David H. Dowell, Editors Proceedings of SPIE, Vol. 3614, 119-130 (1999).

Sub-Picosecond Bunch Length Measurement at the TESLA Test Facility

M. Geitz [a,1] G. Schmidt [a] P. Schmüser [a,2] G. v. Walter [b]

[a] *Deutsches Elektronen-Synchrotron, D–22603 Hamburg, Germany*

[b] *3. physikalisches Institut der RWTH Aachen, D–52072 Aachen, Germany*

Abstract

Sub-picosecond electron bunches are required for the operation of future VUV and X-ray Free Electron Lasers. A streak camera, a Martin-Puplett interferometer and a longitudinal phase space rotation method have been applied at the TESLA Test Facility linac to measure electron bunch lengths.

1. Introduction

Future electron-drive linacs for VUV and X-ray Free Electron Lasers (FEL) require electron bunches of at least 1 nC charge, low emittance (typically 1 mm mrad) and bunch length well in the sub-picosecond regime [1]. These high quality electron bunches are commonly produced by an rf gun based photo injector followed by a magnetic bunch compression chicane. The TTF photo injector is driven by an intense ultraviolet laser beam (typically 20 mJ pulse energy) to produce $6.25 \cdot 10^9$ electrons per bunch from a Cs_2Te photo cathode. The electron bunches are accelerated rapidly by the strong electric fields ($35 - 50\,\mathrm{MV/m}$) of the gun cavity to avoid an emittance blow-up due to space charge forces. The bunch length obtained from an rf gun depends on both the laser pulse length (typically $\sigma_t = 8\,\mathrm{ps}$) and the compression caused by the rf field within the first few centimeters of the gun cavity. By a proper choice of the rf phase a velocity modulation can be impressed on the electron bunch leading to a reduction of its length within the gun cavity. Further bunch compression is achieved by combining off-crest rf acceleration with a magnetic chicane. The off-crest acceleration produces a correlated energy distribution along the bunch with the higher energy electrons trailing the lower energy ones. The higher energy particles travel on a shorter path through the magnetic chicane and a compression is obtained. The bunches pass a second accelerating section and are then guided to a magnetic spectrometer for momentum analysis.

2. Streak Camera Measurement:

The electron bunches produced by the TTF photo injector ($Q = 3\,\mathrm{nC}$, UV laser pulse length $\sigma_t = 15\,\mathrm{ps}$) have been transfered, without the use

[1] corresponding author: DESY, D–22603 Hamburg, Tel.: +49 40 8998 4131, e-mail: geitz@sun52a.desy.de

[2] permanent address: University of Hamburg, D–20146 Hamburg, Germany

of the magnetic chicane compressor, to the spectrometer magnet. During the acceleration from 16 to 170 MeV, the longitudinal charge distribution can be considered as invariant. Synchrotron light pulses, produced in the spectrometer dipole, are detected with a streak camera of 2 ps resolution. Figure 1 (left) shows the charge distribution corresponding to the minimum bunch length measured ($\sigma_z = 1.95 \pm 0.1$ mm). The right graph shows the variation of the bunch length with the rf gun phase. Superimposed is the prediction by PARMELA.

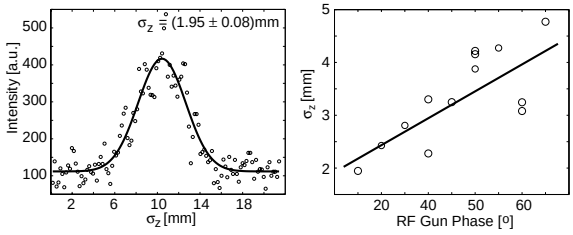

Fig. 1. Streak camera measurements of the longitudinal bunch charge distribution. Left: minimum bunch length. Right: Bunch length versus rf gun phase.

3. Fourier Transform Spectroscopy

Coherent Transition Radiation can be used to determine the longitudinal bunch charge distribution [2,3]. The radiator is a thin aluminum foil arranged at an angle of 45° with respect to the beam direction so that the backward lobe of the radiation is emitted at 90° and is easily extractable from the vacuum chamber through a quartz window. The spectral intensity emitted by a bunch of N particles is

$$I_{\mathrm{tot}}(\omega) = I_1(\omega)\left(N + N(N-1)\left|f(\omega)\right|^2\right) \quad (1)$$

where $I_1(\omega)$ is the intensity radiated by a single electron at a given frequency ω and $f(\omega)$ is the longitudinal bunch form factor defined as the Fourier transformation of the normalized longitudinal charge distribution ρ_z. $T(\omega)$ denotes the spectral acceptance function of the detection device.

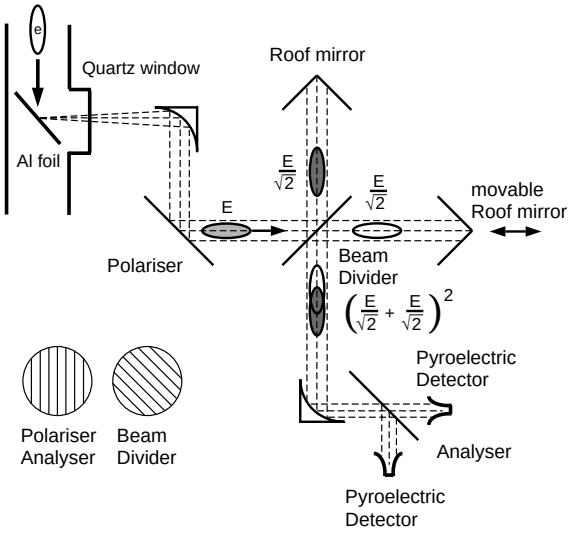

Fig. 2. The Martin-Puplett Interferometer

A Martin-Puplett interferometer, shown schematically in Figure 2, is used to determine the autocorrelation function of the radiation pulse [4]. The diverging transition radiation pulse is transformed into a parallel beam entering the interferometer by a parabolic mirror. The incident radiation pulse is horizontally polarized by the first grid and then splitted by the beam divider into components of orthogonal polarization entering the two interferometer arms. The polarization is flipped by the roof mirrors, hence the component which is first transmitted by the beam splitter is now reflected and vice versa. The recombined radiation is in general elliptically polarized, depending on the path difference in both interferometer arms. The analyzing grid transmits one polarization component into detector 1 and reflects the orthogonal component into detector 2. Two pyroelectric detectors equipped with horn antennas are used as detection devices for the sub-millimeter wavelength radiation.

A Fourier transformation of the autocorrelation function yields the absolute magnitude of the longitudinal bunch form factor. The experimentally determined spectral intensity is strongly modified by the frequency dependent transfer function $T(\omega)$ of the interferometer. As shown in Fig. 3, $T(\omega)$ has its maximum, T_{max}, at around 400 GHz and

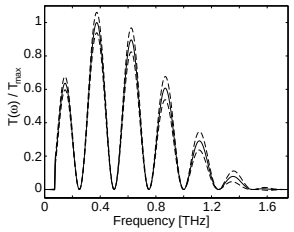

Fig. 3. Spectral transfer function $T(\omega)$ of the Martin-Puplett interferometer. The dashed curves indicate the estimated uncertainty of the transfer function.

decreases towards lower frequencies due to the finite size of the transition radiator and diffraction losses in the interferometer, while the reduction towards larger frequencies is caused by transmission and reflection losses of the quartz window and the wire grids. The oscillatory behaviour is due to interference effects in the 100 μm thick $LiTaO_3$ crystals of the pyroelectric detectors [6]. The transmission of the quartz window and the wire grids has been measured by means of time-domain THz-spectroscopy [7].

Figure 4 shows the autocorrelation (left) as measured by the Martin-Puplett interferometer and the evaluated coherent power spectrum. The measurement was performed at a beam energy of 170 MeV with a bunch charge of 1 nC and laser pulse length of $\sigma_t = 8$ ps. The rf gun phase was adjusted to produce the minimum electron bunch length. The data cannot be described by a single Gaussian charge distribution. Instead, the superposition of three Gaussian curves of different variance and amplitude is required for a good adaption of the model to the measured data. The FWHM bunch length is (1.13 ± 0.45) ps, where the error

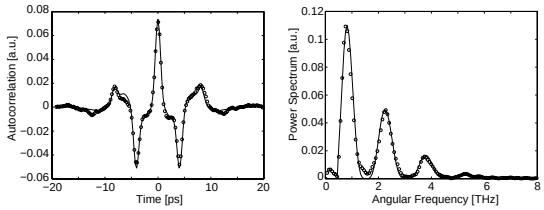

Fig. 4. Autocorrelation (left) and coherent power spectrum (right) measured for optimum bunch compression. Data are indicated by circles. The solid curves are the autocorrelation and power spectrum of a simulated longitudinal charge distribution convoluted with the spectral transfer function.

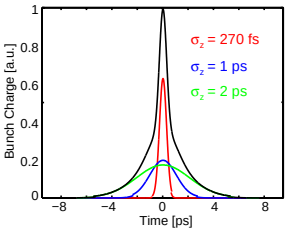

Fig. 5. Longitudinal bunch charge distribution derived from the autocorrelation and coherent power spectrum of Fig. 4. The charge distribution consists of three Gaussians $A_1 = 0.9, \sigma_1 = 0.27$ ps, $A_2 = 0.28, \sigma_2 = 1.0$ ps and $A_3 = 0.25, \sigma_3 = 2.0$ ps. The A_i denote the amplitudes and the σ_i the variances.

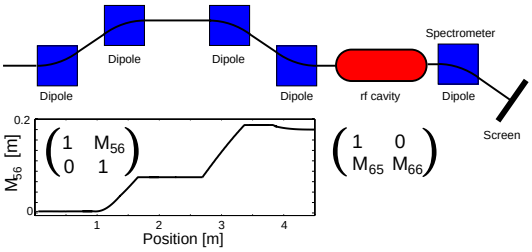

Fig. 6. A magnetic bunch compressor chicane followed by an off-crest acceleration can be used to determine the longitudinal bunch charge distribution.

is mainly caused by the uncertainty of $T(\omega)$. The shape of the longitudinal charge distribution, a short pulse superimposed onto a wider basis, can be explained by a partially uncorrelated bunch energy distribution.

4. Energy Spread Measurement

An efficient and straight forward way to determine the bunch length is the evaluation of the bunch energy distribution. Fig. 6 shows the magnetic bunch compressor chicane followed by an rf cavity and a spectrometer dipole to determine the energy profile. The longitudinal dynamics is described by the transport matrix

$$\left(\begin{array}{c} L \\ \frac{\Delta E}{E} \end{array}\right)\Bigg|_{\mathrm{f}} = \begin{pmatrix} 1 & M_{56} \\ M_{65} & M_{56}M_{65} + M_{66} \end{pmatrix} \left(\begin{array}{c} L \\ \frac{\Delta E}{E} \end{array}\right)\Bigg|_{\mathrm{i}} \qquad (2)$$

where M_{56}, M_{65} and M_{66} denote transfer matrix elements of the chicane and the rf cavity of Figure 6. If we choose the matrix elements such that $M_{56}M_{65} + M_{66} \to 0$, the energy profile

measured with the spectrometer is a direct image of the longitudinal bunch charge distribution in front of the compression section [8]. Figure 7 shows an energy profile measurement performed at optimum compression with 1 nC bunch charge at a beam energy of 170 MeV and laser pulse length of 8 ps. The profile yields a FWHM energy

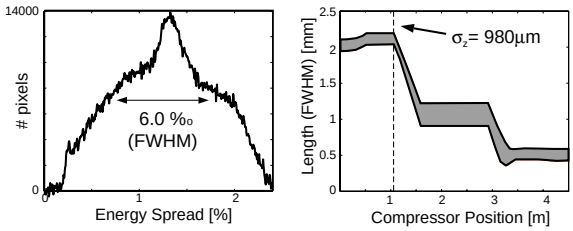

Fig. 7. Left: energy profile measurement at optimum bunch compression. Right: the evaluated compression of the electron bunch within the chicane compressor. The initial bunch length is a free parameter of the computation.

spread of (1.00 ± 0.07) MeV. Using Equation (2), the energy profile can be transformed into a longitudinal charge profile yielding a FWHM bunch length of (2.3 ± 0.3) mm in front of the chicane. The right graph shows the reduction of the electron bunch length when moving along the chicane. The FWHM length of the compressed bunch is (600 ± 110) μm. The shaded area denotes the error of the measurement.

5. Conclusion

The uncompressed longitudinal charge distribution has been measured with a streak camera and by observing the beam energy spread. The streak camera measures a minimum injector bunch length of $\sigma_z = (1.95 \pm 0.1)$ mm. The energy spread analysis yields $\sigma_z = (990 \pm 90)$ μm. The factor of 2 is explainable by the reduced UV laser pulse length during the energy spread measurement. The compressed bunch length measured by the interferometer ($\sigma_z = (200 \pm 70)$ μm) and by the energy spread analysis ($\sigma_z = (260 \pm 50)$ μm) coincide within their error bars.

Acknowledgements

We want to thank Dr. Ingrid Wilke and Mr. Maxim Khazan for carrying out the spectral transmission measurements using time-domain THz spectroscopy at the University of Hamburg.

References

[1] TESLA-Collaboration, DESY-TESLA 95-01 (1995).

[2] J. S. Nodvick et al. , Phys. Rev. A, Vol. 96, No. 2, (1954) and references therein.

[3] E. B. Blum et al. , Nucl. Instr. Meth. A 307, (1991) and references therein.

[4] B. Leissner et al. , Proc. of the PAC conference, New York, 1999 and references therein.

[5] M. Castellano et. al, LNF-98/017(P), 1998.

[6] C. Settakorn et. al, SLAC-PUB-7813, 1998.

[7] I. Wilke et. al, Proc. of EUCAS99, to be published.

[8] K. Ricci et al. , Proc. of the FEL conference, Williamsburg, 1998.

Determination of the Longitudinal Phase Space Distribution produced with the TTF Photo Injector

M. Geitz [a], S. Schreiber [a], G. von Walter [b], D. Sertore [a,1], M. Bernard [c], B. Leblond [c]

[a] *Deutsches Elektronen-Synchrotron, D–22603 Hamburg, Germany*

[b] *RWTH Aachen, D–52056 Aachen, Germany*

[c] *Laboratoire de l'Accélérateur Lineaire, F–91405 Orsay, France*

Abstract

The longitudinal phase space distribution of the beam produced with the rf photo injector of the TESLA Test Facility at DESY is mainly determined by the longitudinal laser pulse shape and the compression due to the rf acceleration field in the rf gun. The longitudinal electron distribution is measured with a high resolution streak camera using synchrotron radiation at the spectrometer dipole (E = 200 MeV). The same streak camera is used to measure the UV laser pulse shape. The longitudinal distribution of the laser and the electron beam can alternatively be determined by Fourier transform spectroscopy. The energy spread of the beam is determined by measuring the beam profile in the dispersive section using optical transition radiation. Dephasing of the superconducting accelerating cavities and variation of bunch compression parameters allow further measurements of the longitudinal phase space distribution.

1. Introduction

Since late 1998, the new photo injector [1] based on a laser driven rf gun and a superconducting accelerating cavity is in operation at the TESLA Test Facility at DESY [2]. The injector is used to perform experiments with high bunch charges related to beam dynamics in accelerating structures, and to serve as an injector for high peak current, low emittance bunches to drive the free electron laser. The beam is injected into the first accelerating module, a string of eight TESLA superconducting accelerating cavities. The module is followed by a magnetic chicane bunch compressor[3], a second accelerating module, and a dipole magnet for energy measurements.

One important beam property is the longitudinal electron bunch shape. Peak currents of 2.5 kA as required for the TTF-FEL phase 2 can only be reached, if the bunches with a charge of 1 nC are compressed from initial 1 mm to 50 μm in the magnetic chicane bunch compressor [4]. For the proof-of-principle experiment, a bunch length of 250 μm is anticipated. In this report we present the measurement of the longitudinal profile of the beam produced by the injector with a high reso-

[1] on leave from INFN LASA, Milano, Italy

lution streak camera. The bunch length is determined by initial laser pulse shape and the relative phase of the gun to the laser. A second method is using Fourier transform spectroscopy. Proper dephasing the beam in the accelerating structure and the measurement of the energy spread in a dispersive section allow the reconstruction of the longitudinal pulse shape.

2. Streak Camera Measurements

The longitudinal bunch charge distribution can be determined single-shot, time-domain with a high resolution a streak camera [5]. Synchrotron light, emitted by the electron bunch, is transmitted by a set of aluminum mirrors onto the photo cathode (S-20) of the streak camera. The light transfer is done without focusing lenses since the intensity suffices. In the streak tube, the light pulse is converted to an electron pulse, which is accelerated and swept transversely by a fast rf electric field. The resulting transverse distribution is projected onto a phosphor screen. The image is amplified by a multi-channel plate and then detected by a CCD camera (Fig. 1).

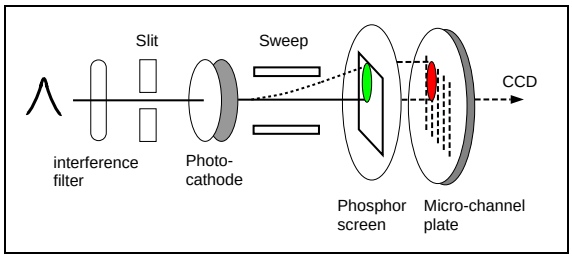

Fig. 1. Principle layout of the streak camera used in this experiment.

The streak camera has a temporal resolution of 2 ps. Space charge effects inside the streak camera tube and the available sweeping speed of 25 ps/mm limit the temporal resolution. The transverse beam size of the electron bunch is convoluted with the longitudinal electron bunch distribution during the sweep. To reduce the effect to a minimum, a narrow slit with a width corresponding to $\sigma = 2.61 \pm 0.01$ ps is used in streak direction. The slit size has been chosen large enough so that diffraction effects on the photo cathode can be neglected. The residual contribution of the transverse intensity distribution on the beam profile recorded by the streak camera has been deconvoluted during data analysis.

The bunch length obtained from an rf gun depends on both the laser pulse length and the compression occurring from the rf field within the first centimeters of the gun cavity. By proper choice of the rf phase a velocity modulation can be impressed on the electron bunch leading to a reduction of its length within the gun cavity. Leading electrons see a lower electric field than trailing electrons to obtain pulse compression. Very short bunches can be obtained at the price of sacrificing a large fraction of the bunch charge. The bunch charge and length is reduced by choosing an rf phase such that only part of the electrons in the bunch are subject to an acceleration. In an electron drive linac the latter mechanism is generally avoided because of the need of intense electron beams. During this experiment, the electron bunches are accelerated in the linac with the maximum accelerating field without the use of the magnetic bunch compressor chicane yielding an invariant bunch length behind the injector. Synchrotron light generated in the TTF spectrometer dipole magnet located at the end of the linac has been used to determine the bunch length.

The laser pulse length has been measured with the same streak camera. Since the laser beam has a wavelength of 262 nm, special UV transmitting optics have been used.

Laser Pulse Length Measurements Averaged over several measurements, the laser pulse length in the UV is $\sigma = 16.7 \pm 1.7$ ps. Figure 2 shows an examples of longitudinal laser shapes. The unexpected long laser pulse (left) was due to a problem with the pulse train oscillator of the laser during this experiment. After replacing the laser head, a pulse length of $\sigma = 7.1 \pm 0.6$ ps (right) was measured [6].

Electron Pulse Length Measurements Figure 3 (upper left and right) shows two examples of measured longitudinal electron bunch shapes using the streak camera . The rf gun was operated with a laser pulse length of 16 ps, a gradient of 35 MV/m and a bunch charge 3 nC. The shapes are fitted with a gaussian distribution as

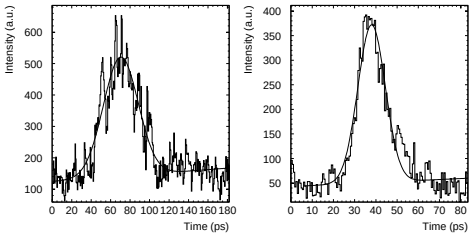

Fig. 2. Two examples of longitudinal laser bunch shapes measured with a streak camera in the UV (262 nm). The left shape is taken with the pulse train oscillator produced longer pulses than expected, the right shape is after repair. Indicated is a fit to a gaussian function giving a width of $\sigma = 17.81 \pm 0.01$ ps (left) and $\sigma = 8.0 \pm 0.01$ ps.

indicated by the solid lines. The upper left profile has been obtained for a gun phase (relative phase between rf gun and laser) of 25° yielding maximum bunch compression to $\sigma_z = 1.95 \pm 0.08$ mm without a significant reduction of the bunch charge. Figure 3 (lower left) shows the measured bunch length as a function of rf phase. The bunch length determined by a simulation of the bunch dynamics in the rf gun using PARMELA [7] is indicated with a solid line. It fits well with the data and confirms the understanding of the bunch compression due to the rf field in the gun. Figure 3 (lower right) shows the rms bunch length

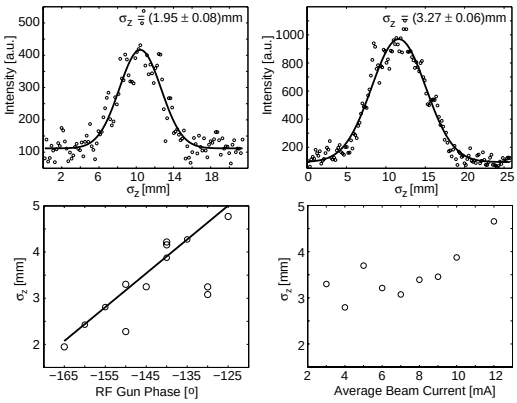

Fig. 3. Longitudinal electron bunch shapes measured with a streak camera for a gun phase of 25° (upper left) and 40° (upper right). The bunch length from a gaussian fit to the shapes is shown as a function of gun phase (lower left). The result of a simulation is indicated as a solid line. The lower right graph shows the bunch length for different bunch charges.

at a fixed gun phase 40° but for a variable bunch charge. The bunch length does not change significantly for bunch charges smaller than 8 nC, corresponding to a beam current of 700 A. For bunch charges exceeding 8 nC, a gradual lengthening is observed. This lengthening can be explained by longitudinal space charge forces whose strength is rising proportional to the bunch charge. At low energies, within the gun cavity, the strength of these additional forces suffice to enlarge the longitudinal beam dimension.

3. Energy Spread Measurement

Injector Energy Spread The energy spread measured at a beam energy of 16 MeV in the dispersive section of the photo injector by means of optical transition radiation yields an rms energy spread of $\Delta E/E = 1.9 \cdot 10^{-3}$. Together with the rms bunch length of $\sigma_z = 2$ mm a normalized longitudinal emittance of $\gamma\epsilon_z = 1920$ mm keV is obtained.

Linac Energy Spread The evaluation of the bunch energy distribution in the dispersive section at the end of the linac can be used to determine the bunch length. For this experiment, the electron pulses are accelerated off-crest in the first accelerating module (longitudinal transfer matrix M), are longitudinally compressed by a magnetic chicane compressor (longitudinal dispersion M_{56}) and accelerated (eventually) off-crest by a the second module (longitudinal transfer matrix R). The final energy spread $\sqrt{\bar{\sigma}_{66}}$ can be expressed in terms of the initial beam parameters, hence

$$\bar{\sigma}_{66} = R_{65}^2\tilde{\sigma}_{55} + 2R_{65}R_{66}\tilde{\sigma}_{56} + R_{66}^2\tilde{\sigma}_{66} + U_A^2\tilde{\sigma}_{55}^2 \quad (1)$$

where

$$\tilde{\sigma}_{55} = \sigma_{55}(1 + M_{56}M_{65})^2 + \sigma_{66}M_{56}^2M_{66}^2 + S_A^2M_{56}^2\sigma_{55}^2 \quad (2)$$

$$\tilde{\sigma}_{56} = \sigma_{55}\left(M_{65} + M_{65}^2M_{56}\right) + \sigma_{66}M_{66}^2M_{56} + S_A^2M_{56}\sigma_{55}^2 \quad (3)$$

$$\tilde{\sigma}_{66} = \sigma_{55}M_{65}^2 + \sigma_{66}M_{66}^2 + S_A^2\sigma_{55}^2 \,. \quad (4)$$

σ_{55} and σ_{66} denote the square of the initial rms bunch length and energy spread respectively. S_A and U_A denote the second order beam transfer

matrix elements of the off-crest rf acceleration

$$S_A = U_A = \frac{1}{2}\frac{dE\cos\phi}{E_0 + dE\cos\phi}\frac{2\pi}{\lambda} \qquad (5)$$

where dE, ϕ and λ denote the cavity gradient, phase and wavelength.

During the measurements, the injector was operated with a reduced laser pulse length of 7 ps, a gun gradient of 35 MV/m and a reduced bunch charge of 1 nC. For this measurements, the machine setup is a comparable to the setup used for the streak camera measurements discussed in the previous section, because the longitudinal space charge forces are identical in both cases. Longitudinal space charge forces scale with the bunch charge and inverse to the square of the bunch length, hence the laser pulse length. The rf gun phase yielding the shortest bunch length in the injector, see Fig. 3, has been chosen.

Measurements The energy spread measured behind the spectrometer dipole magnet, the phase and the gradient of the rf cavity strings have been used to determine the rms bunch length according to formulae (1 - 4). The result of a simulation, generating 10^5 possible σ_{66} for varying cavity gradient, cavity phase, initial bunch length and energy spread, is compared with the measurement. The simulation data sample is cut for the measured energy spread and rf parameters (within their measurement errors) yielding the evolution of the bunch length through the machine. Figure 4 shows the FWHM bunch length evolving through the magnetic chicane compressor. The shaded area indicates the error of the bunch length measurement at various positions within the chicane. The left plot shows a set-up with optimum compression from $\sigma_z = (920 \pm 80)\,\mu$m to the right plot an over-compression from $\sigma_z = (850 \pm 100)\,\mu$m to $\sigma_z = (500 \pm 180)\,\mu$m. The result of the measurements agrees well with the streak camera measurements taken into account, that the laser pulse length was reduced by a factor of 2 and at the same time, the contribution of longitudinal space charge forces during both measurements are identical.

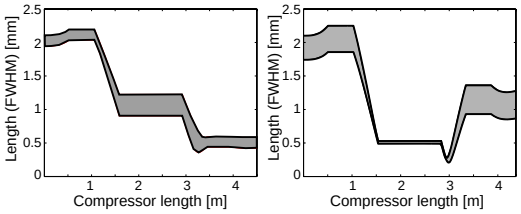

Fig. 4. FWHM bunch length through the magnetic chicane bunch compressor. The measured energy spread, rf cavity gradient and phase (within their error bars) are compared to a simulation with the initial bunch length and energy spread as free parameters. Left: Optimum compression. Right: Over-compression. The shaded area indicates the confidence of the bunch length measurement at various stages of compression.

4. Conclusion

The longitudinal electron bunch shape has been measured as a function of the relative phase of the rf gun and the laser beam. The bunch length predicted by a simulation of the beam dynamics in the rf gun fits well with the measurement. This support our understanding of an rf compression in the gun for low phases. A second method to determine the longitudinal bunch shape by measuring the bunch energy spread after the bunch traveled through 2 accelerating modules and a magnetic chicane compressor allows to reconstruct the evolution of the bunch length throughout the linac. The results are in good agreement with the streak camera measurements. For optimum compression, an injector bunch length of $\sigma_z = (920 \pm 80)\,\mu$m and a final bunch length of $\sigma_z = (260 \pm 50)\,\mu$m is achieved.

References

[1] S. Schreiber, "First Running Experience with the RF Gun based Injector of the Tesla Test Facility Linac", this conference.

[2] TESLA-Collaboration, ed. D.A. Edwards, "TESLA Test Facility Linac – Design Report", DESY Print March 1995, TESLA 95-01.

[3] M. Geitz, A. Kabel, G. Schmidt, "Bunch Compressor 2", Proc. of the 1999 Part. Acc. Conf., New York, 1999.

[4] "A VUV Free electron Laser at the TESLA Test Facility at DESY – Conceptual Design Report", DESY Print, June 1995, TESLA-FEL 95-03.

[5] ARP Streak Camera, now Photonetics GmbH, D-77694 Kehl, Germany.

[6] S. Schreiber et al., "Running Experience with the Laser System for the RF Gun based Injector at the Tesla Test Facility Linac", this conference.

[7] PARMELA, Version 5.0, B. Mouton, LAL, F–91405 Orsay, France.

Design and Performance of the Vacuum Chambers for the Undulator of the VUV FEL at the TESLA Test Facility at DESY

U. Hahn, P.K. Den Hartog[+], J. Pflüger, M. Rüter, G. Schmidt, E. M. Trakhtenberg[+]

Deutsches Elektronen-Synchrotron DESY, Notkestrasse 85, 22603 Hamburg, Germany

+ Advanced Photon Source, Argonne National Laboratory, Argonne, IL 60439

Abstract

Three vacuum chambers for the VUV SASE FEL undulator sections at the TESLA Test Facility (TTF) were designed, built, tested and installed. Each chamber is 4.5 m long and of 11.5 mm thick. The inner diameter of the beam pipe is 9.5 mm. The rectangular chamber profile with a width of 128mm is used to integrate beam position monitors and steerers. This is needed to provide a good overlap between the electron and the photon beam over the entire undulator length. The chambers are built in an aluminum extrusion technology developed for the insertion device vacuum chambers of the Advanced Photon Source. After manufacturing special processing was performed to reach low outgassing rates ($<1\cdot10^{-11}$mbar·l/sec·cm^2) and particle-free chambers. Mounting of the chambers at TTF were performed under clean room conditions better class 100.

Keywords: Vacuum Chamber, Undulator, Beam Position Monitor, Corrector Coils

1. INTRODUCTION

At the TESLA Test Facility (TTF) at DESY the phase I of the VUV free electron laser (FEL) [1,2] operating down to 42 nm, is completed. The major component for the generation of the FEL photon beam is the 15 m long undulator. It consists of three 4.5-m long sections with integrated strong focusing quadrupoles. These undulators are permanent magnet structures with a fixed gap of 12 mm. Each section contains a FODO structure of 10 quadrupole magnets[3]. To correct the errors of the 30 quadrupoles, an electron beam position monitor and a steerer is installed for each quadrupole. The diagnostic and steering inside the undulator gap is necessary to achieve a sufficient (< 12 µm) overlap[4] between the particle beam and the photon beam. The three undulator vacuum chambers with an open aperture of 9.5 mm guide the electron beam through the undulator sections.

2. Vacuum Chamber Design

There are several criteria which influence the design of the chamber:

- the particle beam position must be monitored with respect to the magnetic quadrupoles in the 12mm undulator gap over the whole length of the undulator.
- steering of the particle beam in the undulator gap by correction coils.
- a chamber support which guarantees a precise straight alignment of the chambers within 0.1mm and must not affect the precision alignment of the undulators.
- low electrical resistance and small microroughness of the inner beam pipe are needed to minimize resistive wall and wake field effects on the beam[5].
- the vacuum chamber has to fulfil the specifications for the cleaning of vacuum components[6] for the TTF.

- The specific outgassing rate after cleaning of the chamber should be in the range of 10^{-11} mbar·l/sec·cm^2

2.1 vacuum chamber

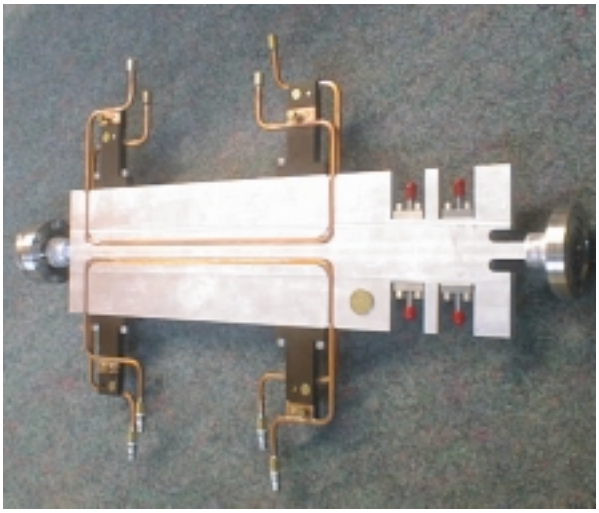

Figure 1: Prototype structure of the FEL vacuum chamber with steerers, pick up monitors and end flanges

The vacuum chamber is a flat long structure with the base dimensions of 11.5 mm x 128 mm x 4500. The central aperture for the beam has a diameter of 9.5-mm. The choice of aluminum as chamber material has the advantage of the low electrical resistance. Aluminum extrusion profiles specifically tailored for this application could be obtained. The previous Advanced Photon Source (APS) experience with the design of aluminum vacuum chambers for insertion devices was widely used [7]. Figure 1 shows the prototype structure of a single chamber period with four electrodes of a beam position monitor (BPM) and the four water cooled steerer windings. The pick up electrodes of the BPM are special UHV compatible RF feed throughs[8] which are connected to the chamber body using special all metal seals[9]. The chamber flange on the right hand is the longitudinal chamber fix point. The connection of the ConFlat flange to the chamber body is formed by a bimetallic welding joint and a flexible junction which allows an elastic bending of the flange for alignment purposes. A more detailed description of the manufacturing and cleaning of the chamber is given in [10].

2.2 monitors and steerers

In order to guarantee a tough control of the electron beam orbit inside the undulator one BPM and corrector are required per FODO quadrupol (every 0.478m). All these components have to fit inside the 12mm undulator gap. In total 10 BPM's and 9 correctors are required per undulator chamber.

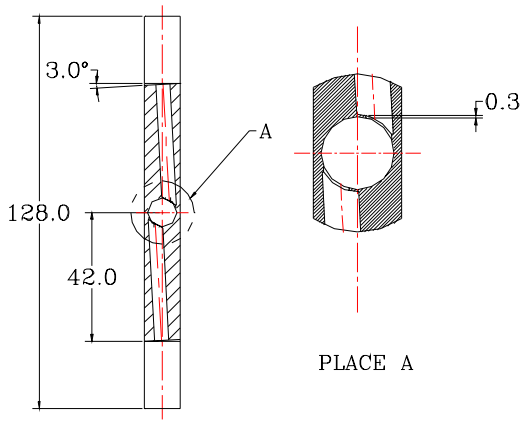

Figure 2: Cross section of the vacuum chamber at the position of the waveguide BPM.

Two kinds of BPM's will be used[11]. For TTF phase I inside the first two chambers button type pick up monitors will be used. These monitors were successfully tested at the CLIC facility at CERN.

Figure 3 : The prototype chamber profile with the waveguide monitor which will be installed in the third chamber

For the 250µm long bunches which will be available in Phase I these monitors are believed to be a safe and reliable system . For even shorter bunches new solutions have to be found. Therefore in the chamber of the third undulator segment a new type of monitor will be tested which has been

described in[12]. It uses outcoupling slits inside the vacuum chamber and waveguides to detect the exact position of the electron beam. These monitors decouple the beam induced RF through four small RF windows. The position information is derived from the four signals. In contrast to the button type monitor this method is not restricted by a lower limit of the bunch length. This new design has a large potential for a use in Phase II when the bunch length will be further reduced to 50µm. The drawback of the waveguide type monitor is its complicated design. It requires complex contours to be manufactured inside the undulator chamber. A more sophisticated RF detection electronics allows to define the relative beam position within a few µm. Successful tests of the first prototype at CERN and the second improved design at DESY have proven the capability of this monitor type. Figure 2 and 3 show the waveguide monitor design after machining by an electrical discharge machining (EDM) process. At the end of the U-type waveguide an asymmetric window couples into the beam pipe.

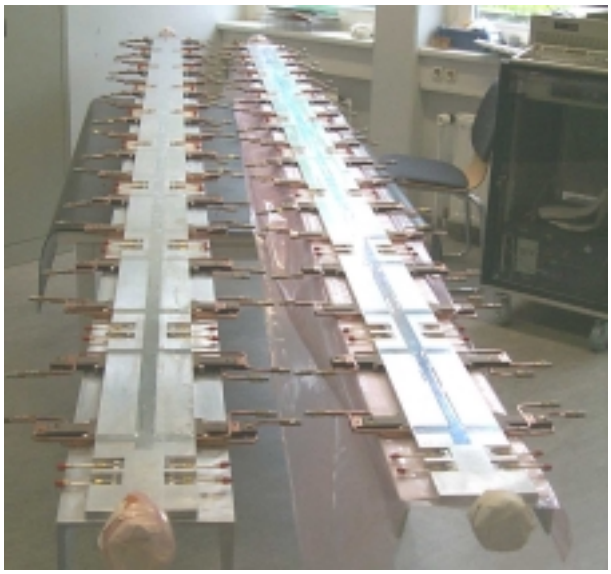

Figure 4: Two vacuum chambers ready for installation into the undulator.

The correctors coils are located in between the BPM's. The generation of corrector fields to the electron beam is complicated by the presence of soft iron poles inside the undulator and soft iron girders. So no external coils could be used. Therefore the so called "Four Wire Steering" principle was chosen. Per corrector there are four single turn coils of 0.3m length.. They are made from a 4×4×2.5 mm hollow copper profile which is insulated against the vacuum chamber. All four wires are grouped symmetrically around the electron beam tube and are inside the undulator gap. These four wire steerers can in principle provide horizontal and vertical steering when properly connected to two power supplies. But it was found sufficient that horizontal steering is applied for the horizontal focusing quadrupoles and vertical steering for the vertical ones. Only the last corrector in each chamber is a double steerer as described above. In this way five horizontal and five vertical steerers are available in each undulator segment. The steering strength of one corrector is about 0.3 Tmm. The hollow copper coils are connected to cooling water which transports off the ohmic heat produced by the current in the corrector coils and RF losses caused by the BPM's. A worst case estimate for the total dissipated power is less than about 30W. A second purpose of the cooling is to thermally stabilize the undulator chamber in order to avoid temperature gradients through the undulator. Therefore the temperature of the cooling water is controlled by precise thermostats.

2.3 The support structure

Special mounting, alignment and supporting systems for the flat and longitudinal very flexible chamber were designed and built.

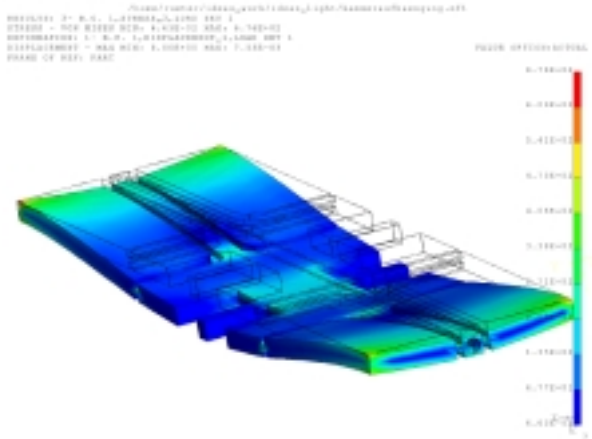

Figure 5: The FEM calculation shows the vertical displacement of one chamber period between two chamber supports. It is smaller than 10 µm

The chamber is flanged directly to the diagnostic block on one side. This defines the longitudinal position of the chamber. In the undulator the

chamber is hold by 9 cardanical sliding supports which are connected to the undulator support system. Each support allows to align the chamber within a tenth of a mm in vertical and horizontal direction. The number of supports were defined by finite element model calculations. Figure 3 shows the calculation for one supporting period. The vertical deviation due to gravity bending is of the order of 6 μm.

3. Chamber mounting

Since the chamber tube must reach a specific outgassing rate $<1\cdot10^{-11}$mbar·l/sec·cm^2, careful cleaning of the chamber is mandatory. To fulfil the stringent particle free requirements of the TTF cleaning, assembling, and mounting of the chamber was made inside a clean room better than class 100. This chamber processing step was done at the APS[10].

Figure 6: The insertion of the vacuum chamber

A special problem was the insertion of the chamber in the undulator gap. A special 4.5 m long sliding system was built. After alignment the chamber was moved into the undulator gap (see Fig. 6) and then connected to the chamber support. The vacuum chamber together with the undulator module were transferred into the TTF linac tunnel. The vacuum connections to the monitor blocks on both ends of the vacuum chamber were made in a local clean room better class 100. After pumping down of the undulator vacuum system at the undulator ends a pressure $< 2\cdot10^{-8}$mbar was reached.

4. Conclusion

Three FEL vacuum chambers were successfully installed in the undulator section of the TTF linac. The vaccuum system has reached the anticipated pressure, so that the first FEL beam can be produced.

References

[1]J. Roßbach, Nucl. Instrum. and Methods A 375, 269 (1996)

[2]J. Feldhaus and B. Sonntag Synchrotr. Rad. News 11, 1, 14 (1998)

[3]Yu. M. Nikitina and J. Pflüger, Nucl. Instrum. and Methods A 375, 325 (1996)

[4]B. Faatz, J. Pflüger, and Yu. M. Nikitina, Nucl. Instrum. and Methods A 393, 380 (1997)

[5]see J. Pflüger, these proceedings

[6]D. Edwards, D. Hubert, A. Matheisen, H. P. Wedekind, H. Weise, and K. Zapfe-Düren, " Proposed Cleaning Procedures for the Vacuum Components for the TESLA Test Facility", TESLA report 15(1997)

[7]P. Den Hartog, E. Trakhtenberg, G. Wiemeslage et al., " Advanced Photon Source Experience with Vacuum Chamber for Insertion Devices", PAC 97, Vancouver, Canada, 12-16 May 1997.

[8] KAMAN Instrumentation Corporation, USA

[9] VATSEAL, VAT Vakuumventile AG, Schweiz

[10] U. Hahn, J. Pflüger, M. Rüter, P. Den Hartog, E. Trakhtenberg, G. Wiemeslage et al., " The Vacuum Chambers for the VUV SASE FEL at the TESLA Test Facility at DESY ", PAC 99, New York, USA, March 29 – April2, 1999.

[11]R. Lorenz, T. Kamps, U. Hahn, and M. Wendt, "Beam Position Monitors inside the FEL – Undulator at the TTF Linac", PAC 97, Vancouver, Canada, 12-16 May 1997

[12]T. Kamps, R. Lorenz, et. al "Design and Test of a new Beam Position Monitor for the Undulator of the TTF-FEL", Proceedings of the EPAC98, Stockholm, Sweden, 1998

[13]P. Castro, Proceedings of the EPAC98, Stockholm, Sweden, 1998

Test Results on the Silicon Pixel Detector for the TTF-FEL Beam Trajectory Monitor

S. Hillert [a], R. Ischebeck [b], U. C. Müller [b], S. Roth [b], K. Hansen [b], P. Holl [c], S. Karstensen [b], J. Kemmer [c], P. Lechner [c], J. S. T. Ng [b], L. Strüder [d]

[a] *II. Institut für Experimentalphysik, Universität Hamburg, D-22603 Hamburg*

[b] *Deutsches Elektronen-Synchrotron DESY, D-22603 Hamburg*

[c] *Ketek GmbH, Am Isarbach 30, D-85764 Oberschleißheim*

[d] *Max-Planck-Institut für extraterrestrische Physik, Giessenbachstraße, D-85740 Garching*

Abstract

First tests of the silicon pixel detector for the beam trajectory monitor (BTM) at the Free Electron Laser (FEL) of the TESLA Test Facility (TTF) at DESY are presented. Measurements using 6 keV photons of the manganese K_α/K_β line allow to determine the electronic noise of detector and read-out and to calibrate the signal amplitude of different pixels. The sensitivity of the silicon detector to low energy X-rays down to 60 eV is shown. The accuracy of its position measurement is found to be better than 0.22 μm using a pulsed diode laser beam focused to a straight line

1. Introduction

In order to achieve the high brightness promised by the single-pass Free Electron Laser (FEL) [1] at the TESLA Test Facility (TTF), the electron beam position must be controlled to better than 10 μm over the 15 m long undulator.

With the beam trajectory monitor (BTM) [2] the off-axis spontaneous undulator radiation is detected through a set of pinholes by high resolution silicon pixel detectors. The sensitive area of the silicon pixel detector consists of two rows of each 12 active pixels as shown in Figure 1. To achieve the required resolution of the BTM the center of the photon spot has to be measured with a precision of 1 μm. The behaviour of the silicon pixel detector with respect to noise, quantum efficiency and spatial precision is presented.

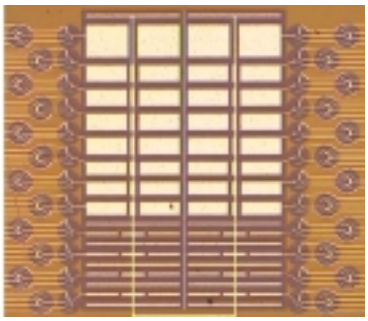

Fig. 1. Anode structure of the silicon pixel detector; two pixel rows with a charge injection line across each row.

2. Calibration and Noise Determination

An absolute energy calibration of each detector pixel is obtained using 6 keV photons of the manganese K_α/K_β line from a ^{55}Fe source. The resulting calibration constants agree for neighbouring left and right pixels within 1%–4%. The Gaussian width of the pedestal peak is mainly caused by one source of noise, namely the leakage current. As expected we find that the noise grows proportional to the square root of the integration time and decreases by a factor of two when cooling the detector by 16 K. A noise charge (ENC) of about 50 e has been achieved at room temperature with an integration time of 20 μs.

3. Sensitivity to VUV Light

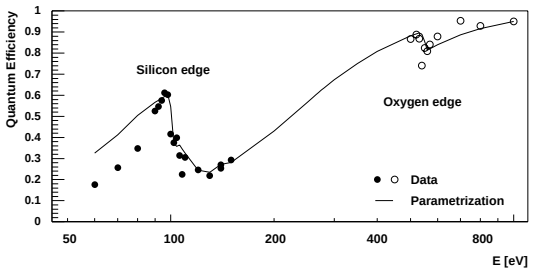

Fig. 2. Quantum efficiency for VUV radiation

The quantum efficiency of the silicon pixel detector was measured using a VUV beam at the synchrotron light source facility HASYLAB. It was illuminated with monochromatic light in the energy range of 50 to 1000 eV. The silicon detector response was normalized to the photo-electron emission of one of the focusing mirrors and the signal of a GaAs photodiode with known quantum efficiency as a reference. The observed reduction of quantum efficiency near the absorption edges (Fig. 2) can be explained by dead layers of 50 nm of silicon oxide and 30 nm of silicon, which have to be passed by the photons before they enter the sensitive region of the detector. For the energy region that will be used in TTF-FEL the quantum efficiency lies above 20%.

4. Position Resolution

The systematics of the position measurement of the pixel detector is studied by projecting a laser line-optic onto the pixel structure. The Gaussian width of the laser line (24 μm) is in the same range as the light spot that we expect in the TTF-FEL setup. Stepping the laser line (0.07 μm per step) across the two pixel rows allows to reconstruct the straightness of the laser line. For each pixel pair the relative difference between the signals of the left and right pixel, $\eta = (S_R - S_L)/(S_R + S_L)$, is calculated. For positions very close to the zero crossing one expects a linear dependence of η on the stepper position (Fig. 3). A periodic oscillation of 0.5 μm length is observed, which is caused by the inaccuracy of the stepping device. For every pixel pair the position of the zero crossing of η can be extracted from a fit of a straight line to the data points. Comparing these positions one gets agreement between the pixel pairs within a standard deviation of 0.22 μm.

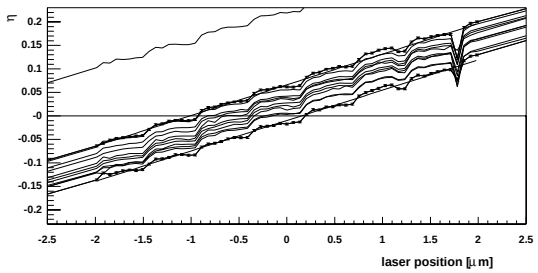

Fig. 3. Measurement of η versus the laser position

References

[1] TTF-FEL Conceptual Design Report, TESLA-FEL 95-03, DESY, June 1995;
J. Rossbach *et al.*, Nucl. Instrum. and Methods **A375** (1996) 269.

[2] J.S.T. Ng, TESLA-FEL 96-16, DESY, 1996;
AIP Conf. Proc. #413, eds R. Bonifacio and W. A. Barletta, 1997;
Proc. of the 8th European Symposium on Semiconductor Detectors 1998, to be published in Nucl. Instrum. and Methods A.

Calibration of Waveguide Beam Position Monitors

T. Kamps

DESY Zeuthen, Platanenallee 6, D-15738 Zeuthen, Germany

Abstract

To ensure overlap between the photon beam and electron beam at the SASE-FEL at the TESLA Test Facility [1], several position sensitive diagnostics components are installed along the beamline of the FEL. For the undulator part, a new type of waveguide beam position monitors (BPMs) is designed, tested, and installed inside the beam pipe of one undulator module. This paper proposes a method to calibrate these monitors with beam based measurements

1. Introduction

The waveguide beam position monitor (BPM) system for one undulator module consists of ten individual BPM units, each with four coupling channels. The operation principle of the BPM is based on the coupling to the magnetic field co-propagating with the electron beam with small slots in the aperture [2]. Fig.1 shows a schematic profile of one BPM unit in the plane perpendicular to the beam direction.

The output data from a BPM shows the electron beam offset relative to the electrical center of the BPM, not to the geometrical. The electrical center may drift due the imbalance among the output signals, because signals must travel through different paths, transducers, cables and signal processing electronics elements, and are then measured by detectors. To find the relation between the geometrical and electrical centers is the object of the calibration. This paper proposes a method to estimate the imbalance from four output signals of one BPM unit using beam signals.

2. Modelling BPM Output Signals

Assuming that the overall effect of transducer, cables, and electronics elements can be described by a gain factor g_i, which is unique for each BPM unit channel, the amplitude of the beam induced signal V_i from a bunch charge q at a position (x, y) reads like

$$V_i = q \cdot g_i \cdot F_i(x, y),$$

where the response function $F_i(x, y)$ describes the response of a particular slot. This response function can be calculated analytically via the beam induced wall current density model [3]. The wall current on a spot (b, α) on a circular beam pipe with radius b at an angle α induced by a beam charge q with current I_b at (r, θ) can be expressed with

$$I_w(r, \theta) = \frac{I_b}{2\pi b} \cdot \frac{b^2 + r^2}{b^2 - r^2 - 2br\cos(\alpha - \theta)}$$

in a cylindrical reference frame centred in the BPM. In a circular region $r \leq b$ the response

function can be given by the wall current density at the location of the coupling slot sensitive center normalised to the beam current. For cartesian coordinates the response function for a beam at (x, y) for the ith slot of a BPM reads

$$F_i(x,y) = \frac{b^2 - (x^2+y^2)}{b^2 + (x^2+y^2) - 2(x_s x + y_s y)}. \quad (1)$$

with slot position (x_s, y_s). This function is normalised to $F_i(0,0) =$. Further analysis is based on two assumptions. One is that the response function will not change in time. Since the response function only depends on the geometrical structure of the BPM, and in particular on the location of the sensitive centers of the coupling channels, this is reasonable. The second assumption is that all effects which displace the electrical center relative to the geometrical center can be included into the gains g_i. This assumption is acceptable when the amplification by the signal processing electronics is stabilised by an internal feedback. When all g_i's are known, the offset between electrical and geometrical monitor center is determined. This idea can be applied to the calibration of a BPM unit itself for modelling its response function [4].

3. Gain Estimation

Considering $j = 1 \cdots m$ measurements for the induced voltage into all channels for m different beam positions. Then, the voltage from the ith channel at the jth measurements is

$$V_{ij} = g_i \cdot q_j \cdot F_i(x_j, y_j) \quad (2)$$

where $F_i(x_j, y_j)$ is the response function for an ideal BPM channel for an electron beam at the position (x_j, y_j) according to Eq.1. Because only the relative imbalance between all gains is of interest for calibration, g_1 can be set to 1, resulting in 3 unknown parameters for the gains (g_2, g_3, g_4). Beside this, for each measurement a set of $3m$ unknown parameters (q_j, x_j, y_j) is generated while $4m$ quantities $(V_{1j}, V_{2j}, V_{3j}, V_{4j})$ are measured. At $m = 3$ measurement the system of equations has a unique solution, for $m > 4$ the number of known parameters exceeds the number of unknowns. Using a nonlinear multiparameter chi-square method the $3m + 3$ unknown parameters, including the gains, can be estimated. Rewriting Eq.2 to

$$V_{ij} = g_i \cdot q_j \cdot F_i(x_j, y_j) \equiv V(i, j; \mathbf{a})$$
$$i = 1 \cdots 4 \qquad \text{and} \qquad j = 1 \cdots m$$
$$\mathbf{a} = (g_2, g_3, g_4, q_1, x_1, y_1, \cdots, q_m, x_m, y_m)$$

where $\mathbf{a}$ is the array of fitting parameters to be determined. This can be estimated by minimising the chi-square function

$$\chi^2(\mathbf{a}) = \sum_{i=1}^{4} \sum_{j=1}^{m} \frac{[V_{ij} - V(i,j;\mathbf{a})]^2}{\sigma_{ij}^2}$$

where σ_{ij}^2 is the error of the ith channel at the jth measurement and is assumed to be equal for all measurements and thus negligible. The diagonal elements of the covariant matrix build by second derivatives to each fit parameter of the chi-square function are the errors of each fitted quantity.

4. Test with Measured Data

The method described was tested with data from testbench measurements with a prototype BPM. The prototype BPM is mounted on a twodimensional precision stage with a wire strung coaxially through the BPM. A beam simulating TEM-wave is induced into the system, and all four output signals are detected and recorded. With this setup mapping scans have been performed on a square field with 1.2 mm edge length and 20 μm step width. The relative error for each voltage measurement is 0.25% and the signal source amplitude jitter is 1% of the peak value.

Several seeds of five, eight, and twelve position were randomly drawn from the data field, simulating five, eight, and twelve different orbit measurements with randomly spread beam positions in the transverse plane of the BPM. Fig.2 shows a typical result for a five point random selection.

There is a systematic offset between set and back calculated wire positions. This offset is caused by an imperfect alignment of the wire with

respect to the mechanical center of the BPM. After correcting the set values for this offset, a typical result for an eight point selection is depicted in Fig.3 showing good agreement between set and back calculated wire position.

In total, 30 seeds were tested and convergence was always reached. The average error for the fitted wire position is $\sigma_{fit} = 8$ μm and $\sigma_{offsety} = 15$ μm for the average offset error resulting in a total error of $\sigma_{tot} = 17$ μm. In Tab.1 results for estimated gain factors are summarised.

The average bunch charge parameter was calculated to $q = 88.7 \pm 0.6$, where error reflects the jitter of the signal source.

5. Conclusion

Tests values from testbench measurements show that the proposed procedure is useful to determine beam positions in an absolute reference frame centred in the geometrical center of a BPM.

References

[1] *A VUV Free Electron Laser at the TESLA Test Facility Linac – Conceptual Design Report*, DESY Hamburg, TESLA-FEL 95-03, 1995.

[2] T. Kamps, R. Lorenz, S. deSantis, *Microwave Characeterization of the Waveguide BPM*, Proc. of the PAC99, New York, 1999.

[3] J. H. Cuperus, *Monitoring of Particle Beams at High Frequencies*, NIM 145 (1977) 219-231, 1977.

[4] K. Satoh, M. Tejima, *Recalibration of Position Monitors with Beams*, Proc of the PAC95, Dallas.

Table 1
Results for gain factors.

Quantity	Fit Estimate		
g_2	1.1920	$\pm$	0.0143
g_3	0.7684	$\pm$	0.0115
g_4	0.9705	$\pm$	0.0059

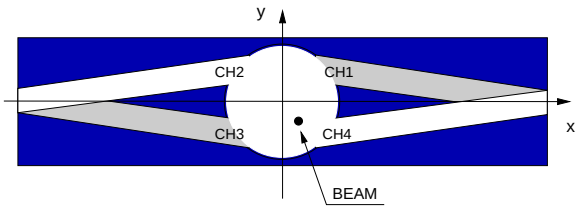

Fig. 1. Waveguide BPM profile.

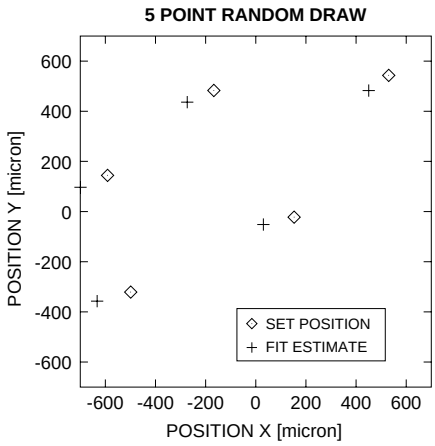

Fig. 2. Set and back calculated wire positions.

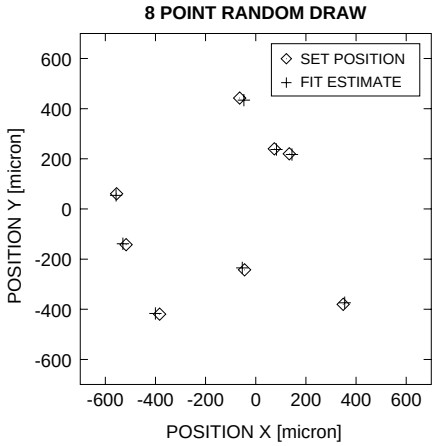

Fig. 3. Corrected set and back calculated wire positions.

High Quantum Efficiency Photocathode Preparation System for TTF Injector II

P. Michelato, C. Gesmundo, D. Sertore[a]

INFN Milano-LASA, Via F.lli Cervi 201, 20090 Segrate (Milano), Italy

[a] DESY, Notkestrasse 85, 22607 Hamburg, Germany

Abstract

The TESLA Test Facility (TTF) Injector II photocathode preparation system is in operation since spring 1998. High quantum efficiency tellurium and alkali metals based photoemissive films are routinely produced at Milano with typical 10% quantum efficiency (QE). Photocathodes are then successfully transported with no QE degradation, using a handy ultra high vacuum (UHV) system, to DESY and here transferred to the RF gun. The main characteristics of the system and the future developments are here discussed.

1. Introduction

During winter 1998/99 the Injector II was commissioned at the TESLA Test Facility LINAC (TTF) [1]. The new electron source is a laser driven RF gun based on cesium telluride photocathodes in place of the thermionic source used with Injector I.

The photocatodes are produced at Milano and used at DESY, hence a fully UHV split system was developed.

Due to the high sensitivity of these materials to gas exposition [2], they are always stored, from their production to their operation into the gun, in UHV condition. Moreover, thanks to the experience on cathode production and vacuum technology of our group, we have designed and built an handy transport system whose main peculiarity is to preserve cathodes in UHV condition during their travel from Milano to DESY.

A significant effort has been dedicated to the movements of the cathode in the UHV environment. The final design consisted of an evolution of the system we realized for the A0 experiment at Fermi National Laboratory [3].

The new cathode preparation system is equipped with all the diagnostics that are necessary for characterizing the cathodes produced, before their delivery to DESY. Here the installed system is mainly used to transfer the cathode from the transportation system to the gun.

The preparation chamber is discussed in the following section together with the material choice for the moving parts in vacuum (needed for cathode manipulation). The transportation system is presented in the third section. The DESY transfer system is the subject of the fourth section; a final discussion of the performances and future improvements of the whole system concludes the present paper.

2. The preparation chamber

The preparation chamber was designed to allow different tasks: cathode preparation, photoemissive property characterization and finally cathode manipulation. A sketch of the preparation chamber is presented in Fig. 1. An UHV chamber pumped by a 400 $l s^{-1}$ ion pump mainly composes it. In Fig. 1, the region "A" shows the cathode preparation and characterization area. In this area a photoemissive layer is deposited on a Molybdenum substrate. The cathode deposition process has been already extensively discussed elsewhere [4]. The tellurium and the alkali metals sources are installed on a frame in front of the masking area. The adjustment of the current, flowing through the sources, controls the evaporation process. An LTM (Linear Transfer Mechanism) moves the Molybdenum substrate in the deposition area. A second LTM translator (Fig. 1 "B") moves the cathode heater, a halogen lamp, together with a thermocouple into the back of the substrate. A feedback loop, between the thermocouple and the halogen lamp power supply, allows a substrate temperature stabilization within 1 °C. Another LTM moves the thickness monitor (a microbalance) from the top of the chamber into the evaporation area, exactly in the cathode position, for source calibration (Fig. 1 "C"). A remarkable feature of this system is the possibility to change the shape of the photoemissive area over the Molybdenum substrate. This possibility can be used to explore the dependence of the injector emittance on the source parameter. As an example, a photoemissive area smaller than the laser spot size avoids the diffraction effects otherwise coming from the laser beam shaping.

In the area between the sources and the masking, an anode, placed in front of the cathode, gives the possibility to measure the photocurrent. During the deposition, it

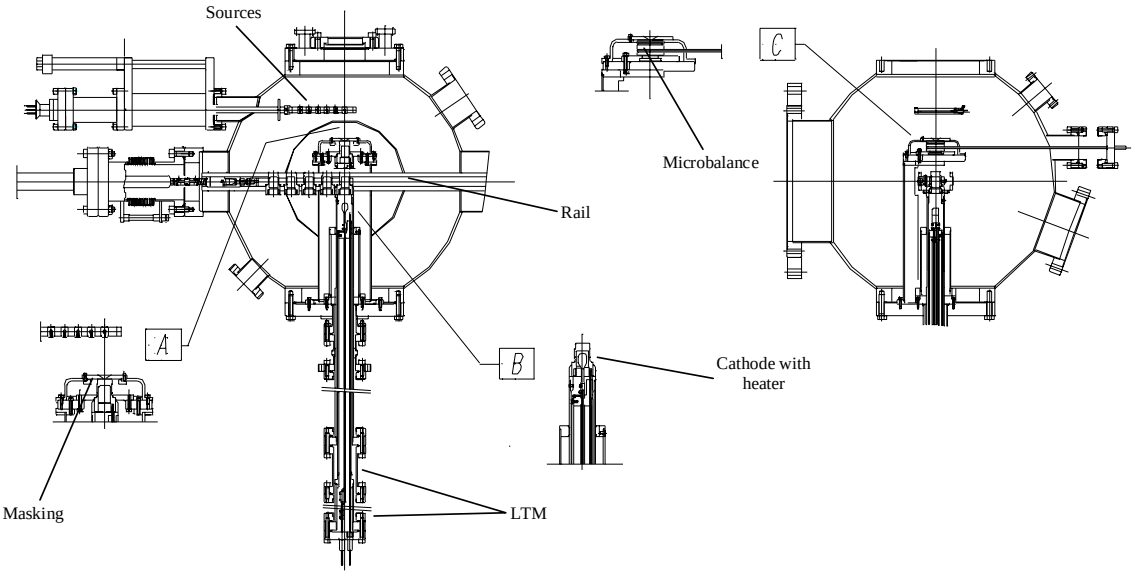

Fig. 1. Preparation system sketch. The cathodes are produced and characterized in the area with the label “A”. The area label “B” shows the LTMs used for moving and heating the cathode. Finally area “C” shows the microbalance and its position when inserted in place of the cathode.

allows the monitoring of the QE. For this purpose a Hg lamp with interference filter (λ= 254 nm) is used. After the cathode production, the spectral response and the QE distribution over the cathode area are measured. Moreover a beam steering system scans the cathode area by moving over it the light beam. In this way, a map of the QE is performed and non-uniformity in the photoemissive film can be detected.

For the movement of the cathode inside the system, a proper carrier has been designed: it holds up to five cathodes. Magnetic coupled translators are used for moving the carrier; upper and lower rails guide it along the entire path from the preparation system to the transportation system. Ball bearings are located on the upper and lower part of the carrier in order to decrease the friction during the movement. CuBe and Stainless Steel (SS) bearings has been used, both with no lubricants: SS ball bearings have shown longer lifetime and reliability. Additionally, spacers in CuBe, mounted on the lower part of the carrier, allow its centering in respect to the guiding sections. The cathode is locked on the carrier by three stainless steel plungers, positioned at 120° one respect to the other. To move the cathode in the different areas of the chamber, proper pincers, able to be coupled with the cathode, have been designed. Two sapphire balls are used for centering the cathode on the pincer. They are loaded with Tungsten springs and mounted on opposite sides in correspondence to two groves machined on the cathode. Fig. 2 shows a detail sketch of the cathode machining.

The preparation chamber and all its components have been assembled at Milano during winter 1997/98 and since then they are operative. Until now, ten cathode have been produced and four of them were successfully transported to DESY.

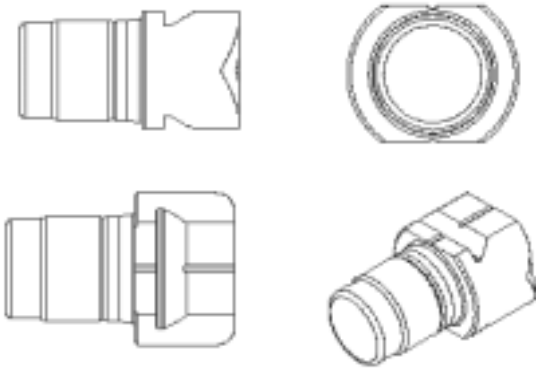

Fig. 2. Details of the cathode machining. From the left down clockwise, a top view with the groves for the plungers, a detailed view of the machining for the coupling with the pincer, and the insertion hole for the heating lamp on the back of the cathode. The last insert is a 3D view where the complex machining of the cathode is visible.

3. The transportation system

The transportation system has been developed to move the photocathodes from Milano to DESY in UHV condition. To accomplish this task, a CF 63 six ways cross was modified in order to contain the cathode carrier. A 60 $l \cdot s^{-1}$ ion pump maintains the system in UHV. Fig. 3 shows a sketch of the transportation system.

To disconnect the carrier from the magnetic manipulator, a bayonet coupling device has been designed. This device allows a fast and reliable connection and detachment of the carrier from the manipulator. A small translator takes in position the carrier during the transportation, inserting a catch in the back of the last cathode. In front of the cathode, an anode and a Fused Silica viewport allow the photocurrent measurement. This is particularly important because no photocathode diagnostic device is available in the transfer system at DESY.

In order to connect the transportation system to the other systems without breaking the vacuum, a CF 63 all metal valve is installed. Another all metal valve is mounted on the other system and a small transition piece allows the connection. This transition piece is the only one, in all the apparatus, that is exposed to air when the transportation system has to be connected or disconnected. To speed up the pumping time a LN_2 (Liquid Nitrogen) trap is foreseen. The typical time necessary to connect the transportation system is about half an hour while the pump down time for the connection

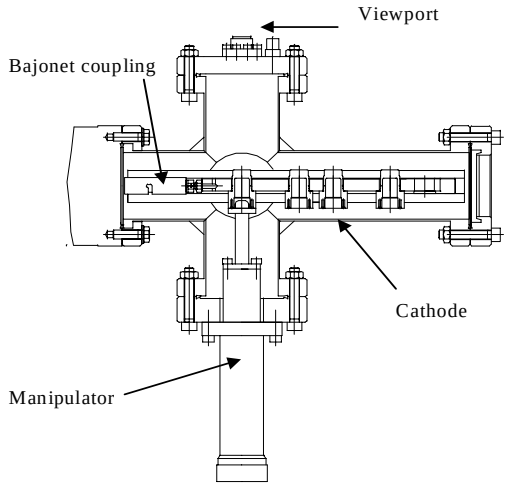

Fig. 3. Sketch of the transportation system. From the left, the bayonet device and then the small manipulator are drawn. In front of the last cathode in the carrier is the small viewport for QE measurement.

piece is of the order of one day before UHV conditions are established (without the LN_2 trap).

As mentioned in the introduction, one noticeable feature of the transportation system is its compactness. During the transportation, a small DC/DC converter supplies the ion pump. We are currently using a modified Penning power

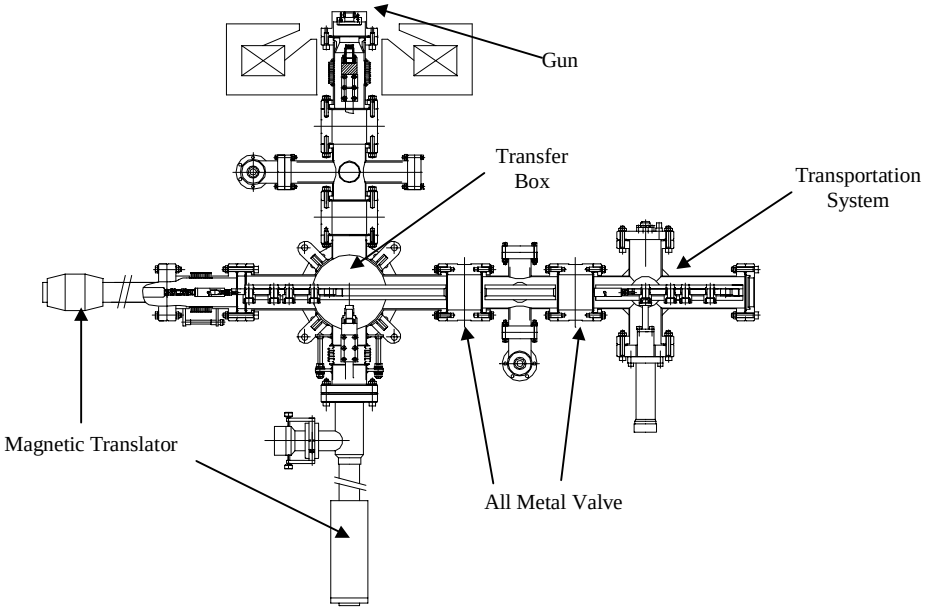

Fig. 4. Top view of the transfer system. The transportation system is connected on the right and a long magnetic coupled translator moved the carrier in the main chamber where a second manipulator moves the selected cathode into the gun.

supply powered by a battery. Since the current drained by the ion pump is very low, the battery is sufficient for the time needed to transport the cathode. The first cathode transportation was done on July 1998 without any degradation of the QE properties of the cathode, as reported at this conference [6]. A second cathode transportation followed in December 1998 with the same good results.

4. The transfer system

The transfer system is installed at DESY and is directly connected to the RF gun: it allows cathodes being transferred from the transportation system to the gun (Fig. 4). It mainly consists of an UHV chamber pumped by a 60 $l \cdot s^{-1}$ ion pump and a Titanium Sublimation Pump (TSP). A long arm magnetic coupled translator moves the carrier from the transportation chamber to the main chamber. Here a pincer, similar to the one used in the preparation system and mounted on a second translator, removes the cathode from the carrier. Non magnetic materials have been used for all the pincer components to avoid any influence on the gun performances. Once the second manipulator held the cathode, it is moved into the gun. The vacuum piping from the transfer system to the gun has been designed to guide and center the cathode in respect to the gun while the cathode itself is moving toward it. To avoid any damage to the photoemissive surface, all the guiding is done in respect to the outer dimensions of the pincer. The final centering of the cathode into the gun is achieved using a spring installed into the gun itself. Up to now two types of spring are used: a watch-bend type copper beryllium silvered spring is installed in the DESY gun while a standard copper beryllium round spring is mounted on the FNAL gun. The alignment of the cathode front surface in respect to the gun inner wall is ensured by a precision machining both of the cathodes and of the back plain of the insertion piece. In this way, only a final fine adjustment of the cathode position is needed in order to tune the frequency of the RF gun.

The transfer system is operative at DESY since July 1998 and has been used, at first, on the DESY RF gun and then assembled on the beam line and connected to the FNAL RF gun. It is operative since November 1998.

5. Conclusions

The system is fully operative since one year and no major problems have been detected. Cathodes are routinely produced and characterized at Milano. The cathode transportation has been successfully accomplished without any QE degradation and the transfer system is fully operative at TTF. New developments are foreseen in the carrier designed and in the transportation system. The critical point of the system is the carrier transfer from the transportation system to the other ones (preparation chamber and transfer system). Furthermore, the removing of the cathode from the carrier itself would be improved. In order to have an easier cathode handling, a new carrier has been designed with a different positioning of the cathode holders. The new design has been based also on the results of calculation done on the carrier balancing providing a safer movement of the carrier itself in the systems. The new cathode transfer system has been designed and will be delivered to DESY in fall 1999. This system is designed for the gun test stand. All the components are now at Milano and the assembling will take place after summertime.

6. Reference

[1] S. Schreiber, 'First running experience with the RF Gun based Injector of the TESLA Test Facility Linac', this conference.

[2] A. di Bona, F. Sabary, S. Valeri, P. Michelato, D. Sertore and G. Suberlucq, J. Appl. Phys. **80**, 3024 (1996)

[3] J.-P.Carneiro *et al*, 'First results of the Fermilab high brightness RF Photoinjector', Proceedings PAC '99, New York, 2027.

[4] P. Michelato, C. Pagani, D. Sertore, A. di Bona and S. Valeri, NIM A **393** (1997), 464.

[5] D. Sertore, S. Schreiber, K. Floettmann, F. Stephan, K. Zapfe and P. Michelato, 'First operation of Cesium Telluride photocathodes in the TTF Injector RF Gun', this conference.

[6] D. Sertore, S. Schreiber, K. Floettmann, F. Stephan, K. Zapfe and P. Michelato, 'First operation of Cesium Telluride photocathodes in the TTF Injector RF Gun', this conference.

Non-linear processes and multi-photon ionisation of clusters with VUV-FEL radiation

T. Möller, P. Gürtler, T. Laarman, W. Laasch and J. Schulz[#]

Hamburger Synchrotronstrahlungslabor HASYLAB am Deutschen Elektronensynchrotron DESY, Notkestr. 85, 22603 Hamburg, Germany

[#]II. Institut für Experimentalphysik, Universität Hamburg, Luruper Chaussee 149,

22761 Hamburg, Germany

The Free Electron Laser (FEL) presently under construction at DESY is expected to provide very intense photon pulses in the vacuum ultraviolet (VUV) and soft x-ray spectral range. This offers new experimental opportunities for the investigation of multi-photon ionisation and optical non-linear processes since all studies in this field were so far restricted to rather small photon energies.

Here we propose a study of non-linear processes and multiphoton ionisation on free clusters in a molecular beam. Thanks to fast sample renewal clusters in a beam allow the study of condensed matter without the problem of sample destruction. Furthermore, results for clusters can be directly compared with findings obtained in a separate set of measurements for atoms ore molecules using the same set-up. In the first phase of the experiment it is intended to study Xe and Kr clusters which are held together by van der Waals forces. Recent experiments on rare gas clusters excited with high power infrared (IR) lasers show that optical non-linear processes like high-order harmonic generation or multi-photon ionisation exhibit new features remarkably different from what observed in atomic beams. The energy distribution of electrons emitted from the clusters is shifted to higher energies with respect of that of atomic beams.

The intense and high energetic radiation from the FEL at DESY is expected to open new areas of research in this field. While so called ‘above threshold ionization’ is the dominant process with IR this channel is expected to be inefficient for high photon energies since the frequency of the radiation is fast compared to the frequency of electron motion. With VUV and soft-x-ray radiation the following experiments are particularly interesting:

1. Resonant multi-photon ionisation can be performed. We intend to selectively excite clusters either at the surface or in the interior by choosing the well-known energies. Thus, it can be expected that new types of fragmentation and coulomb explosion processes can be observed.
2. The energy redistribution inside the cluster ions can be investigated with fluorescence spectroscopy. This allows the determination of the temperature in the micro plasma.
3. High-order harmonic generation can be studied in a spectral range previously not accessible. This may be important for the understanding of the process in particular if inner shell electrons are involved. Furthermore, high-order harmonic generation in the VUV may open a new route for light sources at even shorter wavelengths.

Magnetic Characterization of the Undulator for the VUV-FEL at the TESLA Test Facility

J. Pflüger, P. Gippner[+], A.Swiderski, T. Vielitz,

Hamburger Synchrotronstrahlungslabor HASYLAB at Deutsches Elektronen-Synchrotron DESY
Notkestr 85, 22603 Hamburg, Germany
+ Forschungszentrum Rossendorf e.V. Postfach 510119, 01314 Dresden, German
Corresponding Author :J. Pflüger, DESY-HASYLAB, Notkestr 85, 22603 Hamburg, Germany

Abstract
The 15m long undulator for the VUV-FEL at the TESLA Test Facility combines the generation of the undulator- and the strong focusing quadrupole field. It consists of three individual segments which have been completed and are being installed in the TESLA Test LINAC. In this contribution we report about the magnetic characterization and fine tuning of the three undulator segments. Special emphasis is given to magnetic measurement techniques which were used to verify the small magnetic tolerances.
Keywords : Free electron Lasers, Linacs / 41.60, 29.17

1. Introduction

At DESY in Hamburg the undulator for the VUV-FEL at the TESLA Test Facility (TTF) is now installed. It is a planar fixed gap permanent magnet device based on NdFeB. material. combining two functions, the generation of the undulator field with that of a superimposed strong focusing quadrupole field. Table 1 gives an overview over its key parameters. Various aspect of this structure has already been described in a number of publications/1-5/. Here we focus on very recent results of magnetic measurements.

Table 1 : Undulator parameters

Period length	mm	27.3
Gap	mm	12
Peak Field	T	0.468
K – Parameter		1.17
Number of poles		327
Segment length with ends	mm	4492.3
Total number of segments		3
Total number of FODO quads		30
FODO cell length	mm	955.5
Quad length	mm	163.8
Integrated gradient	T	1.735
Field gradient	T/m	10.6
Segment interspacing	mm	325.0

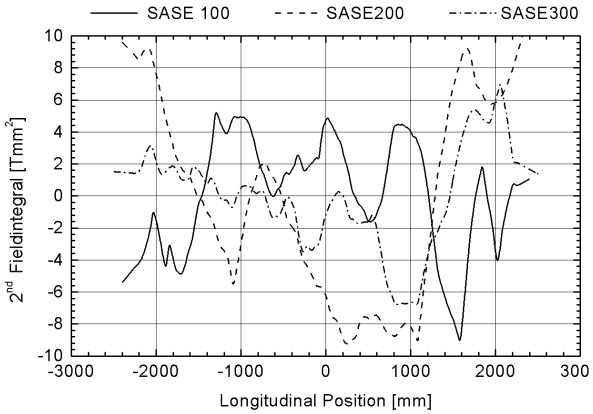

Fig. 1 Horizontal Field integrals

2. Magnetic measurements

The characterization and measurement of the undulator segments was done in three steps. The first two included the 'naked' undulator, this means that the magnet arrays which provide the focusing are not yet attached. The horizontal field was measured using a special coil with 3633 turns a winding area of $0.2625m^2$ and a cross section of about $6.2 * 12mm^2$. The coil was properly aligned in the central plane perpendicular to the main B_y field. of the undulator Alignment could be checked by minimizing the RMS signal induced in this coil

when it is moved through the undulator. as a function of the tilt angle of the coil. A Huber goniometer head, allowed for precise tilt and position control. The flux induced in the coil was measured using an analog integrator (fluxmeter) and was recorded in equidistant intervals along the undulator axis. With this technique errors in the horizontal field could be detected, which then were corrected using appropriate shims. Fig 1 shows the horizontal 2nd field integrals of the three undulator segments labeled SASE100 ,200 and 300 along the undulator axis. The RMS values for the SASE 100,200 and 300 segment are 3.5, 6.3 and 3.1 Tmm^2 ,respectively. Using the relation:

$$Z[\mu m] = \frac{300}{E[MeV)} \cdot I_2[Tmm^2]$$

one can directly calculate the orbit deviation. Typically about 12 –14 shims were needed to

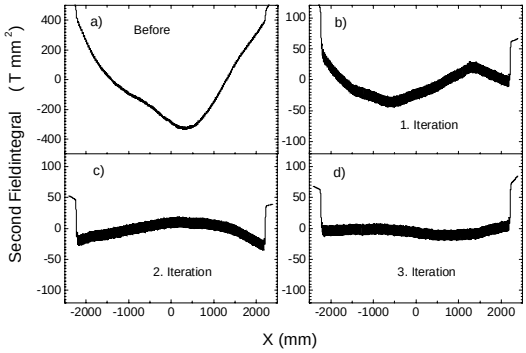

Fig 2 Trajectory optimization of the SASE100 segment.. a) Initial status, note the different scale b)-d) correspond to three optimization steps.

obtain results like those shown in Fig. 1 This is a strong indication that sorting of the magnets prior to assembly as well as the magnet material was already quite good /6/. The shims can therefore be considered as a minor correction only. The B_y field of the undulator was optimized using the method of "field fine tuning by pole height adjustment" which is described in ref. /3/. Each pole is height adjustable by about ± 0.5 mm to allow for this method. The target for this optimization is a perfectly straight trajectory. Fig 2 shows this optimization for the SASE100 segment, see also ref. /5/. for more details. It is seen that the optimization converges rapidly. The final RMS value inside the undulator shown in Fig 2 d) is 6.5Tmm^2.out of which 6,25 Tmm^2 are due to the orbit oscillation using as can be calculated using

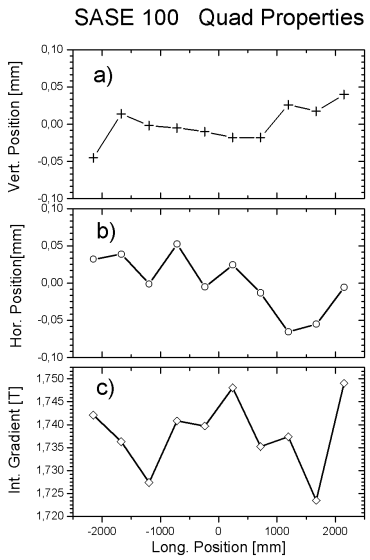

Fig 3 a),vertical b) horizontal center position c) integrated gradient of the FODO quads of the SASE100 segment

$$I2_{RMS} = \frac{1}{\sqrt{2}} \cdot \left(\frac{\lambda_u}{2\pi}\right)^2 \cdot B_{Max}.$$

Here B_{Max} is the peak field and λ_U is the undulator period length. Values are taken from Table 1 Fig 3 finally shows the final result of the adjustment of the quadrupole sections. /7/. The Rectangular coil method was used to tune each FODO quadrupoles individually/4/. It is seen that the horizontal and vertical center positions are aligned better than 50 μm. The integrated gradient deviates less than 1.2 % maximum. These deviations are small and can be handled by the beam based alignment method/8/ which will be used to control the orbit in the undulator. .

References

1. Y. M. Nikitina, J. Pflüger, Nucl. Instr. and Methods A375 (1996), 325
2. J. Pflüger, Y. M. Nikitina, Nucl. Instr. and Methods A381 (1996), 554
3. J. Pflüger, H. Lu, T. Teichmann, Proceedings of the FEL 98 Conference, Aug 16-22, 1998, Williamsburg, VA, USA
4. J. Pflüger, H.Lu, D. Köster, T. Teichmann, Nucl. Instr. and Methods A407 (1998), 386
5. J. Pflüger, Proceedings of the PAC-99 conference 29.3 – 2.4.1999 New York City, New York, USA
6. B. Faatz, J. Pflüger TESLA-FEL 99-01
7. J. Pflüger, these proceedings
8. P. Castro Proceedings of the EPAC98, June 1998, Stockholm, Sweden

Undulators for SASE FEL's

J. Pflüger

Hamburger Synchrotronstrahlungslabor HASYLAB At Deutsches Elektronen-Synchrotron
DESY Notkestr. 85, 22603 Hamburg, Germany

Abstract

In this contribution the requirements on undulators for Linac driven SASE FEL's will be discussed. Differences between long and short wavelength SASE FEL's will be worked out. The problematic influencing the choice of minimum gap and undulator peak field which are special for SASE FEL's driven by multi GeV electron beams with sub picosecond pulses, peak currents of several Kiloamperes will be pointed out. Special attention is given to the magnetic design of combined strong focusing undulators as are needed for VUV FEL's. As an example results will be presented of the undulator for the VUV-FEL at the TESLA Test Facilty which has just been completed.

Keywords Free electron lasers, Linac / 41.60, 29.17

1. Introduction

Linac driven SASE FELs are the most promising candidates for the next, the 4th generation of light sources /1-3/. They offer unique time structure of sub picosecond pulses and a gain in peak brilliance of 6-10 orders in magnitude as compared to existing 3rd generation synchrotron radiation sources.. Presently several SASE projects are underway worldwide and are about to become operational in the IR and VUV spectral region /4-6/. SASE FEL's for the hard X-ray regime down to radiative wavelengths of 0.1 nm have been proposed /7,8/. An overview of these projects is given in Table 1. One key component of central importance for any FEL is the undulator. Its length varies from about 5m for an IR source like VISA /6/ to about 100m in the case of a X-ray FEL /7,8/, see table 1.. In this contribution some considerations for the design of undulators are made. As examples recent results obtained on the undulator for the VUV-FEL, which is described in detail in /9-12/ will be presented.

2. Undulator design considerations

2.1 Undulator parameters

The radiative wavelength of an FEL is given by the basic relation

$$\lambda_R = \frac{\lambda_u \cdot \left(1 + 0.5K^2\right)}{2\gamma^2} \quad ; \quad K = \frac{e \cdot B_{Max} \cdot \lambda_u}{2\pi \cdot m_e \cdot c} \quad ; \quad B_{Max}[T] = a_3 \cdot \exp - \left\{ \frac{g}{\lambda_u} \cdot (a_1 - a_2 \cdot \frac{g}{\lambda_u}) \right\} \qquad (1)$$

With the help of these equations the undulator period length λ_u and the gap g for a given K parameter at a desired radiation wavelength λ_R and a given electron energy can be determined. Here e is the electron's charge, m_e its mass, γ its kinetic energy in units of its rest mass, and c the speed of light. The peak field B_{Max} is usually described by the empirical constants a_1 - a_3 . For a state of the art NdFeB made hybrid undulator a_1 = 5.08 ; a_2 = 1.54 ; a_3 =3.44 . It is valid for .07 < g/λ_u < 0.7.

The choice of the optimum K value for an FEL is not straight forward. Analytical formulae as given in /13/ may be used for first estimates .FEL simulation codes such as TDA3D /14/ may be used for the fine design. These simulations have to take into account realistic key parameters of the Linac such as the normalized emittance, bunch length, peak current as well as the β-function and its variation inside the undulator. The saturation length and therefore the total undulator length can then be calculated. Table 1 shows the parameters for different SASE projects ranging from the IR via the XUV to the X-ray range. The optimization for the FEL at the TTF is described in detail in /15 /. There are however other factors which influence design considerations and put additional constraints to parameters:

Resistive wall wake field effects as well as wake field effects due to surface roughness and changes in the chamber profile play an important role in Linacs with ultra short bunches and peak currents of typically several thousand amperes /16-18/. They result in a coherent energy spread over each bunch. The strength depends on the

size and design of the vacuum chamber and on the resistivity of the chamber material as well as on the surface roughness of the vacuum chamber in the undulator. These effects have been considered in the chamber design for the VUV-FEL at the TTF /19/. The surface roughness of the chamber material plays an important role and gives a big contribution to the total wake field budget /16 /. Its magnitude depends on the proper assumption of the microscopic surface structure, which may reduce or increase this effect significantly /17/. Therefore at the TTF an experiment is planned to get more quantitative information /18/

Another problem is potential radiation damage of permanent magnet material due to electron bombardment. Not much experience exists how undulators behave in the radiative environment of a high duty cycle Linac such as the TTF . Extensive experience exists only for storage rings where a high transmission through the undulator and therefore a very low loss rate is enforced by the requirement of long lifetime of the stored beam. Under normal operating conditions no significant radiation damage has been observed. In a Linac the situation is different. Although the emittance and beam sizes are smaller there might be a significant amount of beam halo and dark current. Two lines of defense have therefore been set up at the TTF: First, loss monitors will be used after each undulator segment monitoring the showers of bremsstrahlungs radiation if a beam loss occurs. Second, a well designed collimator system in front of the undulator /20/ together with a conservatively large inner vacuum chamber diameter of 9.5mm and a 12mm undulator gap will provide a passive protection.

The spontaneous emission of light in an undulators is a statistical process which induces an uncorrelated energy spread into the electron beam.. The rate of energy diffusion as given in /21/:an be calculated using :

$$\left\langle \frac{d(\Delta\gamma^2)}{dz} \right\rangle = \frac{14}{15} r_e \cdot \lambda\!\!\!^{-}_c \cdot \gamma^4 \cdot K_U^3 \cdot K^2 \cdot F(K) \quad ; \qquad K_U = \frac{2\pi}{\lambda_U} \tag{2}$$

Here r_e is the classical electron radius and $\lambda\!\!\!^{-}_c$ the Compton wavelength. For K >1 the function F(K) can be approximated by F(K)= 1.42K. /21/. FEL operation is affected if $\Delta\gamma/\gamma$ becomes comparable with the Pierce parameter ρ. It has been shown that this effect puts an ultimate limit to the achievable minimum wavelength in an X-ray FEL /13/. In Table 1 the uncorrelated energy spreads is listed. It plays a significant role only for X-ray FELs

As a consequences for undulator design: Wake field effects as well as radiation damage impose a lower limit on the vacuum chamber aperture and therefore on the undulator gap quite independent of the beam energy, while quantum fluctuations impose an upper limit on the peak field at a given beam energy but are important only for multi GeV electron beam energies, which are required for an X-ray FELs

2.2 Focusing

The saturation length of any SASE FEL is much larger than the optimum β function. Therefore additional strong focusing is required in order to keep the β function close to this optimum value. Because of its simplicity most commonly a sequences of focusing and defocusing quadrupoles a so called FODO lattice is used for this purpose. This principle is described in more detail ref. /22/, Also quadrupole tripletts can be used /8 /. If used in separated function devices they allow for a longer undulator segments but require longer interruptions between them. The external focusing determines the average β value and the effect of the beat onto the FEL process which also should be simulated using TDA3D as has been done in /15/. As a rough rule of thumb, the longer the radiation wavelength the shorter the optimum β function. IR and VUV-FELs with electron beam energies in the 1 GeV range are therefore good candidates for combined function undulators. In contrast X ray FEL's driven by multi GeV beams which require β values well above 10m and will use the separated function approach.

2.3 Gap versus energy tuning

The radiative wavelength of an undulator as given by eq. (1) can be changed in two ways.:

1. by changing the electron beam energy
2. by changing the K – parameter

Alternative 1 can be used wherever one undulator is served by one Linac, which is the case for all SASE projects presently under construction. For long undulators this alternative is clearly preferable. The undulator can be built with a fixed gap and can be fine tuned magnetically to a high degree of perfection.

Alternative 2 is relevant when more than one undulator is served by a single Linac. This situation will be encountered in a large X-ray FEL facility such as the TESLA FEL. Here several undulators will be served with beam in a time sharing fashion /8/. Here, fortunately due to the large optimum β-function a separated function undulator can be used which simplifies the magnetic design considerably. However tuning the gap in an long undulator and simultaneously preserving tough magnetic specifications as well as the phase relationships between individual undulator segments might be a very difficult challenge. For these reasons gap tuning in such a device will most probably be slow since active correction of electron beam properties as well as phase

monitoring is required. Unlike in a storage ring the undulators are not consecutively using the same beam. Therefore as an alternative fast switching of the beam lines and beam energy is discussed /8/. To what extend this will be possible with the required accuracy and stability is certainly a big technological challenge.
In the case of combined function undulators which are needed for VUV-FEL's gap tuning would be very problematic or even impossible since the focusing is coupled to the gap motion so that at larger gaps the focusing is reduced. No magnet designs exist in literature so far which can cope with this problem.

3. Results from the undulator for the TTF-FEL at the TESLA Test Facility

The undulator system for the VUV-FEL at the TESLA Test Facility is a fixed gap (12mm) permanent magnet device using a combined function magnet design called Four Magnet Focusing (4MFU). Key parameters are given in table 1. This device has been discussed in a number of publications /9-12, 22/. Her we restrict only to some most recent and unpublished results. Fig. 1 shows a view along the three undulator segments readily installed in the TTF tunnel. The vacuum chamber has also been mounted. It almost completely disappears inside the undulator gap, but the connection of the ten beam position monitors and the nine Four Wire Correctors together with the connections for the cooling water can be seen as well. For more details on the vacuum chamber design see ref /19/. Above the orbit plane the two guide rails for the laser interferometric precision alignment system can be seen. A commercial Hewlett-Packard HP5507 laser interferometer system with two 30m straightness optics ,one for the vertical and one for the horizontal direction is used to align the three undulator segments and the four monitor blocks with an ultimate precision better than 20μm. To do so a vertical and a horizontal reference surface is placed on either end of each undulator segment. They are connected via the guide rails. These surfaces are referenced to the magnetic axis of the undulator FODO lattice. Using these guide rails the Wollastone prism of the straightness optics can be placed from one reference surface to the next without interrupting the laser beam, which is essential for the measurement. Its accuracy over 15m distance is better than 4 μm. The alignment accuracy achieved is better than 14μm. The total alignment error of the magnetic undulator axes including all error sources of fiducialisation is estimated to be better than 30 – 40 μm.. The whole undulator system is enclosed by a climatized box which is about 17m long. It is designed to stabilize the temperature to 22 ± 0.3 °C and guarantees ultimate mechanical and magnetic stability.
Extensive magnetic measurements were carried out to characterize and tune the undulator. prior to installation The whole procedure included three steps. The first two were made on the "naked" undulator, which means that the quadrupoles were not yet attached. Only for the third and last step the quadrupoles were brought in place
For the first step the horizontal field was characterized and corrected: The measurements were made using a coil with 3633 windings, a cross section of only about 6.2 *12 mm^2 resulting in a winding area of 0.2625 m^2 . The flux induced in this coil is measured with an analog integrator (fluxmeter) and recorded as a function of the longitudinal position along the undulator axis. Averaging of multiple scans helps to reduce the influence of drift and increases reproducibility. It has been shown that a reproducibility of about 1 Tmm^2 can be obtained using 20-40 scans.
Field errors which still exist were compensated using appropriate shims made of .05 to 0.3mm thick iron foil. It took not more than about 12-14 shims distributed over the structure consisting of 327 magnet pairs. to bring the second field integral below 10 Tmm^2. This is a strong indication that good material quality together with individual block measurements and subsequent magnet sorting using simulated annealing /23/ was quite effective and that the error level before shimming was already very low. Fig.2 shows the second horizontal field integrals of the three installed undulator segments called SASE100, 200 and 300 after shimming. With a little exception in the case of SASE200 the value of 10 Tmm^2 is not exceeded. The RMS value of the 2^{nd} Field integral excursions are 3.5, 6.3 and 3.1 Tmm^2 for the SASE 100, 200 and 300 segments, respectively.
The second step included the measurement and optimization of the B_y field using the technique of field fine tuning by pole height adjustment/11/. Results on the first undulator segment are given in /22/. It proved very effective in optimizing the second field integral of the B_y field.
In the third step the FODO quadrupoles were attached and adjusted using the Rectangular Coil Method described in /12/. This method allows for the precise measurement of the strength and the horizontal and vertical center position of the quadrupoles. Fig 3 shows these results for the SASE100 segment. It is seen that the center alignment is better than 50μm and the integrated gradient varies by about 1.5% maximum.. These errors are small enough so that the beam based alignment method which is planned for the TTF /24,25/ can cope with them.. The residual center errors can be corrected using the Four Wire Correctors, and the individual quadrupole strengths are input into the algorithm.

4. Conclusion

In this paper some design considerations for Linac driven SASE FELs have been made.

- Away from basic considerations of the undulator parameters wake field effects as well as precautions to radiation damage sets lower gap limits which are quite energy independent. In addition on X-ray FELs spontaneous synchrotron emission puts an upper limit on the peak field.
- Additional external focusing is required in any case., Its proper design requires extensive simulations using FEL codes
- The requirement of gap tunability in very long undulators is a severe complication

Acknowledgement
The author wants to thank M. Dohlus, B. Faatz, M. Timm, H. Schlarb and R. Wanzenberg for many stimulating discussions.

References

1. M. Kondratenko, E.L. Saldin, Part. Accel. 10 (1980), 207
2. R. Bonifacio, C. Pellegrini, L. Narducci, Opt. Comm. 50 (1984), 373
3. Proceedings of the 10th ICFA Beam Dynamics Panel Workshop on 4th Generation Light sources Jan 22-25, 1996, Grenoble, , France
4. "A VUV Free Electron Laser at the TESLA Test Facility at DESY – Conceptual Design Report" TESLA-FEL 95-03 ,1995
5. S. V. Milton representing the LEUTL design team, Nucl. Instr. and Methods A407 (1998), 210
6. L. Bertolini, R. Carr, M. Cornacchia, E. Johnson, M. Libkind, S. Lidia, H.-D. Nuhn, C. Pellegrini, G. Rakowski, J. Rosenzweig, R. Ruhland, Proceedings of the FEL98 Conference, Aug 16-22, 1998, Williamsburg, VA, USA
7. LCLS Design Study Report, SLAC - R – 521, April, 1998
8. Conceptual Design of a 500GeV Linear Collider with Integrated X-ray Laser Facility Vol. II Editors: R. Brinkmann, G. Materlik, J. Rossbach, A. Wagner DESY 1997-048
9. Y. M. Nikitina, J. Pflüger, Nucl. Instr. and Methods A375 (1996), 325
10. J. Pflüger, Y. M. Nikitina, Nucl. Instr. and Methods A381 (1996), 554
11. J. Pflüger, H. Lu, T. Teichmann, Proceedings of the FEL 98 Conference, Aug 16-22, 1998, Williamsburg, VA, USA, to be published in Nucl. Instr. and Methods
12. J. Pflüger, H.Lu, D. Köster, T. Teichmann, Nucl. Instr. and Methods A407 (1998), 386
13. J. Rossbach, E.L. Saldin, E.A. Schneidmiller, M.V. Yurkov , Nucl. Instr. and Methods A374 (1996), 401
14. T. M. Tran, J. S. Wurtele, Compt. Phys, Commun. 54 (1989),18 : B. Faatz, S. Reiche, Proceedings of the FEL98 Conference, Aug 16-22, 1998, Williamsburg, VA, USA
15. W. Brefeld, B. Faatz, Y. Nikitina, J. Pflüger, P. Pierini, J. Roßbach, E. Saldin, E. Schneidmiller, M. Yurkov, Nucl. Instr. and Methods A393 (1997), 119
16. M. Dohlus, R. Lorenz, T. Kamps, H. Schlarb, R. Wanzenberg TESLA-FEL 98-02, 1998
17. G. Stupakov, R. E. Thomson, D. Waltz, R. Carr, Physical Review Special Topics – Accelerator and Beams 2, 060701, (1999)
18. A. Novokhatski, M. Timm, T. Weiland, H. Schlarb Proceeding of the PAC-99, 29.3-2.4.1999 New York City, New York, USA
19. U. Hahn, J. Pflüger, M. Rüter, P. K. den Hartog, M. Erdmann, E. M. Traktenberg, G. Wiemerslage, S. Xu, Proceedings of the PAC-99 conference 29.3 – 2.4.1999 New York City, New York, USA
20. H. Schlarb , Collimator design for the undulator for the VUV-FEL at the TTF TESLA-FEL to be published
21. E.L. Saldin, E.A. Schneidmiller, m.V. Yurkov , Nucl. Instr. and Methods A381 (1996), 545
22. J. Pflüger, Proceedings of the PAC-99 conference 29.3 – 2.4.1999 New York City, New York, USA
23. B. Faatz, J. Pflüger, "Sorting strategy for the TTF-FEL undulator magnets" TESLA-FEL 99-01
24. P. Castro Proceedings of the EPAC98, June 1998, Stockholm, Sweden
25. P. Castro, B. Faatz, K. Flöttmann, Nucl. Instr. and Methods A427 (1999), 12

Figure Captions:

1. View along the undulator installed in the Linac tunnel

2. The second field integral of the three undulator segments SASE100, 200 and 300 along the undulator axis The RMS values are 3.5, 6.3 and 3.1 Tmm^2 , respectively. For 300MeV beam $1Tmm^2$ corresponds to 1μm

3. Status after fine tuning of the ten FODO quadrupoles of the (SASE100) segment:
   a) Vertical center position
   b) Horizontal center position
   c) Integrated gradient

Fig 1

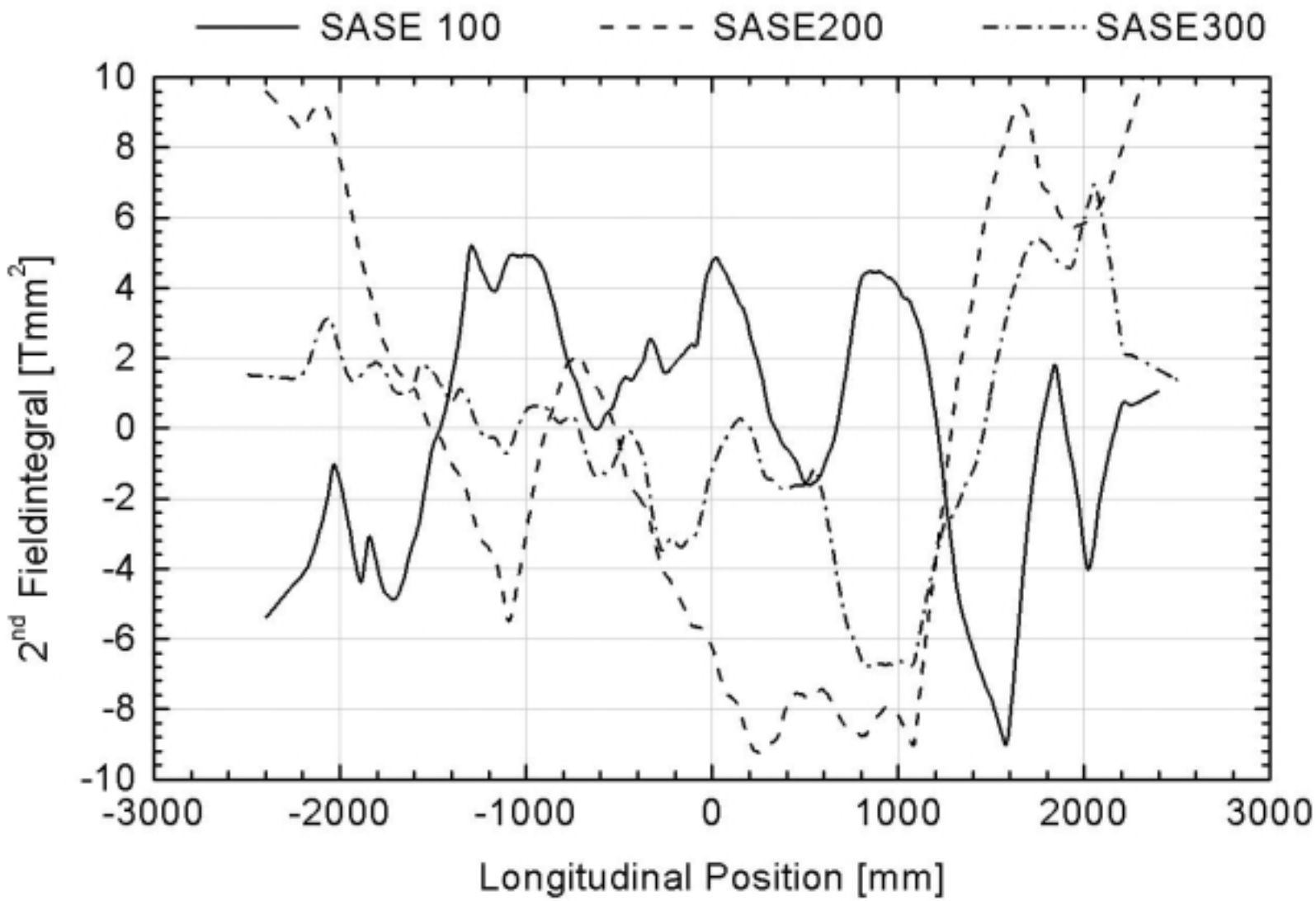
SASE 100
SASE200
SASE300
10
8
6
4
2
0
-2
-4
-6
-8
-10
-3000
-2000
-1000
0
1000
2000
3000
2nd Fieldintegral [Tmm2]
Longitudinal Position [mm]

Fig. 2

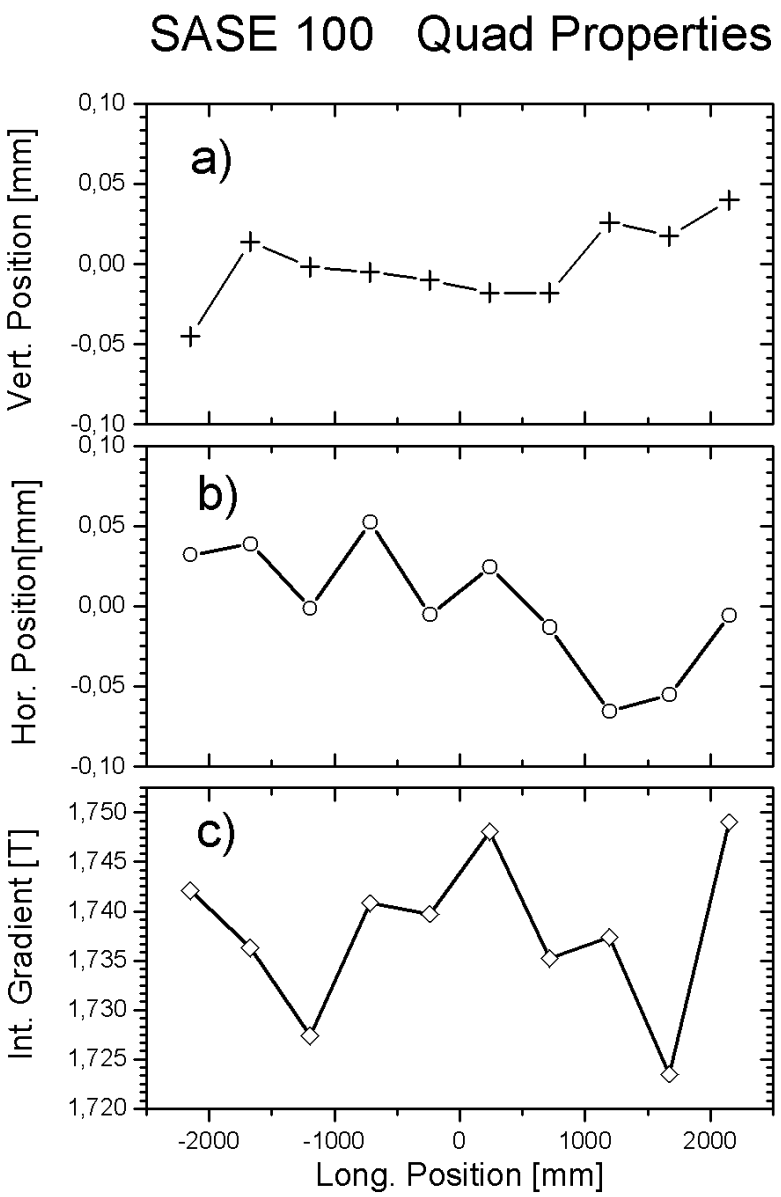
SASE 100 Quad Properties
a)
b)
c)
Vert. Position [mm]
Hor. Position[mm]
Int. Gradient [T]
Long. Position [mm]
0,10
0,05
0,00
-0,05
-0,10
1,750
1,745
1,740
1,735
1,730
1,725
1,720
-2000
-1000
0
1000
2000

Fig 3

Status August 1999		**In Construction**			**Funded**	**Proposed**	
	Units	**VISA /ATF**	**LEUTL**	**TTF I**	**TTF II**	**TESLA X-FEL**	**LCLS**
Linac Parameter							
Energy	GeV	0.071-0.085	.217	0.39	1.0		14.35
Peak current	kA	0.2	0.15	0.5	2.5	5	3.4
RMS bunch length	μm	***	800	250	50	23	33
RMS energy spread	MeV	***	0.1	0.5	1	4	3
Bunch charge	nC	1	1	1	1	1	1
Norm. Emittance	π mm mrad	2	5	2	2	1	1.5
Ext. β-function	m	0.3	1.5	1	3	15	18
Undulator							
Type		Planar	Planar	Planar	Planar	Helical	Planar
K-Parameter		1.35	3.1	1.17	1.17	5.13	3,7
Period length	mm	18	33	27.3	27.3	70	30
Peak field	T	0.75	1.0	0.46	0.46	0.79	1.32
Focusing		combined	Separated*	Combined	Combined	Separated	Separated
Total length	m	5.0	28.8	15	30	100	100
Gap / Vacuum stay clear	mm	6 / +	9.3 / ***-	12 / 9.5	12 / 9.5	12 / 9	6 / -
Induced energy spread	MeV	$< 10^{-4}$	2.7×10^{-4}	1.3×10^{-3}	2.6×10^{-3}	18.5	3.25
FEL Parameter							
Radiation wavelength	nm	600-800	532	42	6	0.1	0.15
Pierce parameter ρ		7.7×10^{-3}	$3{,}2 \times 10^{-3}$	2.76×10^{-3}	$2.1^{x} 10^{-3}$	9.4×10^{-4}	4.65×10^{-4}
Saturation length	m	3.8	14	13.8	19.2	95	94
Saturation Power	GW	.06	0.07	0.5	3.0	200	9
Peak Brilliance	**	2.2×10^{-27}	1.4×10^{28}	4.31×10^{28}	2.23×10^{30}	2.0×10^{34}	1.3×10^{33}

* using quadrupoles and natural. focusing ** Photons /s mm^2 $mrad^2$ 0.1%BW *** No information available + in vacuum undulator

Simulation of Time-Dependent Energy Modulation by Wake Fields and its Impact on Gain in the VUV Free Electron Laser of the TESLA Test Facility

S. Reiche, H. Schlarb

Deutsches Elektronen Synchrotron, Notkestraße 85, 22603 Hamburg, Germany

Abstract

For shorter bunches and narrower undulator gaps the interaction between the electrons in the bunch and the wake fields becomes so large that the FEL amplification is affected. For a typical vacuum chamber of an X-ray or VUV Free Electron Laser three major sources of wake fields exist: a resistance of the beam pipe, a change in the geometric aperture and the surface roughness of the beam pipe. The generated wake fields, which move along with the electrons, change the electron energy and momentum, depending on the electron longitudinal and transverse position. In particular the accumulated energy modulation shifts the electrons away from the resonance condition. Based on an analytic model the energy loss by the wake fields has been incorporated into the time-dependent FEL simulation code GENESIS 1.3. For the parameters of the TESLA Test Facility the influence of the bunch length, beam pipe diameter and surface roughness has been studied. The results are presented in this paper.

1. Introduction

Several Free Electron Lasers are proposed or currently under construction to extend the wavelength region to the VUV and X-Ray regime [1, 2, 3, 4]. As a natural drawback the FEL efficiency drops with higher beam energies, which is partially compensated by a larger peak current and undulator field. These FEL parameters are increased by compressing the bunch and by reducing the magnetic gab between the undulator poles. As a disadvantage the electron beam becomes more sensitive to wake fields in the accelerating and undulator section of the beam line.

During the FEL amplification the wake fields generate a modulation of the beam energy. These energy changes are accumulated over the entire undulator length and might push the electrons out of the amplification bandwidth. For an efficient performance the FEL should saturate before. Therefore constraints arise for the bunch length and vacuum chamber design and construction.

The second phase of the Free Electron Laser at the TESLA Test Facility operates with a shorter bunch length and might be affected by the wake fields. The parameters are listed in Tab. 1. Based on a model of the wake fields, described below, the time-dependent FEL simulation code GENESIS 1.3 [5] has been used to study the impact of the growing energy modulation.

2. Wake Field Model

Wake fields have various sources, caused by the explicit shape of the beam pipe. In particular a small beam pipe diameter in the undulator section generates a large wake field amplitude, which is also enhanced by the short bunch length required to achieve an efficient FEL performance. During the FEL amplification only three types of

Electron Beam	
Energy	1 GeV
Bunch Length (rms)	50 μm
Normalized Emittance	2 π mm·mrad
Undulator	
Period	2.73 cm
Undulator Parameter (rms)	0.898
Length	30 m
Beam Pipe Diameter	9.5 mm
FEL	
Radiation Wavelength	6.4 nm
FEL Parameter ρ	$2.1 \cdot 10^{-3}$
Gain Length	1.0 m

Table 1. Design Parameters of the VUV FEL (Phase II) at the TESLA Test Facility

wake fields have noticeable impact on the performance. Although wake fields might already affect the beam energy in the accelerating section of the injector they are not considered here. In addition the discussion is restricted to the fundamental longitudinal wake field. Higher modes as well as transverse wake fields imply either a difference between the center of the beam pipe and the undulator axis of an electron beam offset from the undulator axis. Concerning the second cause the FEL performance is degraded mainly by the missing overlap between electron beam and radiation field [6] and not by the resulting energy modulation and emittance growth.

The first type of wake fields is generated by the resistance of the beam pipe [7]. The mirror charge at the beam pipe surface is affected by the resistance and deforms the electric field of an electron moving along the beam pipe. The model includes only a DC conductivity of the wall. For aluminum the approximation is sufficiently accurate. The resulting change in the energy per unit length as it would be seen by a trailing sample electron is given by the wake function

$$W_z(t) = -\frac{4ce^2Z_0}{\pi R^2}\left(\frac{1}{3}e^{\frac{t}{\tau}}\cos[\sqrt{3}\frac{t}{\tau}] - \frac{\sqrt{2}}{\pi}\int_0^\infty dx \frac{x^2 e^{\frac{t}{\tau}x^2}}{x^6+8}\right) \quad , \quad (1)$$

where $t < 0$ is the longitudinal position behind the ultra relativistic electron, R is the beam pipe radius, $Z_0 \approx 377\ \Omega$ is the vacuum impedance and $\tau = [2R^2/Z_0\sigma]^{1/3}$ is the characteristic scale of the wake field. For the parameter of the TTF-FEL with $R = 4.75$ mm and a conductivity of aluminum ($\sigma = 3.65 \cdot 10^7\ \omega^{-1}\mathrm{m}^{-1}$) τ has a value of 15 μm. Ahead of the electron ($t > 0$) the wake function vanishes.

Another source of wake fields is caused by any change in the aperture of the vacuum pipe such as cavities, bellows as well as pumping slits. Based on the diffraction model [8] the wake function is defined by the effective gap length $g_{eff} = (\sum \sqrt{g_i})^2)$, where g_i is the length of the individual disturbance in the beam pipe. Integrating over a longitudinal distance L, which includes all gaps, yields the wake function of a single electron

$$W_z(t) = -\frac{ce^2Z_0}{\pi^2 RL}\sqrt{\frac{g_{eff}}{2}}\frac{1}{\sqrt{-t}} \quad (2)$$

for $t < 0$. The TTF undulator is built up of several modules with unique design including cavity BPM's, wire scanners, pumping slots and bellows. The effective gap is 15 cm per module ($L = 4.5$ m).

The last type of wake fields are wave guide modes which slowed down and thus can couple to the electron beam. The reason lies in the surface roughness of the vacuum chamber. To model these wake fields the source roughness is replaced by a dielectric layer with $\epsilon \simeq 2$ [9]. The thickness δ is set to the longitudinal rms variation of the roughness. The wake function is

$$W_z(t) = -\frac{ce^2Z_0}{\pi R^2}\cos(k_0 t) \quad , \quad (3)$$

defining the wave number $k_0 = \sqrt{4/R\delta}$. An alternative wake field model [10] predicts smaller wake field amplitudes if the characteristic length of the surface roughness becomes comparable to the electron bunch length. For this paper the more conservative model (Eq. 3) has been considered.

The convolution of all wake functions with the longitudinal bunch profile yields the wake potentials, shown in Fig. 1. The amplitude of the resulting wake potential has an absolute maximum of roughly 100 keV/m for a surface roughness of $\delta = 350$ nm, a bunch charge of 1 nC and a bunch length of 50 μm. These beam parameters correspond to Phase II of the TTF-FEL. At Phase I the five times longer bunch length causes a significantly reduced wake potential with almost no noticeable impact on the FEL performance.

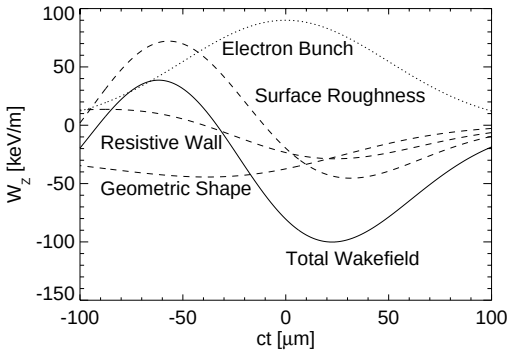

Fig. 1. Wake potential of the undulator chamber of the TESLA Test Facility, Phase I.

3. Simulation Results

The energy modulation affects the FEL process in two different ways. Either the electron energy is pushed outside the FEL amplification bandwidth or the radiation field advances to parts of the bunch where the electrons are resonant at a different wave length. Estimating the saturation length by roughly $L_s \approx 16 L_g = 8/k_U\rho$, where L_g is the gain length, k_U is the undulator wave number and ρ the FEL parameter [11], the total energy loss has to be less than the bandwidth of the FEL. This yields the constraint

$$\left|\frac{d\gamma}{dz}\right| \ll \frac{1}{4} k_U \rho^2 \gamma \qquad (4)$$

for the acceptable energy loss. For the parameters of the TTF-FEL, Phase II, this limit lies at 250 keV/m, which is of the same order as for the expected wake fields.

Similar arguments result in the limitation of the allowed energy modulation along the slippage length with

$$\left|\frac{d\gamma}{cdt}\right| \ll \frac{1}{4} k \rho^2 \gamma \quad , \qquad (5)$$

where k is the radiation wave number. Due to the dependency of k on the energy as γ^2 this condition is negligible for VUV and X-ray FEL's. Because the slippage is much smaller than the bunch length only a strong energy modulation might noticeably affect the FEL amplification. For the TTF-FEL parameters Eq. 5 sets the upper limit to an energy gradient of 1 MeV/μm along the bunch. Even for strong wake fields this gradient would be accumulated after several hundreds of meters only, much longer than the saturation length of typically 25 m. Because Eq. 5 is practically always fulfilled for VUV and X-Ray FEL's any initial energy modulation, caused by wake fields in the injector part preceding the undulator, does not interfere with the FEL amplification. The total slippage length of the radiation is short. Therefore only the local energy change during the amplification is a critical issue for the FEL (Eq. 4) but not the correlated energy spread over the entire bunch (Eq. 5).

Based on Eqs. 1 – 3 the calculated wake potential is incorporated into the time-dependent FEL code GENESIS 1.3. Using the wake potential, shown in Fig. 1, the saturation power is reduced by 20% compared to simulations excluding an energy modulation.

From all parameters, which are defining the wake potential, only three are meaningful to study: the beam pipe radius R, the surface roughness δ and the bunch length σ_t. From these three the FEL amplification is least sensitive on a change of the pipe radius. By varying the radius from 3.5 mm to 6 mm the saturation power changes about 50% while the saturation length remains the same.

The other parameters have a stronger impact on the FEL performance as it seen in Fig. 2. In the range of the considered surface roughness from a smooth surface ($\delta = 0$ nm) to an rms variation of 700 nm the saturation power drops above the threshold value of 200 nm. This defines the tolerance in the roughness, to which level the FEL process is not degraded.

For $\delta < 350$ nm the longitudinal position, where all three wake fields cancel each other, lies within one standard deviation around the location of maximum current. This part of the beam is not affected by the wake fields, providing the gain of an undisturbed FEL amplification. A larger surface roughness increases the period of the wake function (Eq. 3) and shifts the root to a slice in the electron bunch with lower beam current and less gain.

Varying the bunch length the shape of the wake potential remains unchanged but is scaled in magnitude. The dependency is almost quadratically with a maximum amplitude of about 400 keV/m

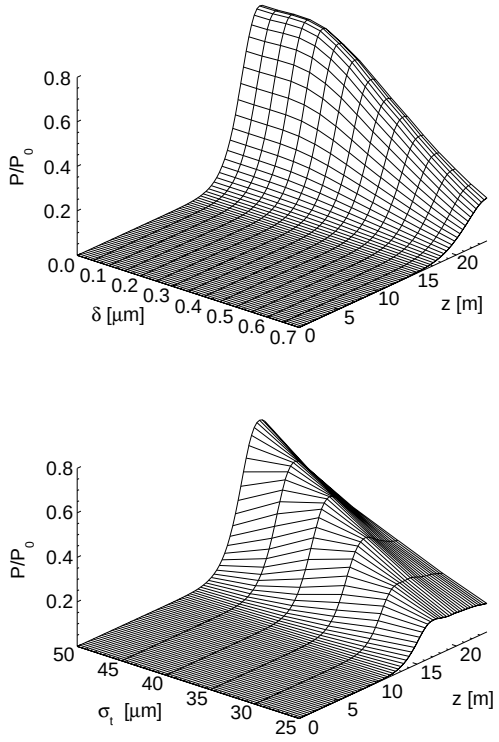

Fig. 2. FEL performance, normalized to the saturation power P_0 of the undisturbed amplification, for different values of surface roughness and bunch length (upper and lower plot, respectively).

for a bunch length of $\sigma_t = 25$ μm, the smallest value used for the simulation. Although the saturation length is shortened the typical oscillation of the radiation power beyond saturation is missing for bunch lengths below 35 μm, as it can be seen in the lower plot of Fig. 2. In these cases the amplification is rather turned off by the accumulated energy loss than by reaching saturation. With respect to the efficiency the best FEL performances is achieved for the longest bunch length.

Because most of the electrons loose energy the resonance condition of the FEL is shifted towards longer wavelengths. The SASE FEL starts from the initial fluctuation in the electron positions, which frequency bandwidth is broader than the FEL amplification bandwidth. With the changing resonance condition lower frequencies gets stronger amplified. The total amplification depends on how long the bunch stays in the amplification bandwidth (Eq. 4). The TTF-FEL parameters allow to reach saturation. A typical spectrum is shown in Fig. 3, compared to the case excluding wake fields. The shift in the spectrum is about 0.5% with an enhanced tail of lower frequencies components.

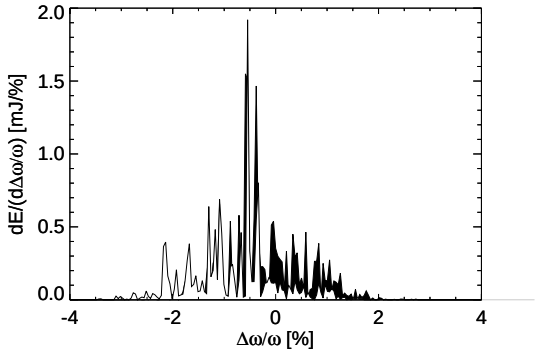

Fig. 3. Typical radiation spectrum after 18 m including wake fields. The difference to the undisturbed case is colored black.

4. Conclusion

It is shown that wake fields are an important factor for the FEL performance in the VUV and X-ray regime. The main source of reduced amplification is the accumulated change in the electron energy, shifting the resonance condition of the FEL. The variation in the energy modulation along the bunch plays a secondary role because the amplification is almost localized due to the negligible slippage length of a few microns or less. The most critical parameter, which magnitude is determined during the construction of the vacuum chamber, is the surface roughness. If the variation exceeds a few hundreds of nanometers it is the dominant part of the wake fields and the output power is easily degraded by more than one order of magnitude. Simulating the impact of the wake fields should give the tolerance level for manufacturing the vacuum chambers. For the TTF-FEL the tolerance lies at 200 nm.

References

[1] J. Rossbach *et al.*, Nucl. Inst. & Meth. **A375** (1996) 269

[2] S.V. Milton *et al.*, Nucl. Inst. & Meth. **A407** (1998) 210

[3] R. Tatchyn *et al.*, Nucl. Inst. & Meth. **A375** (1996) 274

[4] Linear Collider Conceptual Design Report, DESY print 97-48, Hamburg, DESY, 1997

[5] S. Reiche, Proc. of the FEL98-Conference, Wiliamsburg, 1998

[6] B. Faatz, J. Pflüger and P. Pierini, Nucl. Phys. & Meth. **A375** (1996) 441

[7] K. Bane, SLAC Report AP-87 (1991)

[8] A.W. Chao, Physics of Collective Beam Instabilities in High Energy Accelerators, (John Wiley and Sons, New York, 1993)

[9] A. Novokhatski, M. Timm and T. Weiland, Proc. of the PAC99 Conference, New York, 1999

[10] G.V. Stupakov, Phys. Rev. ST Accel. Beams **1**, 064401 (1998)

[11] R. Bonifacio, C. Pellegrini and L.M. Narducci, Opt. Comm. **50** (1984) 373

Compensation of FEL Gain Reduction by Emittance Effects in a Strong Focusing Lattice

S. Reiche

Deutsches Elektronen Synchrotron, Notkestraße 85, 22603 Hamburg, Germany

Abstract

The constraint of a small transverse emittance becomes more severe the higher the electron beam energy in an FEL. To compensate the transverse and thus the longitudinal velocity spread, a compensation scheme has been proposed previously by Derbenev and Sessler et al for Free Electron Lasers by introducing a correlation between the energy and the average betatron amplitude of each electron. This compensation scheme is based on a constant absolute value of the transverse velocity, a feature of the natural focusing of undulators, and does not include strong focusing of a superimposed quadrupole lattice. This paper focuses on the electron motion in a strong focusing lattice with a variation in the axial velocity. The resulting reduction of the compensation efficiency is analyzed using simulations. It is seen that the compensation scheme is not much affected if the lattice cell length is shorter than the gain length. For the results presented in this paper, the parameters of the proposed TESLA X-ray FEL have been used.

1. Introduction

Several Free Electron Lasers are proposed or currently under construction [1, 2, 3, 4] to extend the wavelength range to the VUV and X-ray regime. Compared to FEL's operating at a shorter wavelength, an efficient FEL performance demands an improved beam quality to keep the total length of the FEL in reasonable limits. In particular the spread in the transverse motion degrades the synchronization of the electrons with the radiation field because the longitudinal velocity is modulated by the betatron oscillation. The FEL amplification is affected by the transverse emittance similar to a larger energy spread, resulting in an increased saturation length with reduced radiation power. This emittance effect is enlarged if the focusing strength of a quadrupole lattice is increased. The optimum focusing provides a beam size, where the enhancement of the FEL amplification by a higher electron density and the degradation by emittance effects are in balance for the FEL gain [5].

The impact of the transverse motion can be reduced if the slower longitudinal velocity for a larger betatron amplitude is compensated by a higher electron energy. This implies a correlation between the average transverse position of the electron and its energy [6, 7]. If the change in the longitudinal velocity is constant the compensation scheme will be highly efficient as it is the case for the natural focusing of the undulator with no externally applied strong focusing [8].

The natural focusing is not sufficient enough for X-ray FEL's with electron beam energies above 10 GeV. A quadrupole lattice increases the electron density to shorten the gain length. Typically the period length of the betatron oscillation and thus the modulation of the longitudinal velocity is larger than the gain length. A conditioned beam, where the correlation between energy and betatron amplitude has been applied, can only compensate the average change in the longitudinal velocity, reducing the efficiency of the compensation

scheme for a strong focusing lattice.

For the following discussion of the compensation scheme for a strong focusing quadrupole lattice the design parameters of the TESLA X-ray FEL have been used as listed in Tab. 1. The undulator is built up by an alternating sequence of 0.4 m long quadrupoles and 2.0 m long undulator modules. It is one of the three optional designs for the undulator.

Electron Beam	
Energy	25 GeV
Peak Current	5000 A
Normalized Emittance	1 π mm·mrad
Undulator	
Period	7 cm
Undulator Parameter (rms)	3.93
Length	100 m
Quadrupole Gradient	35 T/m
FEL	
Radiation Wavelength	2.5 Å
FEL Parameter ρ	$9.4{\cdot}10^{-4}$
Gain Length	5.9 m

Table 1. Design Parameters of the TESLA X-Ray FEL

2. Electron Motion

The motion within the undulator is split into the fast oscillation, driving the FEL amplification, and the betatron oscillation. For a highly relativistic electron the longitudinal velocity is

$$v_z = c\left[1 - \frac{1+K^2}{2\gamma^2} - \frac{p_x^2+p_y^2}{2(\gamma mc)^2}\right] \quad , \qquad (1)$$

where γ is the beam energy normalized to the electron rest mass mc^2, K is the dimensionless rms undulator field and $p_{x,y}$ are the transverse canonical momenta. For natural undulator focusing the last term of Eq. 1 adds up with the transverse dependency of the undulator field $K(x,y) = K_0(1+k_x^2x^2/2+k_y^2y^2/2)$ to a constant term when averaged over one undulator period λ_U, where $K_0 = eB/mck_U$ is the field at the undulator axis. The explicit values of k_x and k_y are defined by the curvature of the magnet pole faces, fulfilling the constraint $k_x^2 + k_y^2 = k_U^2$ with $k_U = 2\pi/\lambda_U$. This constant reduction of the longitudinal velocity makes the compensation by a larger energy for large betatron amplitudes highly efficient. For a strong focusing lattice the longitudinal velocity is not constant anymore. The variation in p_x and p_y can only be compensated in average by a conditioned beam.

The spread in v_z due to the transverse emittance has to be smaller than the acceptance of the FEL amplification resulting in the constraint

$$\epsilon_N \ll \frac{4\rho\beta\gamma\lambda}{\lambda_U} \quad , \qquad (2)$$

where ϵ_N is the normalized emittance, ρ is the FEL parameter [9], β the beta function and λ the radiation wavelength of the FEL. The right hand side of Eq. 2 drops approximately as γ^{-1} for higher beam energies. The constraint for a small emittance is more severe for an X-ray FEL than for an FEL, which radiates in the visible or IR regime.

To estimate the trajectory of the electrons in a strong focusing lattice and thus the impact of p_x^2 and p_y^2 in Eq. 1 the TESLA undulator quadrupoles are described in the thin lens approximation.

The electron motion in the x-direction for the drift section behind a focusing quadrupole of the periodic FODO lattice is given by

$$x(z) = \sqrt{I_x\beta(z)}\,\sin(\Psi(z)+\phi_0) \qquad (3)$$

with

$$\beta(z) = \beta_0 - 2\alpha_0 z + \gamma_0 z^2 \qquad (4)$$

and

$$\Psi(z) = \arctan(\gamma_0 z - \alpha_0) + \arctan(\alpha_0) \quad , \qquad (5)$$

where α, β and γ are the optical functions, ϕ_0 the initial betatron phase, I_x the Courant-Snyder constant of the betatron motion [11]. The index 'O' refers to the values of the optical functions right at the beginning of the drift with the length L. The solution for the second drift after the defocusing quadrupole is obtained by replacing z with $L - z$ in Eqs. 3 and 4 and by adding the phase advance $\Psi(L)$ to ϕ_0.

The divergence $x' = p_x/p_z$ is independent on z for the drift section with

$$x'(z) = \sqrt{\frac{I_x}{\beta_0}}\,[\cos(\phi_0) - \alpha_0\sin(\phi_0)] \qquad (6)$$

for $z < L$ and

$$x'(z) = \sqrt{\frac{I_x}{\beta_0}}\left[\left(1+\frac{2\alpha_1 L}{\beta_1}\right)\cos(\phi_0) + \left(1-\frac{2L}{\alpha_1\beta_1}\right)\alpha_0\sin(\phi_0)\right] \quad (7)$$

for $L < z < 2L$ with $\beta_1 = \beta(L)$ and $\alpha_1 = \alpha_0 - \gamma_0 L$.

These general results can be simplified if the FODO cell length is small compared to the average value of the beta function $\bar{\beta} = (\beta_0 + \beta_1)/2$ (L=2.4 m, $\bar{\beta} \approx 18$ m for the TESLA FEL)

The values of α_0 and α_1 tend to be unity with

$$\alpha_{0,1} \approx 1 \pm \frac{L^2}{2\bar{\beta}^2} \quad . \quad (8)$$

The upper and lower sign denotes the value of α_0 and α_1, respectively. The transverse divergence consists out of two terms of equal strength, where the sine term with an alternating sign over one FODO cell length modifies the electron motion to a 'sawtooth'-like trajectory at maximum displacement of the electron from the undulator axis (Fig. 1).

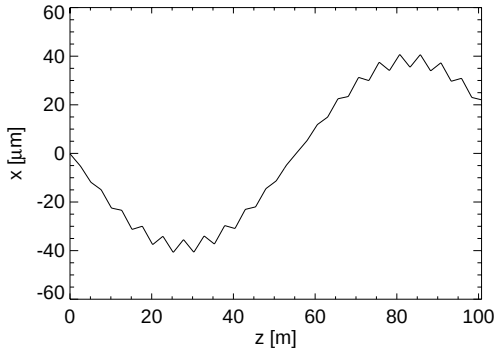

Fig. 1. Trajectory of a sample electron within the undulator of the TESLA X-ray FEL.

With a value of α close to unity and a short FODO cell length the longitudinal velocity exhibits a dominant fluctuation of p_x^2 in Eq. 1 on the scale of $2L$, which is shorter than the gain length. For the FEL process this term can be regarded as constant by averaging over one FODO cell length. The long term variation with the periodicity of the betatron oscillation is strongly inhibited with a remaining amplitude of a few percents compared to the constant term. Therefore the compensation scheme becomes efficient for this kind of quadrupole lattice. The applied correlation between energy and the betatron amplitude is given by

$$\Delta\gamma = \frac{\lambda_U \gamma}{4\lambda\bar{\beta}}(I_x + I_y) \quad . \quad (9)$$

For a typical quadrupole lattice of an X-ray FEL the impact of the natural undulator focusing is negligible and the correlation strength is the same for both planes.

3. Simulation Results

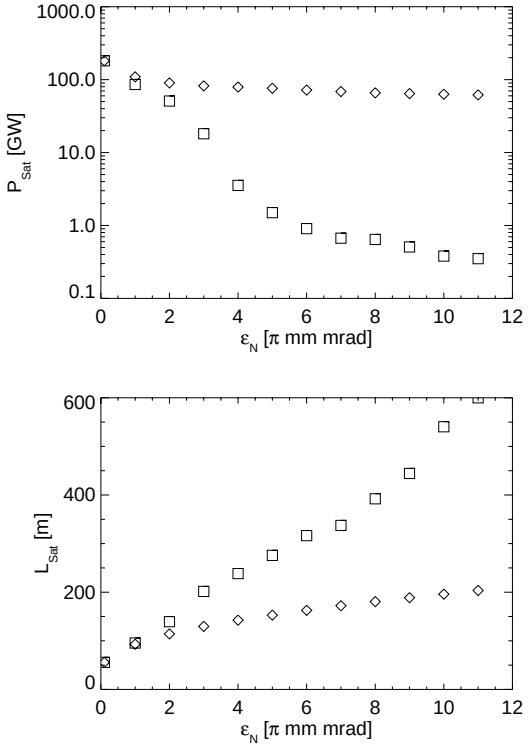

Fig. 2. Saturation power and length (left and right, respectively) for different normalized emittances for a conditioned and unconditioned electron beam (◇- and □-marker, respectively).

The 3D FEL code GENESIS 1.3 [12] has been used to study the efficiency of the compensation scheme for the strong focusing lattice of

the TESLA X-ray FEL. The results for different values of the normalized emittance are shown in Fig. 2. For the largest emittance of $\epsilon_N = 11\ \pi$ mm·mrad and an unconditioned beam the degradation of the saturation power would be two orders of magnitude while the saturation length is increased by a factor of six. The case of a conditioned beam yields a significantly improved output although the results are still worse than those for the design value of $\epsilon_N = 1\ \pi$ mm·mrad. This is explained by the fact that a larger emittance increases the electron beam spot size and thus degrades the efficiency of the FEL. Compared to simulations where the focusing strength has been reduced to obtain the same spot size also with the design value of the emittance the differences in saturation power and length are less than 10%. This indicates that the compensation scheme is highly efficient.

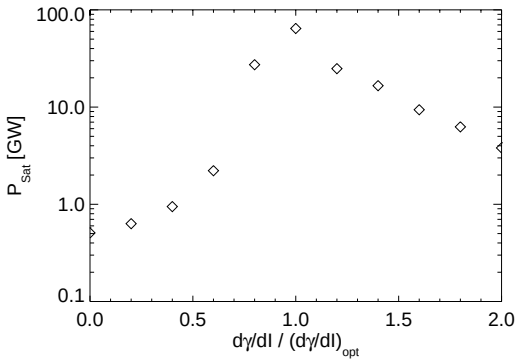

Fig. 3. Saturation power for a conditioned electron beam with different strengths of correlation.

In order to find the highest efficiency the correlation strength has been varied. The results are presented in Fig. 3. The best performance is achieved for the correlation strength according to Eq. 9. Any different value would reduce the output power as well as increase the saturation length. The results are asymmetric in the correlation strength where an overconditioned beam provides a better performance than an underconditioned one. This fact is explained by the distribution in the longitudinal phase space. An overconditioned beam corresponds to an equivalent energy distribution with a tail towards higher energies. The core process of the FEL amplification can be regarded as a rotation of the distribution in the longitudinal phase space. The tail is shifted to lower energies by transferring energy to the radiation field. This supports the FEL process in contrast to the underconditioned case, where the tail extracts energy from the radiation field and thus weakens the FEL amplification.

4. Conclusion

Due to the properties of a strong focusing lattice with a FODO cell length several times shorter than the average beta function, the variation of the longitudinal velocity has a characteristic scale shorter than the gain length and can be regarded as constant for the FEL amplification. This makes it suitable for applying a correlation between the betatron amplitude of the electron and its energy to compensate the reduction in the synchronization of the electrons with the radiation field. It relaxes the constraint of a small transverse emittance. This is particularly for beam energies driving an X-Ray FEL.

5. Acknowledgment

The author would like to thank Y. Derbenev, P.N. Lebedev and J. Rossbach for their useful discussions.

References

[1] J. Rossbach *et al.*, Nucl. Inst. & Meth. **A375** (1996) 269

[2] R. Tatchyn *et al.*, Nucl. Inst. & Meth. **A375** (1996) 274

[3] Linear Collider Conceptual Design Report, DESY print 97-48, Hamburg, DESY, 1997

[4] S.V. Milton *et al.*, Nucl. Inst. & Meth. **A407** (1998) 210

[5] J. Rossbach *et al.*, DESY print TESLA-FEL 95-06, Hamburg, DESY, 1995

[6] Y. Derbenev, "RF Compensation of Aberrational Velocity Spread of Electrons in FEL", reported at: Light Source Dept. Seminar, BNL, 1990

[7] A.N. Sessler, D.H. Whittum and L.H. Yu, Phys. Rev. Lett. **68** (1992) 309

[8] E.T. Scharlemann, J. Appl. Phys. **58** (1985) 2154

[9] R. Bonifacio, C. Pellegrini and L.M. Narducci, Opt. Comm. **50** (1984) 373

[10] D.A. Edwards and M.J. Syphers, An Introduction to the Physics of High Energy Accelerators, (John Wiley and Sons, New York, 1993)

[11] E.D. Courant and H.S. Snyder, Ann. Phys. **3** (1958) 1

[12] S. Reiche, Proc. of the FEL98-Conference, Wiliamsburg, 1998

A Method for Measuring the FEL Radiation Power Along an Undulator

S. Reiche

Deutsches Elektronen Synchrotron, Notkestraße 85, 22603 Hamburg, Germany

Abstract

A highly desirable measurement in Free Electron Laser experiments is the dependency of the radiation power along the undulator. Most designs of undulators prohibit detection of the radiation power within the undulator or extracting the electron beam at arbitrary positions. Transport of both, the radiation field and the electron beam, through the entire undulator, and thus an ongoing FEL interaction, is unavoidable. If there are many correction magnets distributed along the beam pipe, one can think of exciting a large orbit distortion downstream from any of these correctors. For a gain length comparable to or larger than the beta function this excitation of a coherent betatron oscillation might degrade the FEL amplification to a level, for which the radiation power does not further grow over the remaining length of the undulator. This paper presents the efficiency of this method for the parameters of the VUV Free Electron Laser at the TESLA Test Facility.

1. Introduction

The ability of beam diagnostics within the undulator is limited due to the small undulator gap and the vacuum chamber design. In particular no information can be obtained about the radiation power growth along the undulator except for the radiation power at the end of the device. Theoretically the FEL amplification can be stopped by extracting the beam transversely from the undulator but for most Free Electron Lasers, such as the VUV FEL at the TESLA Test Facility [1], the design of the undulator and vacuum chamber denies this. The beam has to be transported to the end of the undulator through the beam pipe. Over the transport distance the already modulated electron beam radiates at the resonant wavelength although a further amplification is reduced if the beam is separated from the radiation field. This radiation is added up to the formerly undisturbed FEL radiation.

The main principle of extracting the information about the radiation power growth is to separate the electron beam from the radiation field and to keep the further interaction to a minimum level. The separation is initialized by exciting a coherent oscillation. For this purpose steering magnets are used. Typically several of them are distributed along the undulator for a VUV or X-ray Laser [1, 2, 3, 4].

For a high gain FEL [5, 6] the radiation power grows exponentially along the distance of the undulator. The question whether the output power of an FEL with excited betatron oscillation can be used to measure the power growth is investigated by means of simulation with the code Genesis 1.3 [7]. The simulation are based on the Free Electron Laser at the TESLA Test Facility, whose parameters are listed in Tab. 1.

2. Transverse Motion of the Electron Beam

The goal for a high efficient Free Electron Laser performance is the synchronization between the

Electron Beam	
Energy	230 – 390 GeV
Bunch Length (rms)	250 μm
Normalized Emittance	2 π mm·mrad
Undulator	
Period	2.73 cm
Undulator Parameter (rms)	0.898
Length	15 m
FEL	
Radiation Wavelength	120 – 40 nm
FEL Parameter ρ	$(4.6\ –2.8)\cdot 10^{-3}$
Gain Length	0.9 – 1.6 m

Table 1. Design Parameters of the VUV FEL (Phase I) at the TESLA Test Facility

electron beam and the radiation field. Any coherent transverse motion of the electron beam would disturb this synchronization and degrade the FEL amplification [8, 9]. Beside the missing overlap between the radiation field and the electron bunch the transverse motion affects the longitudinal velocity and thus the electrons change their ponderomotive phase relatively to the radiation field. These two sources of degradation – often referred to as beam wander and phase shake [10] – have different impact depending on the focusing properties of the undulator and the resonant wavelength.

The transverse beam offset depends linearly on the average transverse velocity while the longitudinal motion, expressed by the ponderomotive phase θ, is influenced by a square dependency according to

$$\frac{d\theta}{dz} = k_U - k\frac{1+K^2}{2\gamma^2} - k\frac{v_x^2+v_y^2}{2c^2} \quad , \qquad (1)$$

where z is the position within the undulator, k_U is the undulator wave number, k the radiation wave number, K is the dimensionless rms undulator parameter, γ the electron energy normalized to the electron rest mass and $v_{x,y}$ are the transverse velocities in the x- and y-direction, respectively.

For an excited betatron oscillation the amplitude in the transverse position and velocity are closely related to each other. Therefore a small amplitude degrades the FEL performance mainly by the missing transverse overlap before the phase shake becomes dominant for larger amplitudes. The degradation of the FEL radiation power close before reaching saturation is shown in Fig. 1, for electron beam injected with various offsets into the undulator of the TTF-FEL. In good approximation the dependency is Gaussian. The phase shake plays no significant role for beam wanders comparable to the beam size of about 80 μm [11].

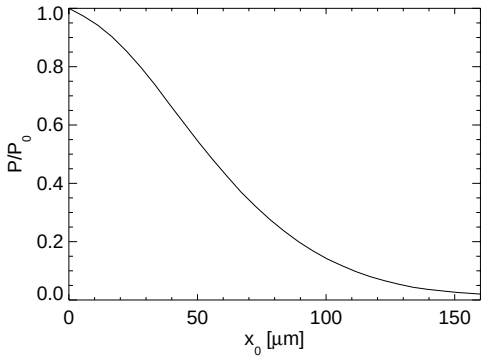

Fig. 1. Reduction of the FEL output power close to saturation of the TESLA Test Facility FEL for various initial beam offsets.

With respect to the electron ponderomotive phase any transverse motion will retard the electrons and the FEL resonance condition is shifted towards longer wavelengths. This change in the resonant wavelength can only compensate the average retardation but not the fluctuation of v_x and v_y in Eq. 1 due to the betatron oscillation. Despite this fact the difference in the resonant wavelength for an electron beam, aligned to the undulator axis, and a beam oscillating coherently with a large betatron amplitude, might be sufficiently large to inhibit the further amplification at the initial resonant wavelength after the excitation of the betatron oscillation.

3. Excitation of Large Betatron Amplitudes

Exciting large betatron amplitudes should be a sufficient method to prevent any further amplification beyond the steering magnet position. The measured output power of the FEL would correspond to the radiation power at the position of excitation. How far the remaining interaction between electrons and radiation field distorts this simple relation is studied by numerical simulations.

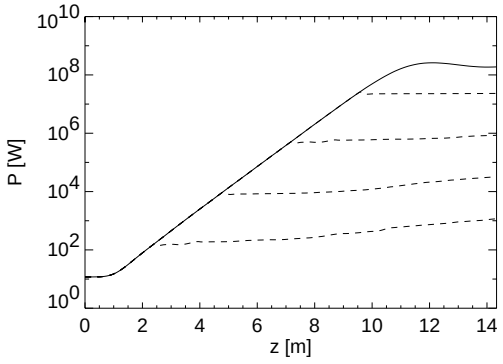

Fig. 2. Evolution of the TTF-FEL radiation power for various positions after a betatron oscillation with an amplitude of 1 mm has been excited.

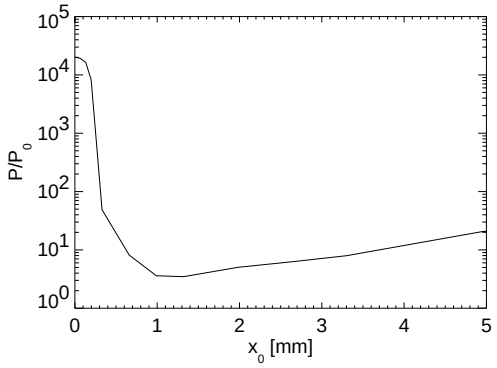

Fig. 3. Output power of the TTF FEL for different excited betatron amplitudes. The radiation power has been normalized to the power at the steering position $z = 5$ m.

In Fig. 2 the radiation power along the undulator is shown for different positions of the exciting steering magnets. An excited betatron amplitude of 1 mm provides the best performances, where the amplification is strongly inhibited and the radiation power is almost conserved to the end of the undulator. If the amplitude is larger than 1 mm the output power of the FEL grows again as it will be discussed below. For an electron beam, steered in an early stage of the amplification, a further growth of the radiation power is unavoidable. The preceding FEL interaction has already modulated the electron beam in the energy as well as in the longitudinal density ('micro bunching'). While the introduced bunching radiates coherently at the resonant wavelength the energy modulation yields an even further growth of the micro bunching.

Exceeding betatron amplitudes of 1 mm the efficiency of the presented method to measure the radiation power along the undulator is not improved as it can be seen in Fig. 3. A steering position of $z = 5$ m has been used for these simulations. The smallest value of the FEL output power occurs for a 1.2 mm offset. The radiation power grows by a factor of 3.5 over the remaining undulator length after the steering position. For earlier positions the factor is even enlarged. Compared to the suppressed growth of the FEL amplification of 2×10^4 over this distance this slight increase of the measured radiation power is acceptable.

The drop in the radiation power for betatron amplitudes smaller than 0.5 mm exhibits a dependency on the amplitude as $\exp[-ax_0^4]$. This agrees with the model when the phase shake is dominant [12]. The strength of this dependency is even enhanced because the wavelength has not been adjusted to the shift in the resonant condition.

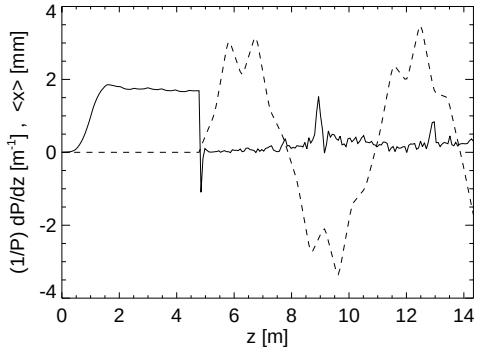

Fig. 4. Betatron oscillation of the electron bunch and exponential increment of the radiation field along the undulator (dashed and solid line, respectively).

For large betatron amplitudes, which upper limit is given by the beam pipe diameter, the power growth has it sources in the energy dependency of the electron trajectory. Modulations in the beam energy change the path length of the trajectories. The bunching is not only enhanced by the longitudinal velocity modulation, as it is mentioned above, but also by run time differences, acting as a bunch compression on the compression scale of the resonant wavelength. The largest com-

pression occurs if the beam has passed a strong deflecting field as it is the case for a large beam offset in a quadrupole field. Fig. 4 shows this enhanced emission by compression for an offset of 3 mm. Two spikes in the growth rate are visible which are clearly correlated with the turning point of the betatron oscillation. For larger amplitudes the growth is not as localized as in Fig. 4 but rather distributed over the remaining length of the undulator.

4. Conclusion

Beside a slight enhancement of the radiation power the simulations show that a kick of 1 mm is sufficient to almost disable the FEL process. This allows to probe the state of amplification at various positions along the undulator, which is an important task to compare the measurements with the theory or simulations.

5. Acknowledgment

The author would like to thank B. Faatz and J. Roßbach for their useful discussions.

References

[1] J. Roßbach *et al.*, Nucl. Inst. & Meth. **A375** (1996) 269

[2] S.V. Milton *et al.*, Nucl. Inst. & Meth. **A407** (1998) 210

[3] R. Tatchyn *et al.*, Nucl. Inst. & Meth. **A375** (1996) 274

[4] Linear Collider Conceptual Design Report, DESY print 97-48, Hamburg, DESY, 1997

[5] A.M. Kondratenko and E.L. Saldin, Par. Acc.**10** (1980) 207

[6] R. Bonifacio, C. Pellegrini and L.M. Narducci, Opt. Comm. **50** (1984) 373

[7] S. Reiche, Proc. of the FEL98-Conference, Wiliamsburg, 1998

[8] B.M. Kincaid, J. Opt. Soc. Am. **B2** (1985) 1294

[9] H.D. Shay and E.T. Scharlemann, Nucl. Inst. & Meth. **A272** (1988) 601

[10] B.L. Bobbs *et al.*, Nucl. Inst. & Meth. **A296** (1990) 574

[11] B. Faatz, J. Pflüger and Y.M. Nikitina, Nucl. Phys. & Meth. **A393** (1997) 380

[12] L.H. Yu *et al.*, Phys. Rev. **A45** (1992) 1163

Field Calculation for Charged Bunches on General Trajectories

K. Rothemund [a,1], M. Dohlus [b], U. van Rienen [a]

[a] *Institut für Allgemeine Elektrotechnik, Universität Rostock, Albert Einstein-Straße 2, D-18051 Rostock, Germany*

[b] *DESY - Deutsches Elektronen Synchrotron, Notkestraße 85, D-22607 Hamburg, Germany*

Abstract

Free Electron Lasers need very short bunches of high charge which are produced in bunch compressors with bended and dispersive trajectories. In addition to the usual space charge effects ($\propto 1/\gamma^2$) other coherent fields (for example coherent synchrotron radiation) appear depending on the path and the charge distribution. To compute such effects, programs like TraFiC^4 (*Tra*ck and *Fi*eld of *C*ontinuous *C*harges in *C*artesian *C*oordinates) were developed. These programs calculate the electromagnetic fields of charge distributions as well as their effects on a test charge under very general conditions. This paper will discuss principle methods to calculate these fields and especially will describe the algorithm underlying TraFiC^4 .

1. Introduction

Free Electron Lasers need very high peak current to generate self-amplified spontaneous emission (SASE) which is produced by compressing a highly charged bunch in dispersive bunch compressor sections. Due to curved trajectories in these components wake fields excited by the passing bunch will have the possibility to interact with the bunch itself. The radiation emitted by the tail overtakes the bunch and reaches the head which may cause emittance growth [1].

To estimate this effect on the bunch, the particle-field interaction has to be calculated. If a given source distribution is strongly affected by the coherent fields this has to be done in a self consistent way, taking into account the change of the charge distribution under the influence of the field. This results in a time dependent description of the bunch distribution respecting the boundary conditions such as free space, perfect conducting planes or real chambers with a certain geometry. A non-self-consistent perturbation approach assumes that the deformation of the bunch shape is weak. The external fields (dc and rf) are used to determine the path and shape variation of a source bunch. For this source bunch the coherent fields are calculated, taking into account the curved path and the shape variation (due to the external fields).

Field calculation methods in general can be divided in several categories:

Modal techniques use the field distribution of a sufficient number of eigenmodes to approximate the field. In the case of short bunches a very large number of modes are stimulated which in general cannot sufficiently be computed. Therefore this method is only useful for geometries with analytically known solutions.

The numerical solution of differential equations (FDTD, FEM etc) is used by particle-in-cell (PIC) codes, which track charged particles forming the bunch under the influence of the fields. It works well for perfect electrically conducting (PEC) boundaries but problems occur when open boundaries are needed. An enormous amount of computation power is needed because the whole field of the considered space is calculated simultaneously and a fine dicretization is necessary.

Integral equations need the retarded source distribution.This is only a problem of storing the informations about the history of the bunch. The complexity of the problem rises when using electrically conducting boundaries (mirror charges). On the other hand, the field has to be calculated only for the points of interest.

With non-self consistent calculations all these methods can be used in time domain as well as in frequency domain. In the case of self consistent

[1] Work supported by DESY, Hamburg

computations only the present and past state of the source distribution is known. So the Fourier transformation is not applicable and the frequency domain method can not be used.

TraFiC^4 stands for "*Tra*ck and *Fi*eld of *C*ontinuous *C*harges in *C*artesian *C*oordinates". TraFiC^4 uses the method of integration of retarded fields which is done by direct numerical integration for 1D- and 2D-bunches. It is proposed to use a convolution method for 2D- and 3D-bunches [2]. The source distribution is modeled by subdividing the bunch into a sufficient number of sub-bunches with individual energy, charge and path; the charge distribution of the sub-bunches is fixed during the calculation. The path of the bunch and the test-particle can be specified in full 3D. TraFiC^4 can handle either free space boundary conditions or two parallel perfect electrically conducting (PEC) planes.

2. Theory

The motion of electrically charged particles is ruled by the Lorentz force:

$$\mathbf{F} = q(\mathbf{E} + \mathbf{v} \times \mathbf{B}) \tag{1}$$

with $\mathbf{E} = -\nabla\phi - \frac{\partial}{\partial t}\mathbf{A}$ and $\mathbf{B} = \nabla \times \mathbf{A}$. Assuming a linear charge distribution $\lambda(s,t)$ and current distribution $i(s,t)\hat{\mathbf{e}}_s(s)$ along the path $\mathbf{r}_b(s)$, the potentials are then given by

$$\phi(\mathbf{r}',t) = \frac{1}{4\pi\epsilon}\int_{-\infty}^{\infty}\frac{\lambda(\mathbf{r}',t')}{|\mathbf{r}-\mathbf{r}'_\mathbf{b}|}ds \tag{2}$$

$$\mathbf{A}(\mathbf{r}',t) = \frac{1}{4\pi\epsilon}\frac{1}{c_0^2}\int_{-\infty}^{\infty}\frac{\mathbf{i}(\mathbf{r}',t')}{|\mathbf{r}-\mathbf{r}'_\mathbf{b}|}ds \tag{3}$$

Taking into account the finite velocity of the field propagation the total force on a test particle with the charge q then is given by

$$\begin{aligned}\frac{4\pi\epsilon}{q}\mathbf{F} = {} & \beta_t\int_{h_a}^{h_b}(\hat{\mathbf{e}}_t-\hat{\mathbf{e}}_s)\times\hat{\mathbf{e}}_s\times\mathbf{G}\beta_s\,ds + \\ & \int_{h_a}^{h_b}(1-\beta_s\beta_t)\mathbf{G}ds - \beta_t\int_{h_a}^{h_b}\frac{\lambda(s,t')}{R}\beta_s\frac{\partial}{\partial s}\hat{\mathbf{e}}_s ds - \\ & \int_{h_a}^{h_b}\left(\frac{\dot{\lambda}(s,t')}{c_0 R}(\beta_t-\beta_s)\right)\hat{\mathbf{e}}_s ds\end{aligned} \tag{4}$$

with $\beta_\mathbf{t} = \mathbf{v_t}/c_0$ the velocity factor of the test-particle, $t' = t - \frac{R}{c_0}$ and c_0 the speed of light where $\mathbf{G} = -\nabla\frac{\lambda(s,t')}{R} = \nabla R\left(\frac{\lambda(s,t')}{R^2} - \frac{\dot{\lambda}(s,t')}{R}\right)$. Eq. (4) is numerically integrated by the field solver of TraFiC^4 for each sub-bunch at every time step.

A more realistic model can be achieved by the following charge and current distribution can be chosen:

$$\rho_F(s,\hat{z},t) = \frac{\lambda(s,t)\;\eta(\hat{z})}{\hat{\mathbf{e}}_z\hat{\mathbf{e}}_s(s)} \tag{5}$$

$$\mathbf{J}_F(s,\hat{z},t) = \frac{i(s,t)\;\eta(\hat{z})\hat{\mathbf{e}}_s(s)}{\hat{\mathbf{e}}_z\hat{\mathbf{e}}_s(s)} \tag{6}$$

with $\int_{-\infty}^{\infty}\eta(z)dz = 1$. The integrals for $\mathbf{F}$ can be derived from (4) by the substitution

$$\frac{i(s,t')}{c_0 R} \longrightarrow I(s,t') = \int\frac{i(s,t')\;\eta(\hat{z})}{c_0 R}d\hat{z} \tag{7}$$

$$\frac{\lambda(s,t')}{R} \longrightarrow L(s,t') = \int\frac{\lambda(s,t')\;\eta(\hat{z})}{R}d\hat{z} \tag{8}$$

where R now is given by $R(s,\hat{z}) = |\mathbf{r} - \mathbf{r}_{sz}(s,\hat{z})|$. To calculate the wake fields of a 2D-bunch distribution 2D-integrals have to be computed which increases the numerical effort.

3D bunches are not implemented in TraFiC^4 directly. But they can be modeled by creating an ensemble of 2D sub-bunches. This is possible because the fields of the 2D-bunches have no singularity.

3. Outlook

TraFiC^4 has already been used to design bunch compressor sections but some improvements in the efficiency of the field calculation are foreseen. For example, when computing the effect of PEC planes on the bunch, the number of the mirror charges taken into account should be detected automatically or, if necessary, approximated by interpolation. To improve the local approximation of the bunch charge distribution, an adaptive adjustment of the sub-bunch parameters is planned. An improved control of the step size during the 1D integration for less smooth functions is intended to reach a higher accuracy of the numerical calculation.

References

[1] Ya.S. Derbenev and V.D. Shiltsev. Transverse effects of microbunch radiative interaction. Technical report, Fermi National Accelerator Laboratory, May 1996.

[2] M.Dohlus, A.Kabel, and T.Limberg. Efficient field calculation of 3d bunches on general trajectories. In *FEL99 (same conference).*

[3] Richard Talman. Novel relativistic effect important in accelerators. *Physical Review, Letters*, 56(14):1429–1432, April 1986.

Free Electron Laser for Gamma-Gamma Collider at TESLA

E.L. Saldin [a], E.A. Schneidmiller [a], M.V. Yurkov [b]

[a] *Deutsches Elektronen-Synchrotron, Notkestrasse 85, D-22607, Hamburg, Germany*

[b] *Joint Institute for Nuclear Research, Dubna, 141980 Moscow Region, Russia*

Abstract

The present paper contains the results of optimization of the free electron laser for the gamma-gamma collider at TESLA. A superconducting linear accelerator, similar to the TTF (TESLA Test Facility) accelerator, produces a driving electron beam for the FEL. The MOPA FEL scheme is studied when the radiation from a master oscillator is amplified in the FEL amplifier with tapered undulator. The FEL produces the radiation of TW level with the wavelength of 1 μm. Optimization of the FEL amplifier is performed with three-dimensional, time-dependent simulation code FAST.

1. Introduction

A second interaction region is under discussion in the TESLA linear collider project which is intended for gamma-e and gamma-gamma collisions [1]. The idea of the gamma-gamma collider takes its origin in the early 80's when it has been shown that a high luminosity colliding gamma-gamma beams can be produced by means of the Compton backscattering of powerful FEL radiation on the electrons of the main accelerator [2,3]. The conceptual scheme for organization of gamma-gamma collisions (see Fig. 1) can be explained as follows. Two electron (or electron and positron) bunches are focused into the interaction point. Prior the collision each electron bunch is irradiated by a powerful laser pulse. High energy gamma-quanta are produced in the process of Compton backscattering and, following the electron trajectories, collide at the interaction region. The time structure of the laser pulses should be identical to the time structure of the electron bunches. It means, that the laser should have a capability of precise synchronization (with an accuracy of about 1 ps) with the electron bunches and should provide a high repetition rate. In the case of the TESLA collider a sub-terawatt level peak power laser is required with the repetition rate of about 1 MHz. The average power should be of the order of 10 kW. The laser radiation should be circularly polarized and

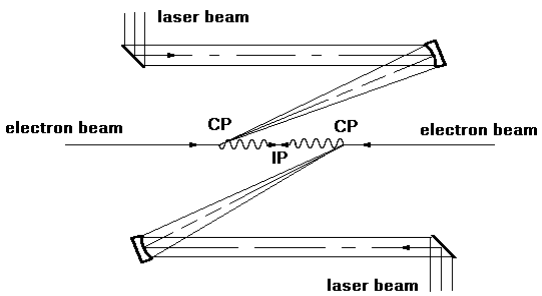

Fig. 1. Conceptual scheme of a gamma-gamma collider.

* FEL'99 Conference, Hamburg, August 23-27, 1999
Report No. Tu-P-50

transversely coherent. A reliable technical solution for a conventional laser system with required parameters seems to be a problem. Indeed, even optimistic estimation of the scale of the conventional laser facility shows that the laser equipment should occupy an area of about 50 000 m^2. The cost of the equipment is estimated as 200 M$ [4].

On the other hand, the FEL technique provides a possibility to construct the laser system which meets all the requirements for the PLC [3,5–7]. Indeed, the FEL can provide a high efficiency, it is tunable and capable to generate powerful coherent radiation which always has minimal (i.e. diffraction) dispersion. With a sufficient quality of the driving electron beam, the FEL peak output power is defined by the peak power of this driving beam. At an electron beam energy of $\mathcal{E} \sim 1$ GeV and a peak beam current of $I \sim 1$ kA, this power reaches the TW level. The problem of synchronization can be solved naturally as it is based totally on the accelerator technology. The FEL output radiation is totally polarized: circularly or linearly for the case of helical or planar undulator, respectively. This feature of the FEL radiation reveals wide possibilities to steer the helicity and energy spectrum of colliding gamma quanta [6]. An option of a free electron laser for the gamma-gamma collider is considered now in the TESLA project [1,7].

2. FEL system for gamma-gamma collider

FEL system is built as a MOPA scheme where the low-power radiation from Nd glass laser ($\lambda = 1$ μm) is amplified in a long tapered undulator by an electron beam. The driving accelerator has the same time diagram as the main TESLA linac.

2.1. Accelerator

Driving electron beam for the FEL is produced by the accelerator based on TESLA technology and similar to the TTF (TESLA Test Facility) accelerator [8]. Parameters of the accelerator are presented in Table 1. The beam with the charge of 12 nC and normalized emittance of 30π mm mrad is generated in photoinjector, accelerated in superconducting modules with the gradient 20 - 25 MV/m and compressed down to 2 ps duration in the bunch compressors. Note that the emittance is not a critical parameter for considered FEL.

2.2. Master laser

The peak power of the master laser with the wavelength of 1 μm is assumed to be 1 MW with pulse duration of several picoseconds, so that the average power will be below 0.1 W. It means that only small fraction of power can be taken out of 2 W of infrared radiation generated in the laser system of photoinjector. Then this radiation can be transported to the undulator entrance. The problem of synchronization of electron and optical bunches is, therefore, solved naturally.

2.3. FEL amplifier

To obtain reasonable luminosity of the gamma-gamma collider at TESLA, the energy in radiation pulse at the FEL amplifier exit should be above 2 J and peak power should reach sub-terawatt level. For chosen parameters of electron beam it means that the FEL efficiency must exceed 10 %. In FEL amplifier with uniform undulator the efficiency is limited by saturation effects and is below 1 % in the considered case. Saturation of the radiation power in the FEL amplifier occurs due to the energy losses by the particles which fall out of the resonance with the electromagnetic wave. Nevertheless, effective amplification of the radiation is possible in the nonlinear regime by means of using a tapered undulator [9]. In this case large fraction of particles is trapped in the effective potential of interaction with electromagnetic wave and is decelerated.

Table 1
Parameters of the accelerator

Energy	1.5 GeV
Charge per bunch	12 nC
Peak current	2.4 kA
Bunch length (RMS)	0.6 mm
Normalized emittance	30π mm mrad
Energy spread (RMS)	1 MeV
Repetition rate	5 pps
Macropulse duration	800 μs
# of bunches per macropulse	1130
Bunch spacing	708 ns
Average beam power	102 kW

Table 2
Parameters of the FEL amplifier

Undulator	
Type	Helical
Period	10 cm
Magnetic field (entr./exit)	1.4 T / 1.08 T
Total length	60 m
Length of untapered section	10.7 m
Beam size in the und. (RMS)	230 μm
Radiation	
Wavelength	1 μm
Dispersion	Dif. limit
Pulse energy	2.2 J
Pulse duration (HWHM)	4 ps
Repetition rate	5 pps
Macropulse duration	800 μs
# of pulses per macropulse	1130
Peak output power	0.7 TW
Average power	12.5 kW
Efficiency	12.2 %

Parameters of the FEL amplifier with the tapered undulator are presented in Table 2. The undulator is helical to provide polarized radiation and is superconducting what seams to be natural solution in the context of TESLA. The resonance is maintained by decrease of the magnetic field at fixed period of the undulator.

We begin our study with analysis of physical effects influencing the operation of the FEL amplifier. Within the scope of the three-dimensional theory of the FEL amplifier we obtain that all the important physical effects are connected with the corresponding dimensionless parameters defining the power of the effect. These parameters are the diffraction parameter B, the space charge parameter $\hat{\Lambda}_{\rm p}^2$, the parameter of the longitudinal velocity spread $\hat{\Lambda}_{\rm T}^2$ and the efficiency parameter ρ [12]:

$$
\begin{aligned}
B &= 2\Gamma\sigma_{\rm r}^2\omega/c \\
\hat{\Lambda}_{\rm p}^2 &= \Lambda_{\rm p}^2/\Gamma^2 = 4c^2(\theta_{\rm s}\sigma_{\rm r}\omega)^{-2} \ , \\
\hat{\Lambda}_{\rm T}^2 &= \Lambda_{\rm T}^2/\Gamma^2 = (\sigma_{\rm E}^2/\mathcal{E}_0^2 + \gamma_{\rm z}^4\sigma_\theta^4/4)/\rho^2 \ , \\
\rho &= c\gamma_{\rm z}^2\Gamma/\omega .
\end{aligned}
$$

The gain parameter Γ defines the scale of the field gain and is defined as

$$
\Gamma = \left[I\omega^2\theta_{\rm s}^2/(I_{\rm A}c^2\gamma_{\rm z}^2\gamma)\right]^{1/2} \quad ,
$$

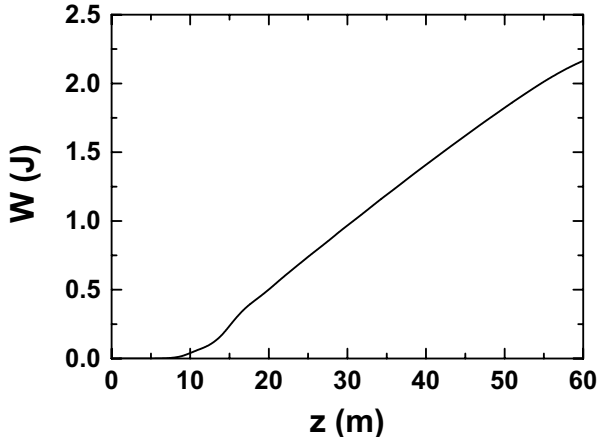

Fig. 2. Energy in the radiation pulse versus the undulator length.

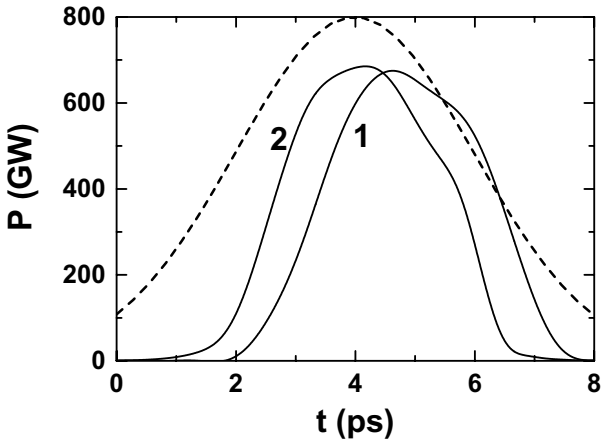

Fig. 3. Time structure of the radiation pulse at the exit of the FEL amplifier (curve 1) and of the power loss in the electron bunch (curve 2). Dashed line is the longitudinal profile of the electron bunch (maximal value of the beam current is equal to 2.4 kA).

where $\omega = 2\pi c/\lambda$ is the frequency of the radiation field and $I_{\rm A} = m_{\rm e}c^3/e$. To be specific, we have written all the formulae for the case of the gaussian distribution of the electrons in the transverse phase space with the RMS radius and the RMS angle spread given by $\sigma_{\rm r} = \sqrt{\epsilon_{\rm n}\beta/\gamma}$ and $\sigma_\theta = \sqrt{\epsilon_{\rm n}/\beta\gamma}$, where $\epsilon_{\rm n}$ is rms normalized emittance, β is focusing beta function and $\gamma = \mathcal{E}_0/m_{\rm e}c^2$ is relativistic factor. Energy spread in the electron beam is assumed to be gaussian with the rms deviation $\sigma_{\rm E}$. Undulator is assumed to be a helical one with amplitude of the magnetic field $H_{\rm w}$ and period $\lambda_{\rm w}$. The undulator parameter K, the electron rotation angle $\theta_{\rm s}$ and the longitudinal relativistic factor $\gamma_{\rm z}$: $K = eH_{\rm w}\lambda_{\rm w}/2\pi m_{\rm e}c^2$, $\theta_{\rm s} = K/\gamma$

and $\gamma_z^2 = \gamma^2/(1+K^2)$.

The main effects influencing on the operation of the FEL amplifier with tapered undulator are the diffraction effect and the slippage effect. Calculations based on the steady-state theory [10] show that at the length of the undulator of 60 m, the efficiency of the FEL amplifier is about 20 %. Axial inhomogenity of the beam current leads to visible reduction of the efficiency. Also, at such a length of the undulator one should take into account the finite length of the electron bunch. Kinematic slippage of the radiation with respect to the electron bunch is 0.6 mm which what is comparable with the bunch length. So, steady-state approach can be used only for rough estimations, and parameters of the FEL amplifier should be optimized using time-dependent approach. Here we present results of optimization performed with three-dimensional, time-dependent code FAST [11]. The efficiency 12.2 % is reached in the end of the undulator, what corresponds to 2.2 J in optical pulse (see Fig. 2). In Fig. 3 we present time structure of the radiation pulse at the undulator exit. One can see that the slippage of the radiation pulse is visibly less than the kinematic slippage of about 0.6 mm (or, 2 ps). This is explained by the fact that the group velocity of the radiation in the electron beam, $v_g^{-1} = \mathrm{d}k/\mathrm{d}\omega$, is less than the velocity of light. Fig. 4 illustrates suppression of the slippage rate in the linear regime of the FEL amplifier operation. In the case under study the value of diffraction parameter is $B \simeq 0.5$, and the slippage effect is suppressed by a factor of 5. Suppression of the slippage effect in the tapered regime is not so strong, but is still significant as it is illustrated with Fig. 3. So, we find that the effect of suppression of the slippage effect reveals the possibility to use short electron bunches for effective amplification of the radiation in a long undulator.

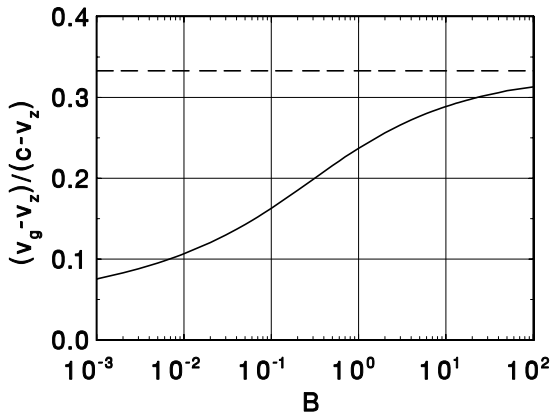

Fig. 4. Ratio of the slippage rate of the radiation wavepacket and kinematic slippage rate, $(v_g - \bar{v}_z)/(c - \bar{v}_z)$, as function of diffraction parameter B. Dotted line represents one-dimensional asymptote.

References

[1] "Conceptual Design of a 500 GeV e+e− Linear Collider with Integrated X-ray Laser Facility" (Editors R.Brinkmann, G. Materlik, J. Rossbach, A. Wagner), DESY 97-048, Hamburg, 1997.

[2] I.F. Ginzburg et al., Pis'ma v ZhETF **34**(1981)514, Preprint INF 81-50, Novosibirsk (1981), in Russian

[3] A.M. Kondratenko, E.V. Pakhtusova and E.L. Saldin, Dokl. Akad. Nauk **264**(1982)849, Preprint INF 81-130, Novosibirsk (1981), in Russian

[4] V.I. Telnov, private communication.

[5] E.L. Saldin, V.P. Sarantsev, E.A. Schneidmiller and M.V. Yurkov, Nucl. Instrum. and Methods **A339**(1994)583

[6] E.L. Saldin, V.P. Sarantsev, E.A. Schneidmiller and M.V. Yurkov, "Photon Linear Colliders of TeV Energy Range", Preprint JINR E-9-94-74, Dubna, 1994. Submitted to Particle Accelerators

[7] E. L. Saldin et al., Nucl. Instrum. and Methods **A361**(1995)101.

[8] "TESLA Test Facility Linac - Design Report" (Editor D. A. Edwards), DESY Print TESLA 95-01, Hamburg, 1995.

[9] N. Kroll, P. Morton and M. Rosenbluth, SRI Rep. JSR-79-01
IEEE J. Quantum Electron. **QE-17**(1981)1436.

[10] E.L. Saldin, E.A. Schneidmiller and M.V. Yurkov, Opt. Commun. **95**(1993)141.

[11] E.L. Saldin, E.A. Schneidmiller and M.V. Yurkov, Nucl. Instrum. and Methods **A429**(1999)233–237.

[12] E.L. Saldin, E.A. Schneidmiller and M.V. Yurkov, Phys. Rep. **260**(1995)187.

Optimization of a Seeding Option for the VUV Free Electron Laser at DESY

E.L. Saldin [a], E.A. Schneidmiller [a], M.V. Yurkov [b]

[a] *Deutsches Elektronen-Synchrotron (DESY), Notkestrasse 85, D-22607 Hamburg, Germany*

[b] *Joint Institute for Nuclear Research, Dubna, 141980 Moscow Region, Russia*

Abstract

In order to get fully coherent radiation from the FEL amplifier starting from the shot noise, it is foreseen to implement a seeding option into the VUV FEL being under construction at DESY [1,2]. It consists of an additional undulator, a bypass for electrons and an X-ray monochromator. This paper presents the results of optimization of the seeding option for the VUV FEL providing maximal spectral brightness at minimal shot-to-shot intensity fluctuations. Calculations are performed with three-dimensional, time-dependent simulation code FAST [3].

1. Introduction

Free-electron laser technique provides the possibility to extend the energy range of lasers into the X-ray regime using a single-pass FEL amplifier scheme starting from noise. One particular feature of the FEL amplifier is its rather large amplification bandwidth. This can be considered an advantage when the FEL amplifier amplifies the narrow bandwidth radiation of a master laser, but in the case when the process of amplification starts from noise, it produces relatively wide band output radiation. For instance, the bandwidth of the 6 nm conventional single-pass SASE FEL at DESY would be about 0.5 % [1]. The shape of the spectrum is not smooth but spiked. To perform experiments which require a narrow bandwidth of the output radiation, a monochromator has to be installed at the FEL amplifier exit. The shot-to-shot fluctuations of the radiation power after this monochromator will increase with increasing energy resolution. Moreover, conventional X-ray optical elements will suffer from heat load due to the high output radiation power and probably filters have to be installed before the monochromator. As a result, the brilliance of the FEL radiation available at the experimental station might be reduced significantly.

A novel scheme of a two-stage single-pass SASE FEL has been proposed in paper [4]. The FEL

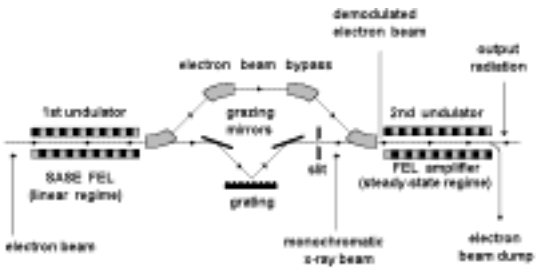

Fig. 1. The principal scheme of single pass two stage SASE X-ray FEL with monochromator.

* FEL'99 Conference, Hamburg, August 23-27, 1999
Report No. We-P-40

Table 1
Parameters of the two-stage SASE FEL

Electron beam	
Energy, $\mathcal{E}_0$	1000 MeV
Peak current, I_0	2500 A
rms bunch length, σ_z	5×10^{-3} cm
rms normalized emittance	2πmm mrad
rms energy spread	0.1 %
External β-function,	300 cm
rms transverse beam size	57 μm
Number of bunches per train	7200
Repetition rate	10 Hz
Undulator	
Type	Planar
Period, λ_w	2.73 cm
Peak magnetic field, H_w	4.97 kGs
Length of 1st undulator	13 m
Length of 2nd undulator	17 m
Output radiation	
Wavelength, λ	6.4 nm
Bandwidth, $\Delta\lambda/\lambda$	7×10^{-5}
rms angular divergence	15 μrad
rms spot size	90 μm
Time of coherence, τ_c	100 fs
Power average over pulse	2 GW
Flash energy	0.6 mJ
Fluctuations of the flash energy	5 %
Average power	40 W

scheme consists of two undulators and an X-ray monochromator located between them. The first undulator operates in the linear regime of amplification starting from noise and the output radiation has the usual SASE properties [5]. After the exit of the first undulator the electron is guided through a bypass and the X-ray beam enters the monochromator which selects a narrow band of radiation. At the entrance of the second undulator the monochromatic X-ray beam is combined with the electron beam and is amplified up to the saturation level.

In this paper we study the operation of the seeding option of the SASE FEL at DESY using three-dimensional, time-dependent code FAST [3].

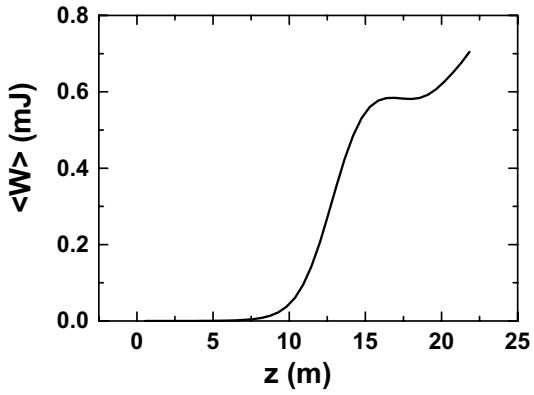

Fig. 2. Averaged energy in the radiation pulse in the second stage of the two-stage FEL amplifier as a function of undulator length. The input power fluctuates in accordance with the negative exponential distribution with the average value of 35 kW.

2. Operation of a two-stage SASE FEL at DESY

Parameters of the seeding option of VUV FEL at the TESLA Test Facility at DESY are presented in Table 1. The characteristics of the two-stage SASE FEL are presented in Figs. 2–7. The FEL process in both undulators has been calculated using the three-dimensional, time-dependent code FAST [3]. Since the FEL process starts from the shot noise, the calculation of the FEL characteristics requires large number of statistically independent runs [5]. The results, presented below, are calculated over 40 independent runs which provide the accuracy of the characteristics of about few per cent. During each simulation run we calculated the radiation produced by the whole electron bunch taking into account the shot noise in the electron beam in both undulators. It has been assumed that the longitudinal profile of the electron bunch is the Gaussian one with $\sigma_z = 50$ μm.

The first stage of the SASE FEL of 13 m length operates in a linear high-gain regime with a power gain of $G^{(1)} \simeq 5 \times 10^5$. This value is by 100 times less than the power gain at saturation, $G_{sat}(\mathrm{SASE}) \simeq 10^8$. At such a choice of the power gain in the first stage the energy spread induced by the FEL process is $\Delta\sigma_{\mathcal{E}}/\mathcal{E} \simeq 10^{-4}$ which is much less than the initial energy spread in the beam, $\sigma_{\mathcal{E}}/\mathcal{E} \simeq 10^{-3}$. The output power averaged over the radiation pulse is equal to 30 MW. The spectral bandwidth of the output radiation is about $(\Delta\lambda/\lambda)_{\mathrm{SASE}} \simeq 0.5\%$. Output radiation

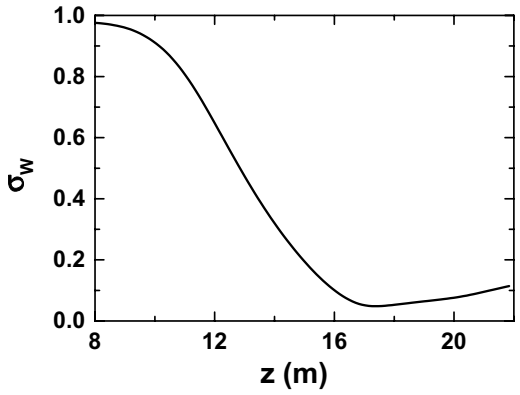

Fig. 3. The dependence of the standard deviation of the fluctuations of the output energy in the radiation pulse as a function of the undulator length ($\sigma_W^2 = \langle W^2 - \langle W \rangle^2 \rangle / \langle W \rangle^2$).

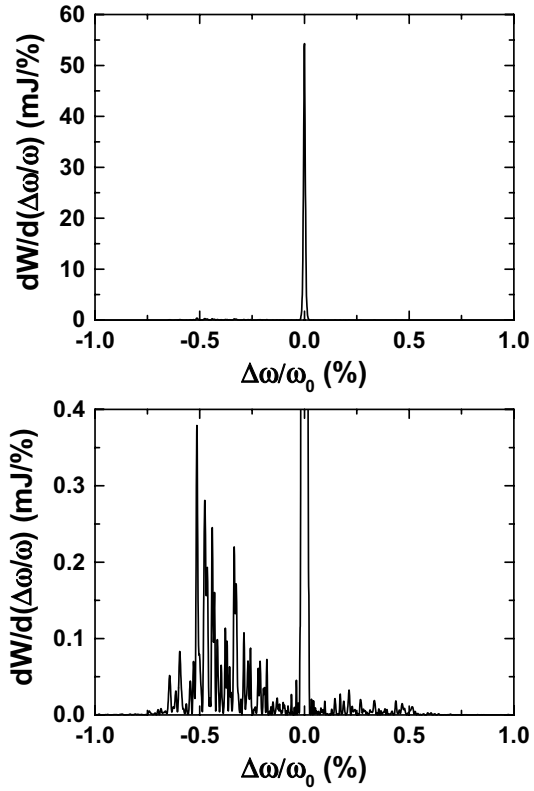

Fig. 4. Upper plot: Spectral distribution of the energy in one radiation pulse at the length of the second undulator equal to 17 m. The lower plot illustrates the level of the shot noise contribution.

from the first stage has full transverse coherence and transverse distribution of the radiation field corresponds to fundamental TEM_{00} mode of the FEL amplifier.

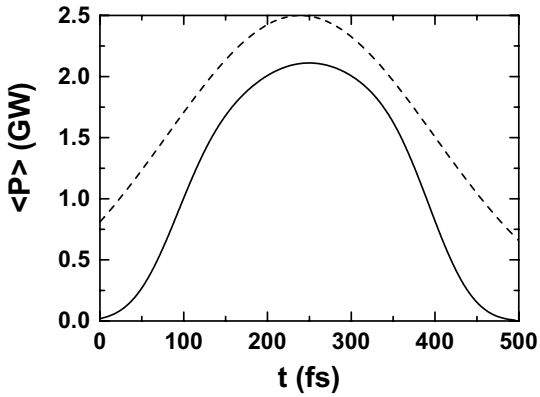

Fig. 5. Averaged temporal structure of the radiation pulse at the undulator length of 17 m. The dashed line presents the corresponding distribution of the electron beam current.

The monochromator for the TTF-FEL selects narrow band of radiation, $\Delta\omega/\omega \simeq 5 \times 10^{-5}$. Total transmission of the monochromator is equal to 9 % [2]. The radiation power after monochromator fluctuates in accordance with the negative exponential distribution, $w(P)dP = \exp(-P/\langle P \rangle)dP/\langle P \rangle$ with the average value $\langle P \rangle \simeq 35$ kW. This radiation is amplified in the second undulator.

The modulation of the electron beam induced in the first undulator is suppressed prior arrival of the electron bunch to the entrance of the second undulator. This is possible because of the finite value of the natural energy spread in the beam and special design of the electron bypass [2]. As a result, at the chosen parameters for the first stage of the SASE FEL and the monochromator the radiation power from the monochromator dominates significantly over the shot noise and the residual electron bunching.

The characteristics of the two-stage SASE FEL are presented in Figs. 2–7. The dependence of the average (shot-to-shot) energy in the radiation pulse is presented in Fig. 2. The mean squared deviation of the fluctuations of the radiation energy, $\sigma_W^2 = \langle W^2 - \langle W \rangle^2 \rangle / \langle W \rangle^2)$, is presented in Fig. 3. It is clearly seen that when the FEL amplifier operates in the linear regime, the value of σ_W is close to the unity. The energy fluctuations are reduced drastically when the FEL amplifier operates in the nonlinear regime. Minimal value of the fluctuations, $\sigma_W \simeq 5$ %, occurs at the undulator length of 17 m. This value is mainly defined by the stabilization near the saturation point of

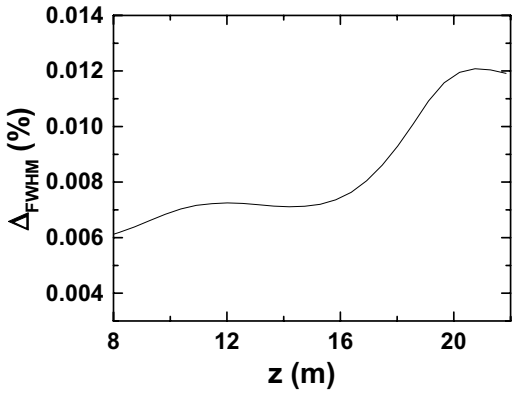

Fig. 6. FWHM width of the spectrum peak shown in Fig. 4 versus the undulator length.

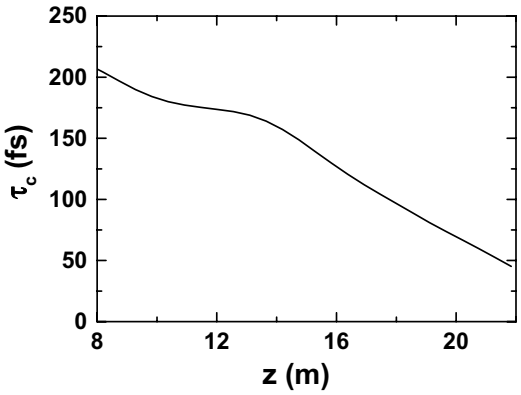

Fig. 7. Correlation time, τ_c, of the radiation versus the undulator length.

the amplitude characteristic of the FEL amplifier with gradient axial profile of the electron bunch. The growth of the energy fluctuations after this point is connected with the growth of spikes in the nonlinear medium, since we have taken into account the shot noise in the electron beam.

So, we find that there exist optimal length of the second undulator. Typical spectrum of one radiation pulse at the undulator length of 17 m is presented in Fig. 4. Its is seen that the contribution of the shot noise in the total radiation power is small. An important characteristic of the radiation is the width of the peak in the radiation spectrum corresponding to the seeding signal (see Fig. 6). The width of the radiation spectrum at the undulator length of 17 m is equal to $\Delta\omega/\omega \simeq 7 \times 10^{-5}$ and is defined mainly by the finite pulse duration (see Fig. 5).

The most general characteristic of the radiation pulse is the time of coherence τ_c (see Fig. 7). This quantity is related to the first order time correlation function, $g_1(\tau)$, as

$$\tau_c = \int_{-\infty}^{\infty} \mid g_1(\tau) \mid^2 d\tau \ .$$

The value of $g_1(\tau)$ have been calculated via Fourier transform of averaged radiation energy spectral density.

Acknowledgments

We are grateful to J. Feldhaus, and J.R. Schneider for many useful discussions.

References

[1] "A VUV Free Electron Laser at the TESLA Test Facility: Conceptual Design Report", DESY Print TESLA-FEL 95-03, Hamburg, DESY, 1995.

[2] "Seeding Option for the VUV Free Electron Laser at DESY": Joint DESY and GKSS Proposal. Available at DESY by a request only.

[3] E.L. Saldin, E.A. Schneidmiller and M.V. Yurkov, Nucl. Instrum. and Methods **A429**(1999)233–237.

[4] J. Feldhaus, E.L. Saldin, J.R. Schneider, E.A. Schneidmiller and M.V. Yurkov, Optics Communications **140**(1997)341.

[5] E.L. Saldin, E.A. Schneidmiller and M.V. Yurkov, Opt. Commun. **148**(1998)383.

Green's Function of Homogeneous Overmoded Waveguide with Finite Conductivity Walls

E.L. Saldin [a], E.A. Schneidmiller [a], M.V. Yurkov [b]

[a] *Deutsches Elektronen-Synchrotron (DESY), Notkestrasse 85, D-22607 Hamburg, Germany*

[b] *Joint Institute for Nuclear Research, Dubna, 141980 Moscow Region, Russia*

Abstract

We describe an approach for developing the numerical simulation codes for the FEL amplifier with the homogeneous overmode waveguide. The radiation field are calculated using Green's function method. We start with the regorous solutions for the eigenfunctions of a passive waveguide. Using these eigenfunctions, we find the Green's function. Finally, the Green's function is simplified using paraxial approximation. This algorithm of electromagnetic field calculation can be implemented in linear and nonlinear code for simulation of the waveguide FEL.

1. Formulation of the problem

To describe the FEL amplifiers operating in the millimeter or far infrared wavelenth range, one should take into account the influence of the waveguide walls on the amplification process. The most comprehensive study of the waveguide FEL is presented in the book [1]. The reader can find there extended list of the references to original papers relevant to the problem. The present study assumes a waveguide to be overmoded. Such an approximation does not reduce significantly the practical applicability of the obtained results. Indeed, the FEL amplifier has advantage against conventional vacuum tube devices only when the undulator period λ_w is much larger than the radiation wavelength λ. The FEL resonance condition is $\lambda_w/v_z = \lambda/(v_{ph} - v_z)$, where v_z is the longitudinal velocity of the electrons and v_{ph} is the phase velocity of the electromagnetic wave:

$$v_{ph} = c\left(1 - c^2 k_\perp^2/\omega^2\right)^{-1/2} \quad .$$

Here $k_\perp$ is the transverse wavenumber of the wave. It is obvious that parameter $c^2 k_\perp^2/\omega^2$ should be much less than unity when $\lambda_w \gg \lambda$, i.e. the waveguide should be overmoded.

The operation of the FEL amplifier with an overmoded waveguide can be described by different methods. Our approach is based on the method of the Green's function. We start with the rigorous solutions for the eigenfunctions of a passive waveguide. Using these eigenfunction, we find the Green's function. Finally, the Green's function is simplified using paraxial approximation. The obtained expressions can be implemented in linear and nonlinear codes for simulation of the

* FEL'99 Conference, Hamburg, August 23-27, 1999
Report No. Mo-P-63

FEL amplifiers. In this paper we demonstrate the application of the Green's function for solution of the initial value-problem for the FEL amplifiers with rectangular and circular waveguides.

Let us consider a helical undulator with magnetic field $H_x + H_y = H_\mathrm{w} \exp(-\mathrm{i}\, k_\mathrm{w} z)$. Electrons in the undulator move along the constrained helical trajectory in parallel to the z axis. The electron rotation angle $\theta_\mathrm{s} = K/\gamma$ is assumed to be small and the longitudinal electron velocity v_z is close to the velocity of light, $v_z \simeq c$. A waveguide is placed inside the undulator. The electromagnetic wave propagates in the waveguide in the same direction as the electron beam. For the electron beam with a small density perturbation, the distribution function can be written in the form

$$f = f_0(\mathcal{E}, \vec{r}_\perp) + \tilde{f}_1(z, \mathcal{E}, \vec{r}_\perp) \exp(\mathrm{i}\,\psi) + \mathrm{C.C.}\ .$$

where $\mathcal{E}$ is the energy of electron, phase $\psi = k_\mathrm{w} z - \omega(z/c - t)$.

We consider the initial conditions when an external electromagnetic wave and unmodulated electron beam are fed to the undulator entrance: $\tilde{f}_1|_{z=0} = 0$, $f_0 = n_0(\vec{r}_\perp) F(P)$, where $P = \mathcal{E} - \mathcal{E}_0$, $\int \mathrm{d}\, P F(P) = 1$. The evolution of the perturbation to the distribution function, $\tilde{f}_1$, is described by the Vlasov equation. Integration of the Vlasov equation gives us the relation between the longitudinal component of the beam current density, and amplitude of the wave.

To simplify the consideration, we write the Vlasov equation for the case of negligibly small energy spread in the beam. The initial distribution function is the delta function in this case, $F(P) = \delta(P - P_0)$, and the Vlasov equation can be reduced to

$$\left[\frac{\mathrm{d}^2}{\mathrm{d}\, z^2} + 2\,\mathrm{i}\, C \frac{\mathrm{d}}{\mathrm{d}\, z} + \left(\frac{4\pi e}{c\gamma_z^2 \mathcal{E}_0}\, j_0(\vec{r}_\perp) - C^2\right)\right] \tilde{j}_1 = -\frac{\omega}{c\gamma_z^2 \mathcal{E}_0} j_0(\vec{r}_\perp) U(z,\ \vec{r}_\perp)\ . \qquad (1)$$

Here $j_z = -j_0(\vec{r}_\perp) + \tilde{j}_1 \exp(\mathrm{i}\,\psi) + \mathrm{C.C.}$, is the longitudinal component of the beam current density, $-j_0(\vec{r}_\perp) \simeq -ecn_0(\vec{r}_\perp)$, $C = k_\mathrm{w} - \omega/(2c\gamma_z^2)$ is the detuning of the particle with nominal energy $\mathcal{E}_0$ from resonance with wave, $\gamma_z^{-2} = \gamma^{-2} + \theta_\mathrm{s}^2$.

In the following we assume that the transverse size of the electron beam is rather large, $r_\mathrm{b}^2/\gamma_z^2 \gg c^2/\omega^2$. In particular, it follows from this assumption that we can neglect the reduction of the plasma wavenumber due to the presence of the waveguide walls.

The complex amplitude of the effective potential, U, is connected with the components of the electromagnetic wave by relation

$$U = -\frac{e\theta_\mathrm{s}}{2\,\mathrm{i}} \left[\tilde{E}_x + \mathrm{i}\, \tilde{E}_y\right]\ . \qquad (2)$$

The transverse electric field of the wave is presented in the form:

$$\vec{E}_\perp(z,\ \vec{r}_\perp,\ t) = \Big[\vec{e}_x \tilde{E}_x(z,\ \vec{r}_\perp) + \vec{e}_y \tilde{E}_y(z,\ \vec{r}_\perp)\Big] \exp\left[\mathrm{i}\,\omega(z/c - t)\right] + \mathrm{C.C.}\ , \qquad (3)$$

To close the problem, we should solve Maxwell's equations with the boundary conditions on the waveguide walls and express the fields in terms of the first harmonic of the beam current density.

2. Green's function of homogeneous waveguide

The electromagnetic field is expressed via the vector and the scalar potential as

$$\vec{H} = \vec{\nabla} \times \vec{A} \qquad \vec{E} = -\frac{1}{c}\frac{\partial \vec{A}}{\partial t} - \vec{\nabla}\phi\ . \qquad (4)$$

In the following we use the Coulomb gauge for the potentials,

$$\vec{\nabla} \cdot \vec{A} = 0\ . \qquad (5)$$

Substitution of (4) into the Maxwell's equations gives (at the Coulomb gauge):

$$\vec{\nabla}^2 \vec{A} - \frac{1}{c^2}\frac{\partial^2 \vec{A}}{\partial t^2} = -\frac{4\pi}{c}\vec{j} + \frac{1}{c}\vec{\nabla}\frac{\partial \phi}{\partial t} = -\frac{4\pi}{c}\vec{J}\ , \qquad (6)$$

$$\vec{\nabla}^2 \phi = -4\pi\rho_\mathrm{e}\ , \quad \vec{j} = \vec{v}\rho_\mathrm{e}\ , \qquad (7)$$

where ρ_e is the charge density. It follows from (7) and from the charge conservation law that $\vec{\nabla} \cdot \vec{J} = 0$. In the Coulomb gauge the scalar potential, ϕ, is the static Coulomb potential. The dynamical part of the field is associated with the vector potential, $\vec{A}$, only.

Let us consider a monochromatic external wave of the frequency ω. Then $\vec{A}$, ϕ and $\vec{j}$ may be written as $\vec{A} = \vec{A}_\omega e^{-i\omega t} + \text{C.C.}$, $\phi = \phi_\omega e^{-i\omega t} + \text{C.C.}$, $\vec{j} = \vec{j}_\omega e^{-i\omega t} + \text{C.C.}$. Equation (6) for $\vec{A}_\omega$ and $\vec{J}_\omega = \vec{j}_\omega + i\omega(4\pi)^{-1}\vec{\nabla}\phi_\omega$ takes the form:

$$\vec{\nabla}^2 \vec{A}_\omega + \frac{\omega^2}{c^2}\vec{A}_\omega = -\frac{4\pi}{c}\vec{J}_\omega \ . \qquad (8)$$

We assume the waveguide walls to be perfectly conducting. The boundary conditions for this case force the vector of the electric field be perpendicular to the waveguide wall. In addition to the Coulomb gauge condition (5), we impose the boundary condition for the scalar potential ϕ be equal to zero on the waveguide walls. The boundary conditions for the vector potential $\vec{A}$ are defined by the boundary conditions for the field:

$$\vec{n} \times \vec{A}_\omega|_S = 0 \ , \qquad (9)$$

where $\vec{n}$ is the unit vector perpendicular to the waveguide wall ($|\vec{n}| = 1$).

Under these boundary conditions, the solution of the inhomogeneous Helmholtz equation (8) has the form:

$$A^\alpha_\omega(\vec{r}) = \sum_\beta \int G^{\alpha\beta}_\omega(\vec{r},\ \vec{r}\,')J^\beta_\omega(\vec{r}\,')\,\mathrm{d}\,\vec{r}\,' \ , \qquad (10)$$

where $G^{\alpha\beta}_\omega(\vec{r},\ \vec{r}\,')$ is the tensor Green's function of the waveguide and $\vec{r}$ and $\vec{r}\,'$ are the coordinates of the observation and the source point, respectively. It can be shown that the condition $\phi_\omega|_S = 0$ results in the zero value of the integral [2]:

$$\sum_\beta \int G^{\alpha\beta}_\omega(\vec{r},\ \vec{r}\,')(\vec{\nabla}\phi_\omega(\vec{r}\,'))^\beta\,\mathrm{d}\,\vec{r}\,' = 0 \ . \qquad (11)$$

Hence, (10) takes the form:

$$A^\alpha_\omega(\vec{r}) = \sum_\beta \int G^{\alpha\beta}_\omega(\vec{r},\ \vec{r}\,')j^\beta_\omega(\vec{r}\,')\,\mathrm{d}\,\vec{r}\,' \ . \qquad (12)$$

Using (12), we write the following expression for the electric field of the radiated wave:

$$E^\alpha_\omega(\vec{r}) = i\,\frac{\omega}{c}\sum_\beta \int G^{\alpha\beta}_\omega(\vec{r},\ \vec{r}\,')j^\beta_\omega(\vec{r}\,')\,\mathrm{d}\,\vec{r}\,' \ , \qquad (13)$$

where tensor Green's function, $G^{\alpha\beta}_\omega$, in the paraxial approximation is given by [1]:

$$\begin{aligned} G_\omega = {} & \frac{2\pi i}{\omega}\sum_\mu \exp\left\{i\left[\frac{\omega}{c} - \frac{c(k^{TE}_\perp)^2_\mu}{2\omega}\right]|z - z'|\right\} \\ & \times \left[\vec{e}_x\frac{\partial\psi^{TE}_\mu(\vec{r}_\perp)}{\partial y} - \vec{e}_y\frac{\partial\psi^{TE}_\mu(\vec{r}_\perp)}{\partial x}\right] \\ & \otimes \left[\vec{e}_x\frac{\partial\psi^{TE}_\mu(\vec{r}\,'_\perp)}{\partial y'} - \vec{e}_y\frac{\partial\psi^{TE}_\mu(\vec{r}\,'_\perp)}{\partial x'}\right] \\ & + \frac{2\pi i}{\omega}\sum_\nu \exp\left\{i\left[\frac{\omega}{c} - \frac{c(k^{TM}_\perp)^2_\nu}{2\omega}\right]|z - z'|\right\} \\ & \times \left[\vec{e}_x\frac{\partial\psi^{TM}_\nu(\vec{r}_\perp)}{\partial x} + \vec{e}_y\frac{\partial\psi^{TM}_\nu(\vec{r}_\perp)}{\partial y}\right] \\ & \otimes \left[\vec{e}_x\frac{\partial\psi^{TM}_\nu(\vec{r}\,'_\perp)}{\partial x'} + \vec{e}_y\frac{\partial\psi^{TM}_\nu(\vec{r}\,'_\perp)}{\partial y'}\right] \ , \end{aligned} \qquad (14)$$

Here symbol $\otimes$ denotes the direct product of vectors. The waveguide functions, ψ^{TE} and ψ^{TM}, are the solutions of the Helmholtz equation:

$$\vec{\nabla}^2_\perp\psi + k^2_\perp\psi = 0 \ , \qquad (15)$$

with the boundary conditions

$$\vec{n}\cdot\vec{\nabla}\psi^{TE}|_S = 0 \ , \quad \psi^{TM}|_S = 0 \ , \qquad (16)$$

and the normalization condition

$$\int |\vec{\nabla}\psi|^2\,\mathrm{d}\,\vec{r}_\perp = 1 \ . \qquad (17)$$

The β th component of the transverse beam current density, j^β_ω, is connected with the complex

[1] Expression (14) contains only transverse components of $G^{\alpha\beta}_\omega$. In the case of an overmoded waveguide it provides sufficient accuracy for the calculation of the transverse component of the vector potential.

amplitude, $\tilde{j}_1$, as

$$j_\omega^\beta = \frac{1}{c} v^\beta(z) \tilde{j}_1(z,\ \vec{r}_\perp) \exp\left(\mathrm{i}\, k_\mathrm{w} z + \mathrm{i}\,\omega \frac{z}{c}\right) \ . \quad (18)$$

Using relation $\tilde{E}_{x,y} \exp(\mathrm{i}\,\omega z/c) = E_\omega^{x,y}$, and equations (2), (14), (13) and (18), we write the expression for the effective potential of the interaction between the particle and the radiated electromagnetic wave:

$$\begin{aligned} U_\mathrm{i} = & -\frac{\pi\,\mathrm{i}}{2c} e\theta_\mathrm{s}^2 \int_0^z \mathrm{d}\, z' \int \mathrm{d}\, \vec{r}'_\perp \tilde{j}_1(z',\ \vec{r}'_\perp) \\ & \times\ \mathcal{D}\mathcal{D}' \left\{ \sum_\mu \psi_\mu^\mathrm{TE}(\vec{r}_\perp) \psi_\mu^\mathrm{TE}(\vec{r}'_\perp) \right. \\ & \times \exp\left[-\mathrm{i}\, \frac{c(k_\perp^\mathrm{TE})_\mu^2}{2\omega} (z - z') \right] \\ & + \sum_\nu \psi_\nu^\mathrm{TM}(\vec{r}_\perp) \psi_\nu^\mathrm{TM}(\vec{r}'_\perp) \\ & \left. \times \exp\left[-\mathrm{i}\, \frac{c(k_\perp^\mathrm{TM})_\nu^2}{2\omega} (z - z') \right] \right\} \end{aligned} \quad (19)$$

where $\mathcal{D}\mathcal{D}'$ denotes

$$\mathcal{D}\mathcal{D}' = \left(\frac{\partial}{\partial x} + \mathrm{i}\, \frac{\partial}{\partial y} \right) \left(\frac{\partial}{\partial x'} - \mathrm{i}\, \frac{\partial}{\partial y'} \right) \ .$$

The external electromagnetic wave can be expressed in terms of the eigenmodes of the passive waveguide:

$$\begin{aligned} [\vec{e}_x(\tilde{E}_x) + \vec{e}_y(\tilde{E}_y)]_\mathrm{ext} = & \sum_\mu C_\mu^\mathrm{TE} \exp\left[-\mathrm{i}\, \frac{c(k_\perp^\mathrm{TE})_\mu^2 z}{2\omega} \right] \\ & \times \left(\vec{e}_x \frac{\partial \psi_\mu^\mathrm{TE}(\vec{r}_\perp)}{\partial y} - \vec{e}_y \frac{\partial \psi_\mu^\mathrm{TE}(\vec{r}_\perp)}{\partial x} \right) \\ & + \sum_\nu C_\nu^\mathrm{TM} \exp\left[-\mathrm{i}\, \frac{c(k_\perp^\mathrm{TM})_\nu^2 z}{2\omega} \right] \\ & \times \left(\vec{e}_x \frac{\partial \psi_\nu^\mathrm{TM}(\vec{r}_\perp)}{\partial x} + \vec{e}_y \frac{\partial \psi_\nu^\mathrm{TM}(\vec{r}_\perp)}{\partial y} \right) \ , \end{aligned} \quad (20)$$

where coefficients C_μ^TE and C_ν^TM are given by

$$C_\mu^\mathrm{TE} = \int \mathrm{d}\, \vec{r}_\perp \left(\tilde{E}_x(0,\ \vec{r}_\perp) \frac{\partial \psi_\mu^\mathrm{TE}}{\partial y} - \tilde{E}_y(0,\ \vec{r}_\perp) \frac{\partial \psi_\mu^\mathrm{TE}}{\partial x} \right)$$

$$C_\nu^\mathrm{TM} = \int \mathrm{d}\, \vec{r}_\perp \left(\tilde{E}_x(0,\ \vec{r}_\perp) \frac{\partial \psi_\nu^\mathrm{TM}}{\partial x} + \tilde{E}_y(0,\ \vec{r}_\perp) \frac{\partial \psi_\nu^\mathrm{TM}}{\partial y} \right) \ .$$

Total power of the input radiation is expressed in terms of coefficients C_μ^TE and C_ν^TM as

$$W_\mathrm{ext} = \frac{c}{2\pi} \left(\sum_\mu |C_\mu^\mathrm{TE}|^2 + \sum_\nu |C_\nu^\mathrm{TM}|^2 \right) \ . \quad (21)$$

In the case of a single-mode input radiation, we can let the value of the amplitude coefficient C_μ^TE (or, C_ν^TM) be real and positive constant, and write the expression for U_ext as
for TE-mode:

$$\begin{aligned} U_\mathrm{ext}^\mathrm{TE} = & \mathrm{i}\, e\theta_\mathrm{s} \left(\frac{\pi W_\mathrm{ext}}{2c} \right)^{1/2} \left(\frac{\partial \psi_\mu^\mathrm{TE}}{\partial y} - \mathrm{i}\, \frac{\partial \psi_\mu^\mathrm{TE}}{\partial x} \right) \\ & \times \exp\left[-\mathrm{i}\, \frac{c(k_\perp^\mathrm{TE})_\mu^2 z}{2\omega} \right] \ , \end{aligned} \quad (22)$$

for TM-mode:

$$\begin{aligned} U_\mathrm{ext}^\mathrm{TM} = & \mathrm{i}\, e\theta_\mathrm{s} \left(\frac{\pi W_\mathrm{ext}}{2c} \right)^{1/2} \left(\frac{\partial \psi_\nu^\mathrm{TM}}{\partial x} + \mathrm{i}\, \frac{\partial \psi_\nu^\mathrm{TM}}{\partial y} \right) \\ & \times \exp\left[-\mathrm{i}\, \frac{c(k_\perp^\mathrm{TM})_\nu^2 z}{2\omega} \right] \ . \end{aligned} \quad (23)$$

Thus, we have obtained the expressions for effective potential of particle interaction with the radiated wave, U_i, and with the external wave, U_ext. We are interested in the sum of these two contributions:

$$U = U_\mathrm{i} + U_\mathrm{ext} \ . \quad (24)$$

Substituting (24), (19) and (1) into (1), we obtain the integro-differential equation for the first harmonic of the beam current density, $\tilde{j}_1(z, \vec{r}_\perp)$ which can be solved numerically using computer code.

3. Wall resistance effects

All the results, obtained above, refer to the case of perfictly conducting waveguide walls having the conductivity $\sigma \to \infty$. In reality the conductivity

has always finit value. The problem of the exitation of the waveguide having finit conductivity can be solved in the same way as for the perfectly conducting waveguide. The vector and scalar potential are connected with the field components acording to (4). Taking to account the Coulomb gauge for the vector potential (5) we find from Maxwell's equations that the vector potential is subjected to the equation (6). When the waveguide is excited at frequency ω, we have equation (7). The boundary condition for the scalar potential on the waveguide walls is $\phi_\omega = 0$. The boundary conditions for the vector potential, $\vec{A}_\omega$, must provide the boundary conditions for the field. Leontovich,s boundary condition for the field may be written in the form:

$$(\vec{n} \times \vec{A}_\omega)|_{\rm S} = \frac{{\rm i}\, c}{\omega n'} \vec{n} \times (\vec{n} \times (\vec{\nabla} \times \vec{A}_\omega))|_{\rm S} \ . \quad (25)$$

where $\vec{n}$ is the unit vector ($|\vec{n}|^2 = 1$), perpendicular to the surface, and directed inside the waveguide, $n' \simeq \sqrt{{\rm i}\, 4\pi\sigma/\omega}$ is the index of refraction of a metal. We suppose the value of n' to be large complex number, i.e. $|n'|^2 \gg 1$. Finally, we come to the expression for the Green's function which is identical to (10) obtained for the case of perfectly conducting waveguide walls. The only difference is that the eigenvalues and eigenfunctions become to be complex values for the case of waveguide walls with finit conductivity. Scalar functions $\psi^{\rm TE}$ and $\psi^{\rm TM}$, are the solutions of the Helholtz equation

$$\vec{\nabla}_\perp^2 \psi + k_\perp^2 \psi = 0 \ , \quad (26)$$

The eigenfunctions are ortogonal and normalized as

$$\int \vec{\nabla}\psi_\mu \cdot \vec{\nabla}\psi_\nu \, {\rm d}\, \vec{r}_\perp = \delta_{\mu\nu} \ . \quad (27)$$

It is relevant to mention that the orthogonality and normalization conditions are formulated without complex conjugation.

The boundary conditions for $\psi^{\rm TE}$ and $\psi^{\rm TM}$, written down in paraxial approximation, are as follows:

$$[\vec{n} \cdot \vec{\nabla}\psi^{\rm TE} + (\vec{e}_z \times \vec{n}) \cdot \vec{\nabla}\psi^{\rm TM}]|_{\rm S} = -\frac{{\rm i}\, c}{\omega n'} (k_\perp^{\rm TE})^2 \psi^{\rm TE}|_{\rm S} \ ,$$

$$(k_\perp^{\rm TM})^2 \psi^{\rm TM}|_{\rm S} = -\frac{{\rm i}\, \omega}{c n'} [\vec{n} \cdot \vec{\nabla}\psi^{\rm TM} - (\vec{e}_z \times \vec{n}) \cdot \vec{\nabla}\psi^{\rm TE}]|_{\rm S} \ .$$

When $\omega/(|n' k_\perp| c) \ll 1$, these boundary conditions can be written in the form [2]:

$$\vec{n} \cdot \vec{\nabla}\psi^{\rm TE}|_{\rm S} = -\frac{{\rm i}\, c (k_\perp^{\rm TE})^2 \psi^{\rm TE}|_{\rm S}}{\omega n'} + \frac{{\rm i}\, \omega [(\vec{e}_z \times \vec{n}) \cdot \vec{\nabla}]^2 \psi^{\rm TE}|_{\rm S}}{c n' (k_\perp^{\rm TE})^2} \ ,$$

$$(k_\perp^{\rm TM})^2 \psi^{\rm TM}|_{\rm S} = \frac{{\rm i}\, \omega}{c n'} \vec{n} \cdot \vec{\nabla}\psi^{\rm TM}|_{\rm S} \ .$$

In conclusion we should like to stress that described approach for the problem of waveguide exitation is valid for a metallic, or dielectric overmoded waveguide. The only requirement is that of a large value of the refractive index of the waveguide walls which reveals an opportunity to use Leontovich's boundary conditions.

References

[1] H.P. Freund and T.M. Antonsen "Principles of Free electron Lasers" (Capman Hall, New York, 1992)

[2] P.M. Morse and Feshbach, "Methods of Theoretical Physics", Part I (McGraw Hill, New York, 1953)

[3] E.L. Saldin, E.A. Schneidmiller, M.V. Yurkov, Opt.Commun.85(1991)117

[2] It should be stressed that the parameter of the perturbation theory is $\omega/(|n' k_\perp| c)$. The requirement $|n'| \gg 1$ for the overmoded waveguide is necessary, but not sufficient.

Measurement of Space Charge Effects and Laser Pulse Length in the TTF RF Gun using the Phase Scan Technique

S. Schreiber [a], D. Sertore [a,1], P. Michelato [b], M. Ferrario [c], G. von Walter [d], N. Walker [a]

[a] *Deutsches Elektronen-Synchrotron, D–22603 Hamburg, Germany*

[b] *INFN Milano LASA, I–20090 Segrate (MI), Italy*

[c] *INFN Frascati, I–00044 Frascati, Italy*

[d] *RWTH Aachen, D–52056 Aachen, Germany*

The new injector based on a laser driven rf gun at the TESLA Test Facility Linac (TTFL) at DESY is in operation since Dec. 1998 [1]. Its aim is twofold: to provide beam for experiments related to beam dynamics, where high bunch charges of 8 nC are required, and to provide a low emittance beam with reduced charge to drive the free electron laser TTF-FEL. To generate electron beams with high quality, it is important to understand space charge effects, especially in the rf gun. High space charge may lead to an unacceptable emittance growth. This report briefly describes space charge related measurements in the rf gun. Furthermore, a method to measure the laser pulse length with the phase scanning technique is presented.

An important tool to evaluate space charge effects in a laser driven rf gun is the phase scanning technique: the charge transmitted through the gun is measured as a function of relative phase between the gun rf and the laser pulse. The charge is measured with an integrated current transformer (Bergoz, France) directly at the gun exit. The phase and amplitude of the rf pulse in the gun is controlled and stabilized with a low level rf control system based on digital signal processors [2]. It analyses the signal of a pick-up electrode in the gun to perform a feedback and to adjust a feedforward table. This system allows to change consistently the gun phase in steps of 0.5°. The phase stability of the laser is 0.5° as well [3]. The phase scans are performed for various charge densities on the cathode. Charge densities are either changed by varying the laser pulse energy (1 to 8 nC) or by changing the laser spot size on the cathode (r = 1.5 mm or 5 mm).

Figure 1 shows several phase scans for different charge densities. At low charge densities (around 5 nC/cm^2), the phase scan shows a steep rise and a flat top of about 80°. The rise time, as explained later on, reflects the length of the laser pulse. A flat top is expected, since all electrons are accelerated and transmitted through the gun during the first 90° of rf. For high charge densities (above 10 nC/cm^2) a much slower rise of the transmission is observed. This is explained by the screening ef-

[1] on leave from INFN Milano LASA, Italy

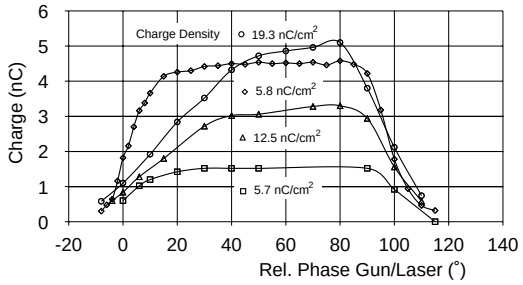

Fig. 1. Phase scans for several charge densities on the cathode.

fect due to space charge: while part of the bunch has already left the cathode, it shields the accelerating field. For small phases, the shielding is strong enough to fully compensate the accelerating field for the residual electrons. The data are in good agreement with beam subamics simulations.

To investigate this further, the charge transmitted through the gun is measured for different accelerating gradients for constant phase, charge, and the charge density. Figure 2 shows the transmitted charge as a function of the accelerating gradient. At 40 MV/m, the full charge of 2 nC

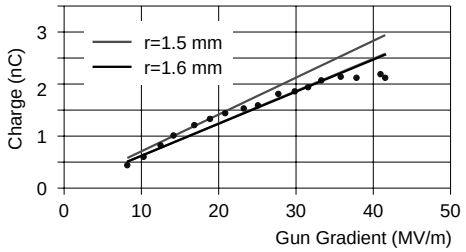

Fig. 2. Transmitted charge for different accelerating gradients in the gun. The lines indicate the space charge limit calculated with Gauss' law for two laser spot radii.

(28 nC/cm^2) is transmitted through the gun. Lowering the field, the screening effect due to space charge take over and reduces the transmitted charge. Figure 2 also shows the space charge limit calculated from Gauss' law for two different radii of the laser spot on the cathode. The spot size radius of the laser was adjusted to 1.5 mm.

Taking the space charge limit in the rf gun into account, the phase scanning technique is also used to evaluate the longitudinal profile of the laser pulse. The zero crossing of the accelerating field acts like a sharp edge: only the part of the bunch which sees acceleration is accelerated to full energy and transmitted through the gun. The shape of the rise in the phase scan plots is just the integral of the longitudinal laser pulse shape. Differentiating the rise yields the longitudinal laser pulse shape as shown in Fig. 3. To confirm the validity of this method, the laser pulse shape was also measured with a streak camera (resolution 2 ps).In Fig. 3, the measured profile is overlaid to the differentiated rise of the phase scan plot. The agreement obtained is reasonable. Integrating the profile measured with the streak camera also matches well with the recorded rise of the phase scan plot. In this example, the laser pulse has a length of 8.0 $\pm$ 1 ps.

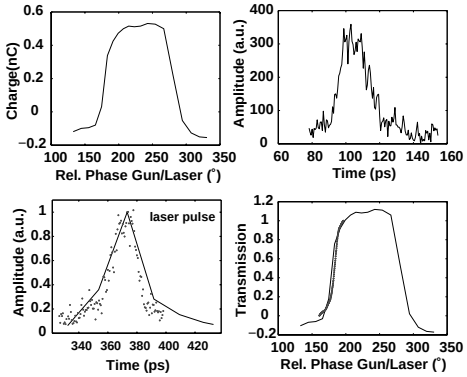

Fig. 3. The rise of the phase scan plot (upper left) taken at a low charge density is differentiated to obtain the longitudinal shape of the laser pulse (lower left). The shape is compared to the profile taken with a streak camera (dots). The integration of the streak camera laser profile (upper right) fits well with the rise of the phase scan plot (lower right, dotted line).

We like to thank M. Bernard and B. Leblond for their help in setting up the streak camera provides to us by LAL, Orsay, France.

References

[1] S. Schreiber, "First Running Experience with the RF Gun based Injector of the TESLA Test Facility Linac", this conference.

[2] G. v. Walter, Diploma Thesis, RWTH Aachen, in preparation.

[3] S. Schreiber et al., "Running Experience with the Laser System for the RF Gun based Injector at the TESLA Test Facility Linac", this conference.

Transverse Emittance Measurements in the TTF Injector

H. Edwards, M. Castellano, L. Catani, A. Cianchi, M. Ferrario, M. Geitz,
S. Schreiber, D. Sertore, F. Stephan
For the TESLA Collaboration

1 Introduction

The transverse emittance of the beam delivered to the TESLA Test Facility FEL is critical to its performance. A laser driven RF gun of FNAL design has been installed in the TESLA Test Facility injector. Initial emittance measurements in the injector of a 1 nC bunch beam have been carried out using both the slit method and quad scan tomography technique. Results are compared with those of an identical injector system at FNAL and with calculations—simulations.

2 Hardware

The injector consists of a 1.6 cell 1.3GHz normal conducting gun, a 9 cell superconducting TESLA cavity, a magnetic chicane, and beam line and quads to match into the TTF Linac cryo module structures. The overall injector length is about 10 m. The start of the 1 m Tesla cavity is located at 1.3m from the gun cathode and emittance is measured at 3.6m where the slits are located. The beam image is monitored 38 cm downstream. The beam image for the tomography scan is recorded at 5.8 m while adjusting a quad-doublet at 3.8 m.

Gun operating parameters are: gradient, 35MV/m on the cathode; launch phase relative to bunch center, 50 deg; laser spot diameter, 3mm; laser pulse length sigma, 7ps. Primary and secondary solenoids at the gun cathode and exit regions provide beam focusing and optimize the emittance. The 9 cell cavity was operated at 11-12 MV/m on crest. Typically total energy after the gun and 9 cell cavity is about 4.5 and 16 MeV respectively.

Adjustment of the slit is obtained by means of a linear actuator. Additional rotational alignment is provided about the horizontal and vertical axes. Linear motion is 150 mm (5 micron/step) to allow for additional screens; rotational motion is 3.6 micro-radians/step.

View screen/slit actuators, video camera switching and image recording is controlled by the optical diagnostic control system (ODCS), a complete set of Labview tools. A new set of Vi's has been integrated into ODCS to perform online the emittance measurement with the slit technique. Slit alignment is performed by looking at the beamlet images and profiles while the slits are moved. Online emittance calculation is performed starting from the profile in two steps. The first is to obtain a rough estimate of the peak center, width and height. The operator selects the number of peaks that can be seen and a threshold discrimination value to reject any background spikes. When a result in good agreement with the data has been achieved the operator can continue and ask for a multi-gaussian fit which is then used to calculate the phase space and a plot of the beam ellipse displayed on the control panel.

3 Emittance Measurements

The transverse rms normalized emittance is defined in terms of the Lorentz γ and the variances of x and x' by $\epsilon_{\rm rms} = \gamma\sqrt{< x^2 >< x'^2 > - < xx' >}$.

Slit Measurements A tantalum mask with horizontal slits is used to measure the vertical beam emittance as a function of the gun solenoid magnetic fields for 10 and 20 beam bunches per pulse. Beamlets are imaged on a downstream OTR screen so that the spot size and the divergence of the beam at the position of the slit mask can be determined from knowledge of the slit spacing (1.05 mm±1%) and slit to OTR distance (385 ± 10 mm).

The OTR video image is analyzed in detail offline and background and X-rays removed. In nearly all measured cases three slits show up in the vertical projection and can be fit with gaussians and a constant background. The fit describes the data well and emittance is calculated taking into account the resolution of the frame grabber [$(60 \pm 3)\mu$m/pixel in y]. Measurements have been obtained for three solenoid settings with the ratio of primary to secondary peak fields held constant at 1.04. Peak primary B_z fields were 0.077, 0.079, 0.083 T (current Prim/Sec 158/86, 165/90, 176/96 A). Four independent measurements were made for each setting at 20 bunches and two at 10 bunches.

Five sources of systematic error are taken into account. The most important contribution comes from the fact that only three slits are illuminated and the unmasked spot was not used in the analysis. For only one measurement a tiny fourth spot is visible which if taken into account increases σ_y^2 by 13%. All σ_y^2 data has been increased by this amount, with an uncertainty of ±13% as well. Other systematic errors are: pixel size (5%), distance slit to screen (3%), slit spacing (1%), slit width (negligible). The resultant systematic error in the emittance is 9%. The slit emittance results are given in Fig. 1

where systematic and statistical errors have been added in quadrature. Tomography results from the next section are also shown.

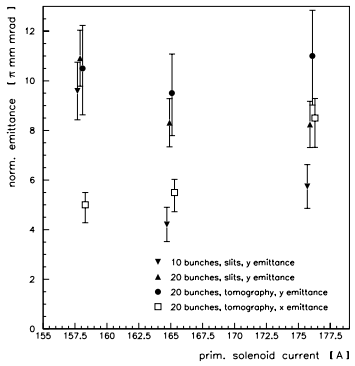

Figure 1: Measured emittances with slit and tomography method as a function of solenoid current and bunches per pulse train. Identical solenoid settings are slightly displaced horizontally.

Phase Space Tomography An experimental determination of the entire transverse phase space distribution can be accomplished by applying a quadrupole scan in combination with tomographic image reconstruction techniques [1, 2]. For this purpose, a set of quadrupoles is used to rotate the phase space distribution in well-defined steps between the reconstruction point z_0 in front of the quadrupoles and the measurement point z_1 behind the quadrupoles. Under the assumption of linear beam transfer, the phase space rotation angle ϕ is determined by the beam transfer matrix. The beam spot OTR profiles recorded at various rotation angles ϕ yield the so-called Radon transformation [3] $p_{z_1,\phi}(x)$ and $q_{z_1,\phi}(y)$ in the x- and y-plane respectively. The Radon transform is inverted by a filtered backprojection algorithm [4] yielding the reconstructed phase space distribution.

Linearized space charge forces are implemented into the beam transfer calculations. Defocusing quadrupole kicks of strength $k_{x,y} = \frac{2Nr_e}{\sqrt{2\pi}} \frac{1}{\sigma_{x,y}(\sigma_x+\sigma_y)\sigma_z\gamma^3}$ are included in the transfer matrix formalism every millimeter of the lattice. N denotes the number of charges and r_e the classical electron radius. The beam parameters for space charge affected beams are determined by a self-consistency method: the beam transfer is computed for a set of assumed beam parameters (ϵ, α, β, σ_z, N) yielding reconstructed transverse beam parameters (ϵ^R, α^R, β^R). The initial parameters are varied until the initial and reconstructed parameters match. Fig. 2 shows the phase space ellipse as measured by the slit and by tomography.

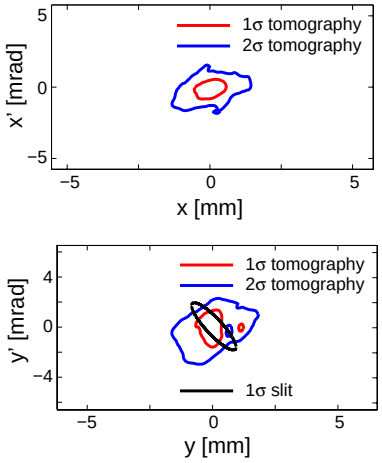

Figure 2: Contour plot of the charge distributions reconstructed by phase space tomography and the reconstructed phase space from the slit method.

4 Comparison and Conclusions

Emittances of 4-10 mm-mr have been measured. For y with 20 bunches there is consistancy between methods. Inhomogeneity in the laser can result in differences in x and y planes. One would expect larger emittances with more bunches or with the tomographic technique if there are changes bunch to bunch or over the time needed to carry out the tomography scan. Measurements carried out at FNAL (reported this conference) yield similar results. Parmella calculations yield ≈10 for these solenoid settings but predict lower possible emittances at the same total focal strength but with a larger primary to secondary ratio. Further measurements will be necessary to see if good quality beam can be found in this region.

References

[1] O. R. Sander, G. N. Minerbo, R. A. Jameson and D. D. Chamberlin, Proc. of the Linear Accelerator Conference 1979, 1979.

[2] M. Geitz, Proc.of the Particle Accelerator Conference 1999, 1999.

[3] J. Radon, Berichte der Sächsischen Akademie der Wissenschaften, Leipzig, Math. Phys. Kl. 69 (1917) 262.

[4] F. Natterer, The Mathematics of Computerized Tomography, Teubner, Stuttgart, 1996.

First Running Experience with the RF Gun based Injector of the TESLA Test Facility Linac

S. Schreiber for the TESLA Collaboration,

Deutsches Elektronen-Synchrotron, D–22603 Hamburg, Germany

The TESLA Test Facility (TTF) built by an international collaboration [1] is a test bed situated at DESY to prove that superconducting cavities as proposed for a TeV scale linear e^+e^- collider can be assembled into a linac test string (TTFL), and that accelerating gradients above 15 MV/m are consistently obtainable [2]. In fall 1998, a new injector based on a laser-driven rf gun [3] to generate high bunch charges up to 8 nC with 1 MHz repetition rate was brought into operation. Its aim is to perform various experiments where beam properties have to be as close as possible to the TESLA design: to detect and investigate higher order modes, space charge, and wake field effects. In addition, the new injector is being used for the proof-of-principle experiment of the proposed free electron laser TTF-FEL [4].

A schematic overview of the TTF injector is shown in Fig. 1, further details can be found in [5]. The electron source is a laser-driven 1 1/2-cell

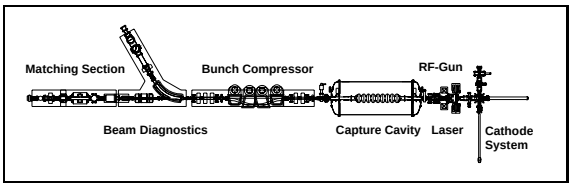

Fig. 1. Schematic overview of the rf gun based TTF injector. The laser system is not shown. The total length of the injector is 12 m.

rf gun operating at 1.3 GHz using a Cs_2Te cathode. The gun has been built and tested in the framework of the TESLA collaboration at the A0 Test Facility at Fermilab [6]. A summary of the rf gun design and typical operating parameters is shown in Tab. 1. A load lock cathode system allows mounting and changing of cathodes while maintaining ultra-high vacuum conditions [7]. The cathode is illuminated by a train of UV laser pulses generated in a mode-locked solid-state laser system synchronized with the rf [8]. An energy up to 50 μJ with a shot-to-shot energy variation of 2 % (rms) is achieved. The UV pulse length measured with a streak camera gives $\sigma_t = 7.1 \pm 0.6$ ps. The system was running more than 2000 h during the last running period. It was available for beam 97 % of the running time [9].

Table 1
Some RF gun design parameters compared to typical operating values during the last runs.

Parameter		Design	Operated
Ave. Gradient	MV/m	35	35 ... 43
Klystron Power	MW	2.2	2.2 ... 3.3
Av. Diss. Power	kW	22	0.11 ... 3.5
Rep. Rate	Hz	10	1 ... 5
RF Pulse Length	μs	800	50 ... 800
Bunch Charge	nC	8	1 ... 8
Bunch Spacing	μs	1	1
Bunch Length	mm	2	2 ... 4

The gun section is followed by a superconducting capture cavity, a bunch compressor, a dispersive arm, and a section to match the beam optics

to the accelerating structures. The capture cavity is identical to a 9-cell TESLA accelerating structure. It boosts the beam energy up to 20 MeV. For some beam experiments, the magnetic chicane bunch compressor is used to compress the bunch length by a factor of 2. Several diagnostic instruments allow to measure basic beam parameters as well as to perform dedicated experiments. The design parameters of the injector are listed in Table 2 together with parameters required for TTF-FEL operation.

Table 2
Injector design parameters for TTFL and TTF-FEL operation.

Parameter		**TTFL**	**FEL**
RF Frequency	GHz	1.3	
Rep. Rate	Hz	10	
Pulse Train Length	μs	800	
Pulse Train Current	mA	8	9
Bunch Frequency	MHz	1	9
Bunch Charge	nC	8	1
Bunch Length (rms)	mm	1	0.8
Emittance, n. x,y	10^{-6} m	20	2
ΔE/E (rms)		$1{\cdot}10^{-3}$	
Injection Energy	MeV	20	

Experimental Results: A field gradient in the rf gun of 35 MV/m is routinely achieved. For some experiments, the gradient was raised to 43 MV/m. In the linac, the rf pulse length is limited to 100 μs and 1 Hz during the run for machine safety reasons, although the gun was conditioned at Fermilab up to 800 μs.

The charge transmission of the gun is linear up to 16 nC for nominal field and a hard edge laser spot size on the cathode of $r = 5$ mm. For charge densities above 20 nC/cm^2 on the cathode, part of the beam is lost due to screening of the acceleration field by space charge [10]. The beam energy has been measured with and without the capture cavity, the results are in agreement with the expectation from the accelerating gradients: 3.8$\pm$0.1 MeV for 35 MV/m (gun only) and 16.5$\pm$0.1 MeV with a capture cavity gradient of 12 MV/m. The energy spread measured using an optical transition radiation screen in the dispersive arm yields $\Delta E/E = 1.9{\cdot}10^{-3}$ (rms).

Two different techniques have been used to measure the emittance [11]: a tomographic reconstruction of the phase space by scanning quadrupoles and a slit system to mask out small bunchlets. From the bunch size and the divergence of the drifting bunchlets the emittance is been reconstructed. Both method use optical transition radiation created on aluminum foils to measure the bunch profiles. Results of both methods agree, an emittance of $(4.2 \pm 0.7) \cdot 10^{-6}$ m for a bunch charge of 1 nC has been achieved.

References

[1] For members of the TESLA collaboration see http://tesla.desy.de/

[2] TESLA-Collaboration, ed. D.A. Edwards, "TESLA Test Facility Linac – Design Report", DESY Print March 1995, TESLA 95-01.

[3] The injector is based on Injector I built by IN2P3/LAL and IN2P3/IPN, Orsay and CEA/DSM DAPNIA, Saclay. Major contributions to the new installation at DESY are from Fermilab, Max Born Inst. Berlin, INFN Milano, DESY, INFN Frascati, INFN/Univ. Roma II, UCLA Dep.of Physics.

[4] "A VUV Free electron Laser at the TESLA Test Facility at DESY – Conceptual Design Report", DESY Print, June 1995, TESLA-FEL 95-03.

[5] S. Schreiber, "The RF-Gun based Injector for the TESLA Test Facility Linac", Proc. of the 6th European Particle Accelerator Conference, Stockholm, Sweden, June 22-26, 1998, p. 1462.

[6] J.-P. Carneiro et al., "First Results of the Fermilab High-Brightness Photo-Injector", in Proc. of the 1999 Particle Acc. Conf., New York, March 1999.

[7] P. Michelato et al., "First Operation of Cesium Telluride Photocathodes in the TTF Injector RF Gun", this conference.

[8] I. Will, A. Liero, S. Schreiber, W. Sandner, "The TTF Photocathode Laser", this conference.

[9] S. Schreiber et al., "Running Experience with the Laser System for the RF Gun based Injector at the Tesla Test Facility Linac", this conference.

[10] S. Schreiber et al., "Measurement of Space Charge Effects and Laser Pulse Length in the TTF RF Gun using the Phase Scan Technique", this conference.

[11] H. Edwards et al., "Measurement of the Transverse Emittance in the TTF Injector", this conference.

Running Experience with the Laser System for the RF Gun based Injector at the TESLA Test Facility Linac

S. Schreiber [a], I. Will [b], D. Sertore [a,1], A. Liero [b], W. Sandner [b]

[a] *Deutsches Elektronen-Synchrotron, D–22603 Hamburg, Germany*

[b] *Max-Born Institut, D–12489 Berlin, Germany*

Abstract

During the run 1998/1999, the new injector based on a laser driven rf gun was brought into operation at the TESLA Test Facility Linac (TTFL) at DESY. A key element of the injector is the laser system to illuminate the rf gun cathode to produce short (ps) electron bunches of high charge (nC). This electron beam is used to perform various experiments for the future TESLA linear collider, and to drive the free electron laser TTF-FEL. The laser design is challenged by the unusual requirement of providing synchronized ps UV pulses in 0.8 ms long trains with ambitious stability requirements. The design was also driven by the requirement to have an operational system with a high reliability. The system is based on a mode locked solid-state (Nd:YLF) pulse train oscillator followed by a linear amplifier chain. In a first phase, a laser pulse rate of 1 MHz within the train has been realized, 2.25 MHz and 9 MHz are in preparation. Performance and running experiences with the laser system during the last TTF run are reported.

1. Introduction

The TESLA Test Facility Linac (TTFL) [1] under operation at DESY uses an rf photoinjector together with a superconducting linac to generate and accelerate an electron beam adequate for the proof-of-principle experiment of the TTF free electron laser (TTF-FEL) [2]. The laser system driving the rf gun is a key element, which determines significantly the quality of most beam parameters, and thus plays a major role in the success of the free electron laser.

Superconducting accelerating structures allow high duty cycles, in the case of TTF 0.8 ms long rf pulses with a repetition rate of 10 Hz. To make use of this, the laser system is challenged by the generation of ms long pulse trains. Since this is an unusual requirement for common laser systems, the development of a novel techniques were required to accomplish this task. Another basic guideline for the design was to realize a robust and reliable system, which fulfills the specified performances routinely during normal running conditions of an FEL user facility. Independently, a second laser system for similar purposes has been built and is in operation at the A0 gun test beamline at Fermilab [3].

[1] on leave from INFN Milano - LASA, I–20090 Segrate (MI), Italy

During the last TTF run from December 1988 to March 1999 the laser system has been continuously operated allowing to evaluate its reliability under realistic conditions. In the following, principle components of the laser system will be described, results of its performance are given followed by a discussion of the overall experience with the system during the run.

2. Description of the laser system

Table 1 gives an overview on the specified parameters of the laser system, Fig. 1 shows an overview of the laser components. A complete description is given in [4].

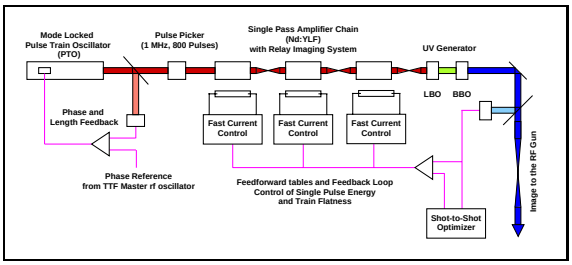

Fig. 1. Schematic overview of the TTF photoinjector laser system.

The main difficulty is to produce a flat and stable train of 800 UV pulses within 0.8 ms, each with an energy of at least 5 μJ. The pulses have to be synchronized within 1 ps with the rf system driving the gun and the linac klystrons. To meet both requirements, an active mode locked pulse train oscillator (PTO) bases on Nd:YLF at a wavelength of 1047 nm was developed. One difference to common oscillators is, that the PTO already amplifies the pulse train to several 10th of W within the train (typically 30 W), which avoids the use of a regenerative amplifier. Mode locking is established by an acousto-optic mode locker driven by a 27 MHz rf signal provided by the TTF master rf oscillator [5]. All relevant rf signals required for linac operation are derived directly from the master oscillator to assure good phase stability between the rf signals. An analog feedback system is used to lock the oscillator to the reference phase. This is done with an additional electro-optic mode locker driven with 1.3 GHz with which a phase stability of better than 0.5° or 1 ps is achieved. The PTO is operated in a pulsed mode pumped with flashlamps. About 1 ms is sufficient for stabilization (see Fig. 2).

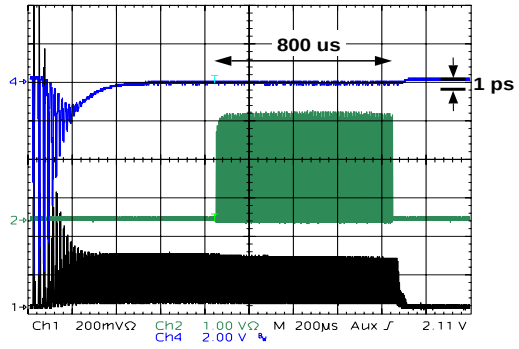

Fig. 2. Oscilloscope trace of the output of the pulse train oscillator (PTO) (trace 1), the phase of the pulses relative to the reference (trace 4), and the pulse train after amplification measured in the green with a fast photodiode (trace 2). Note, that due to the scale (200 μs per div.) individual pulses in the train are not visible. Indicated is the vertical scale of the phase signal corresponding to a phase shift of 0.5° of 1.3 GHz, which corresponds to 1 ps.

Before the amplification process, the 54 MHz pulse train output of the PTO is reduced to the desired train length and number of pulses in the train using a Pockels cell together with a polarizer. For most of the TTF experiments, 1 MHz repetition rate is chosen, were the number of pulses is adjustable from 1 to 800. For future FEL experiments, 2.25 MHz and 9 MHz trains are in preparation.

The amplification to 200 μJ per pulse (thus about 200 mJ per train), is done in a linear single pass amplifier chain. Three amplifiers with an adjustable gain between 8 and 10 are sufficient. A novel feature is the use of programmable power supplies. The flashlamp current is set in steps of 10 μs width predefined feedforward tables. This is essential to obtain a flat pulse train and gives in addition the opportunity for an efficient amplitude feedback system [6].

Since the work function of the Cs_2Te cathode used in the rf gun reaches its maximum at 5 eV [7], the fundamental wavelength has to be converted into the UV. With the two non-linear crystals LBO and BBO a conversion efficiency to 262 nm of 15 to 20 % is achieved. The energy of a UV

Table 1
Basic specifications of the TTF laser system. They are compared to the measured performance during the last run.

Item	Specification	Measured
pulse train	800 pulses spaced by 1 μs	achieved
repetition rate	10 Hz	achieved, run mode 1 Hz
pulse energy	5 μJ (262 nm)	50 μJ (262 nm)
pulse length (262 nm)	2 to 10 ps (sigma)	7.1 $\pm$ 0.6 ps (sigma)
transverse profile	flat-top	achieved
flat-top homogeneity	$\pm$10 %	partially achieved
energy stability	peak-peak	
– train to train	$\leq \pm$ 10 %	$\leq \pm$ 5 %
– pulse to pulse	$\leq \pm$ 10 %	$\leq \pm$ 5 %
synchronization	to reference rf signals	achieved
phase stability	$\leq$ 1 ps rms	$\leq$ 1 ps rms

pulse can be adjusted in wide range up to is 50 μJ, largely sufficient to produce 8 nC electron bunches even with a moderate quantum efficiency of the cathode of 0.5 %.

A relay imaging system generating near flat-top pulses contributes to the homogeneous amplification along the train. A hard edge aperture at the exit of the PTO is relay imaged together with spatial filtering to each amplifier, the frequency conversion stage, and the cathode of the rf-gun. Imaging onto the cathode has also the advantage of a much better pointing stability on the 10 m transfer beamline from the laser to the rf-gun. The laser system is installed in a separate room inside the TTF experimental hall. Air-conditioning provides a stable temperature of $\pm$ 0.5°C. No beam jitter has been observed using a CCD camera near the gun, the pointing jitter is less than 2 μrad. The imaging is done using a telescope with a magnification of 1 to transport the beam into the linac tunnel. A second telescope with a magnification of 10 images the beam onto the cathode. For 8 nC operation, a laser beam diameter of 10 mm is used, for 1 nC operation it is reduced to 3 mm. The mirrors of the transfer line are motorized to allow for remote adjustment of the beam path. The last lens just before the vacuum chamber is used to remotely steer the beam over the cathode in order to well center the beam within a fraction of a mm.

All relevant parts of the laser system are controlled or adjustable via a computer system. It is mainly used to control the operation of the laser system. It is integrated into the TTF control system, so that TTF operators have the possibility to control basic parts of the laser such as switching it on and off, setting flashlamp currents, and the number of pulses in the train. An SPS based system surveys safety relevant parameters like water flow, temperatures, status of power supplies etc. providing a reliable interlock system. The standard TTF timing system is used to provide all necessary triggers.

3. Performance and running experience

The performance of the laser system measured during the last run are typical performances in the sense, that these values have been reached routinely during operation. Table 1 shows the measured performance compared to the specification. Most of the goals have been reached or are even better: the energy per pulse is with 50 μJ (peak performance 100 μJ) largely sufficient to produce an 8 nC beam with the given cathode. The train-to-train energy stability and the pulse to pulse stability within the train (train flatness) is better than 5 % (peak-peak), an rms value of 2 % is being reached averaged over 20 shots. The phase stability is better than 1 ps, the feedback system is working without failures. Figure 2 shows an oscilloscope trace of the phase in respect to the reference phase of the 1.3 GHz rf signal. Also shown is the pulse train output of the PTO and the amplified train after conversion into the green, measured with fast photodiodes.

The laser pulse length in the fundamental wavelength has been measured with a standard autocorrelation technique giving a pulse length of 10 ps (sigma). A streak camera [8] with a resolution of 2 ps has been used to measure the pulse shape in the UV, two examples are shown in Fig. 3. For nominal flashlamp currents averaged over several measurements a pulse length of $\sigma_t = 7.1 \pm 0.6$ ps is obtained. This is within the specified range. However, shorter pulses are required to produce longitudinal flat-top-beams which help to reduce the beam emittance. It was foreseen from the beginning, that the ambitious goal of 2 ps could not be reached in the first phase. At present, an upgrade project is going on with the goal to reduce the pulse length.

As a fast and simple method, the phase scan technique [9] has been used to verify the laser pulse length during the run. In fact, this method revealed lengthening of the laser pulse by a factor of 2 due to a fault in the PTO laser head.

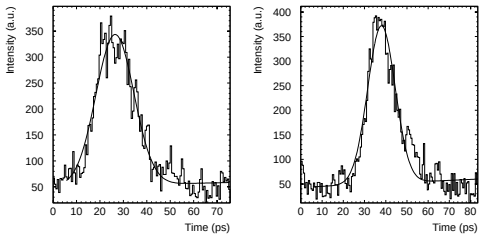

Fig. 3. Two examples of laser pulse shapes measured with a streak camera at 262 nm. The pulse length determined by a fit to a gaussian profile is $\sigma_t = 6.3 \pm 0.6$ ps and 8.0 $\pm$ 0.1 ps resp.

The UV transverse beam profile during the last run was not yet satisfactory. Inhomogeneities induced by the frequency conversion process are larger than specified. Effort is going on to improve the quality, using an additional spatial filter in the UV beam line and to reduce the focussing into the frequency conversion crystals.

The laser has been continuously operated during the run from mid December 1998 to mid March 1999 (except last week 1998) on a 24 h/day bases. The total up-time exceeded 2000 h or $8 \cdot 10^6$ shots running at 1 Hz. The total uptime was 99 % of the running time, the laser was available for beam 97 % of the time. Besides routine maintenance like replacing flashlamps, no major failure of the system occurred, however, the complete PTO laser head was replaced to achieve the anticipated pulse length. Replacing major components is easily possible, because a copy of the laser system is in operation at MBI used for further developments.

4. Conclusion

In general, the first running period with the laser system under realistic conditions was a success. The availability during the 2000 h was an impressive 97 % running within its specification. This shows, the importance of a robust and reliable design of lasers intended to be used in user facilities. Also the computer controlled operation of the laser and its integration in the TTF control system is essential for a successful operation. Further long term tests have to follow, especially running with higher repetition rates.

This work was done within a cooperation between DESY, Hamburg and the Max-Born-Institut, Berlin.

5. Acknowledgement

We like to thank K. Rehlich, O. Hensler, and A. Agababyan for integrating the laser into the TTF control system, and M. Staack for his work on the laser interlock system.

References

[1] TESLA-Collaboration, ed. D.A. Edwards, "TESLA Test Facility Linac – Design Report", DESY Print March 1995, TESLA 95-01.

[2] "A VUV Free electron Laser at the TESLA Test Facility at DESY – Conceptual Design Report", DESY Print, June 1995, TESLA-FEL 95-03.

[3] A. R. Fry, M. J. Fitch, A. C. Melissinos, B. D. Taylor, "Laser System for a High Duty Cycle Photoinjector", Nucl. Instr. and Meth. A430 (1999) 180-188.

[4] I. Will, A. Liero, S. Schreiber, W. Sandner, "The TTF Photocathode Laser", this conference.

[5] Composants Quartz & Electronique, F–92391 Villeneuve-la-Garenne Cedex, France.

[6] I. Will, A. Liero, D. Mertins, W. Sandner, "Feedback-stabilized Nd:YLF amplifier system for generation of picosecond pulse trains of an exactly rectangular envelope", Journal of Quantum Electronics 34 (1998), 2020-2029.

[7] E. Taft, L. Apker, J. Opt. Soc. Am., 43 (1953) 81.

[8] ARP Streak Camera, now Photonetics GmbH, D-77694 Kehl, Germany.

[9] S. Schreiber et al., "Measurement of Space Charge Effects and Laser Pulse Length in the TTF RF Gun using the Phase Scan Technique", this conference.

First Operation of Cesium Telluride Photocathodes in the TTF Injector RF Gun

D. Sertore, S. Schreiber[a], K. Floettmann[a], F. Stephan[a], K. Zapfe[a], P. Michelato[b]

DESY, Hamburg, Germany on leave from INFN Milano-LASA

[a)] DESY, Hamburg, Germany

[b)] INFN Milano – LASA, Via F.lli Cervi 201, 20090 Segrate (Milano), Italy

Abstract

During the run 1998/1999 a new injector based on a laser driven RF gun was brought in operation at the TESLA Test Facility (TTF) linac at DESY, in order to produce the beam structure and quality required either by TeV collider and SASE FEL experiments. High quantum efficiency cesium telluride photocathodes, prepared at Milano and transferred to DESY, have been successfully operated in the RF gun. A bunch charge of 50 nC, only limited by space charge effects, was achieved. The photocathodes have shown an operative lifetime of several months. A new cathode surface finishing has showed a promising decrease of the photocathode dark current. Measurements of dark current, quantum efficiency and lifetime are reported.

1. Introduction

In the fall 1998 the Injector II based on the laser driven FNAL RF gun was installed at TTF in DESY, in order to produce the beam structure and quality required either by TeV collider and SASE FEL experiments. To reduce the requirements for the laser and to satisfy the electron beam structure and quality [1], a cathode with high quantum efficiency, low thermal emittance and fast response time is required. Moreover, the linac operation asks for a lifetime of the electron source in the order of months. The cathode selected for the Injector II operation is cesium telluride [2]. It is illuminated by the 4th harmonic of a Nd:YLF laser whose pulse length is σ = 7 ps [3]. The cathode preparation chamber is independent from the gun loading system and a UHV transport device allows to transfer the cathodes from one system to the other. In our case, cathodes are produced at Milano while the gun operates at DESY. Up to now two sets of cathode are prepared and transported to DESY: in June and in December 1998. In July 1998, one blank cathode was used for conditioning the DESY RF Gun and in August, a Cs_2Te cathode replaced it. In November 1998, a second blank was used for the FNAL gun conditioning. In December the second photocathode was installed into the gun and used for operation until mid March, a second set of cathodes was transported to DESY consisting of two photocathodes, one blank and a blank with an UV scintillator. One of the photocathodes was tested in the gun in March 1999 at the end of the run.

In this paper we report the results obtained so far with cathode operation at DESY. In the following section, the cathode preparation process is described. We then report the results about dark current and its reduction with a new surface polishing. In the last section, a discussion on the photoemissive and lifetime performance of the photocathode during the transport and the gun operation is presented.

2. Cathode preparation

The photoemissive material consists of thin layers of Tellurium and Cesium deposited on a Molybdenum substrate under UHV conditions. They react to produce Cs_2Te. This material has an energy gap of 3.2 eV and an electron affinity of 0.5 eV [4]. For these reasons, it is blind to visible radiation and UV light is required for photoemission. The Milano group has studied the procedure for the cathode preparation in the last years [5] applying also surface science techniques [6].

The developed recipe is based on a first evaporation of 10 nm of Tellurium on a substrate heated at 120 °C. Cesium is then evaporated with a rate of 1 nm/min while monitoring the cathode quantum efficiency (QE) with a mercury lamp, selecting the 254 nm line. When the QE is at maximum, the evaporation is stopped and the substrate is cooled down to room temperature. The final photoemissive layer thickness is of the order of some tens of nanometers. The final QE is routinely in the range of 8-10 %.

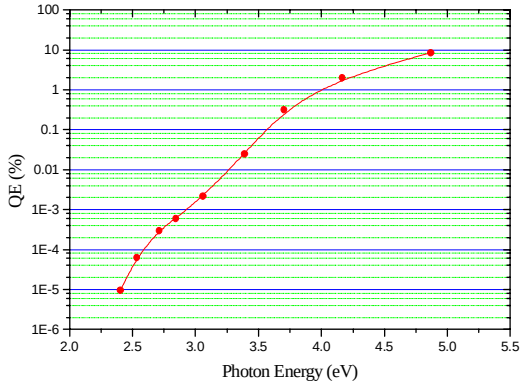

Fig. 1. Typical cathode spectral response. The UV laser light used has a photon energy of 4.7 eV.

The standard cathode characterization consists of a spectral response and a QE scan in order to check the uniformity of the cathode. Fig. 1 shows a typical spectral response of the cathode. The drop of the QE at long wavelengths is due to the physical properties of Cesium Telluride as mentioned at the beginning of this section. The absence of a sharp edge at long wavelengths was explained as due to the presence of more than one phase of the Cs_2Te compound [7]. A plateau is reached at E=5.0 eV close to the 4^{th} harmonic of Nd:YLF (4.7 eV). A beam steering system scans the cathode area by moving a UV light beam from a Hg lamp. The photocurrent emitted from the cathode is collected with an anode placed right in front of the cathode itself. The uniformity is a few percent with respect to the max QE over the whole cathode area (Fig. 2).

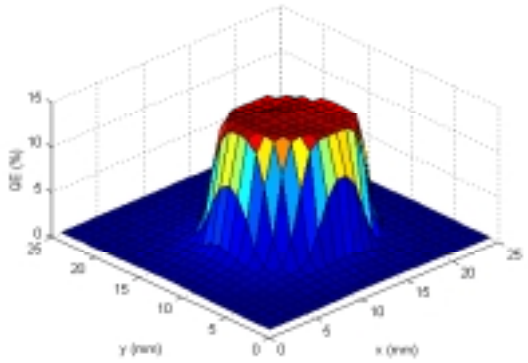

Fig. 2. Distribution of the quantum efficiency over the cathode area.

3. Dark current

The operation of the cathode in the gun exposes the cathode itself to a very high electric field, up to 50 MV/m. In these conditions, the field emission plays an important role. The current density due to field emission is given by the Fowler-Nordheim relation [8]

$$j \propto (\beta \cdot E)^{5/2} \cdot \exp\left(-\frac{B}{\beta \cdot E}\right)$$

where E is the amplitude of the electric field, β is an enhancement factor due to the geometry of the source and B is a material dependent parameter. The sources of dark current are usually tips or needles on the surfaces exposed to the electric field that, due to their geometry, cause an increase of the β parameter. Part of the electrons produced in this way is then accelerated along the linac becoming a source of dark current.

The first test of a Mo substrate exposed to the high field of the gun was done in the summer 1998. The current was collected over the RF pulse with a Faraday Cup. After this measurement, we tested a coated substrate. The results are shown in Fig. 3.

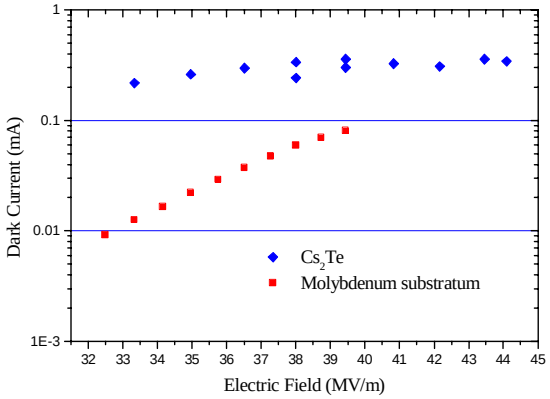

Fig. 3. Dark current from an uncoated and coated substrate with rough surface finishing measured in the gun test stand.

High dark current values were observed in the first operation of the new Mo substrate in the gun. Its reduction to the values shown in Fig. 3 are due to gun conditioning. The coated substrate showed always higher dark current values, probably related to the cesium telluride.Since both substrate surfaces were finished with a tooling machine, they were not mirror-like and an inspection with an optical revealed deep scratches on the surface. For these reasons, a second set of cathodes was prepared with a better surface polishing in order to minimize the surface irregularities. We used diamond grinding powder with a size down to 50 nm. The final aspect of the surface was mirror like. The first cathode with this new surface finishing and a Cs_2Te coating layer was tested in the gun in March 1999 for one week of continuos operation. A significant reduction of the dark current was achieved. The comparison between the

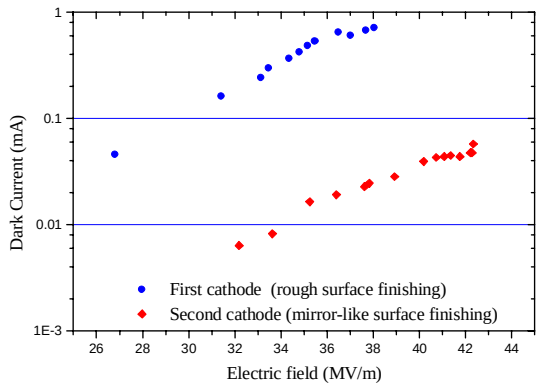

Fig. 4. Dark current measurements in respect to the different surface finishing of a coated substrate.

two types of cathodes is shown in Fig. 4. The new surface finished cathode had more than one order of magnitude less dark current than the old type cathode.

The cathode dark current was measured again at the end of July 1999, when the gun was brought back in operation. We measured a dark current value of 100 μA at 35 MV/m to be compared with the previous value of 16 μA. A significant drop of the QE was also measured that is reported in the following section.

4. QE and lifetime

Cathodes produced at Milano are transported under UHV condition at DESY with a dedicated transport system[9]. This procedure is necessary due to the high sensitivity of these photocathodes to gas exposition [10]. As an example, Fig. 5 shows the effects of exposition to oxygen on the QE. In the following, the influence of the cathode transport system on the QE degradation and the cathode performance when used in the RF gun are discussed.

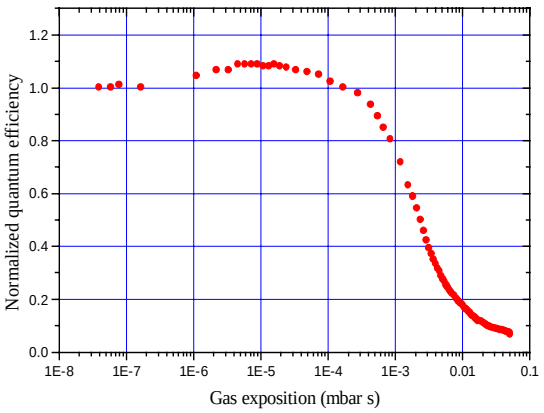

Fig. 5. Cathode sensitivity to oxygen exposition.

To evaluate the effect on the cathode QE due to the transportation, we measured the QE just before leaving Milano and when arriving at DESY. During the travel of about 24 hours, the pumping system of the transportation chamber was powered by a battery through a DC/DC converter and the vacuum was kept in the 10^{-10} mbar range. The measurements show no QE degradation during transportation. The reliability of the system was confirmed with the transportation of the second cathode set.

During the run from December ’98 to March ‘99, we used a cathode with a rough surface finishing. Only at the end of the run, we tested one cathode with the new surface polishing.

The first cathode used in the injector had a high dark current as mentioned in the previous section. We measured from time to time the charge vs. laser energy response. A typical set of data is shown in Fig. 6.

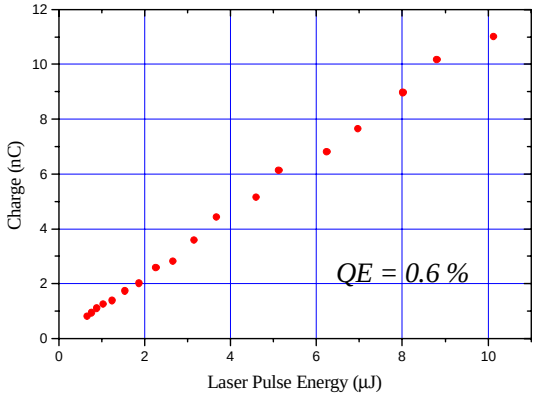

Fig. 6. Response of the Cs2Te cathode in the Rf gun as a function of laser pulse energy.

The corresponding QE is 0.6 % far below the value of 6 % measured in June ‘98 but stable along the whole run. Electron bunches of 1 and 8 nC were routinely produced. Up to 30 bunches (1 MHz repetition rate) per train were used during the run and no saturation effect in the extracted charge was observed. Fig. 7 shows an oscilloscope trace of the charge pulse train measured with integrated current transformers installed along the injector beam line.

At the end of the run, the cathode with the new surface finishing was tested in the gun. The QE after the production was 10 % with uniformity of 5 % over the whole cathode surface, the cathode remained three months in the transport system, mid March it was installed into the gun. We have already reported about the dark current performance in the dedicated section. Fig. 8 shows the charge measured in the gun for different laser pulse energies. The dependence between charge and pulse energy is linear up to 16 nC.

From the slope, the evaluated QE value is 5.6 %, a factor of ten larger with respect to the previous cathode. A saturation effect appeared at high laser pulse energies as

expected, because of the build-up of space charge screening due to the high charge density on the cathode surface. A detailed discussion on this subject is reported at this conference [11]. The maximum charge extracted from the gun was 50 nC to be compared with 0.3 μC emitted from the cathode, assuming constant QE.

This cathode was measured again in July 1999 after 5 months of storage in the RF gun.

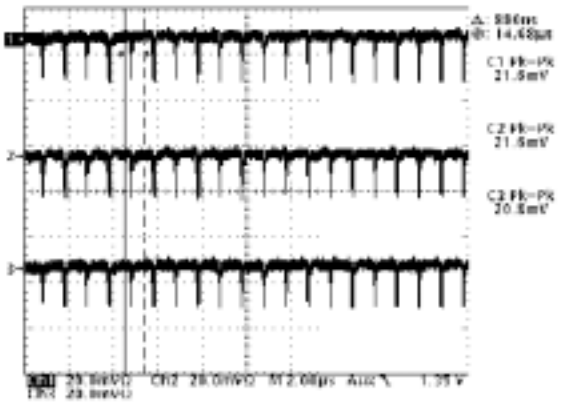

Fig. 7. Charge along the bunch train measured in different locations in the injector.

The QE was 0.6 %, a factor of 10 lower than in March. During this period, the pressure at the pump near the gun was stable at $3.5 \cdot 10^{-11}$ mbar and, since the gun has never been baked, we expect a water partial pressure of some 10^{-10} mbar in the cathode region. Therefore, the cathode has been exposed to some 10^{-3} mbar·s of water. Since the expected effect of water is at least comparable to that of oxygen, the measured QE drop by a factor of 10 is consistent with the experimental data shown in Fig. 5.

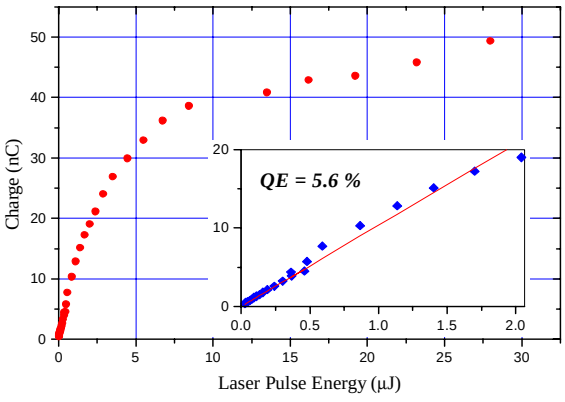

Fig. 8. Charge vs. laser pulse energy for the cathode which has the mirror-like surface finishing. In the insert, the linear part at low pulse energy is zoomed.

5. Conclusion

Transportation and operation of Cesium Telluride photocathodes in the TTF injector was successfully commissioned during the run December '98 to March '99. Cathodes were transported from Milano to DESY without degradation of quantum efficiency. High dark current and low QE values were measured on a six months old photocathode with a rough surface finishing. However, a significant improvement is attained with a fresh cathode, which has a mirror-like substrate finishing. The dark current was a factor of 10 higher. Nevertheless, after five months storage, the QE dropped by a factor of 10, presumably due to water in the gun, while the dark current increased only by a factor of 6. Studies are in progress in order to investigate if QE drop and dark current are related. Moreover, new types of photocathodes will be tested in the RF gun in the next months, prepared with new recipes, which include Potassium. Has been demonstrated [12] that these cathodes are less sensitive to gas exposition while maintaining high quantum efficiency.

The charge delivered over 30 bunches at 1 MHz repetition rate was not limited by saturation effect on the cathode itself. The maximum charge extracted from the gun was 50 nC well above the requirements for TTF.

6. References

1 S. Schreiber, 'First operation of TTF Injector II', PAC 99, New York (USA)

2 D. Sertore, P. Michelato, C. Pagani, A. di Bona, S. Valeri, NIM A **393** (1997), 464

3 S. Schreiber, I. Will, D. Sertore, A. Liero, W. Sandner, 'Running Experience with the Laser System for the RF Gun based Injector at the Tesla Test Facility Linac', this conference.

4 E. Taft and L. Apker, J. Opt. Soc. Am **43** (1953), 81

5 A. di Bona, F. Sabary, S. Valeri, P. Michelato, D. Sertore ,G. Suberlucq, J. Appl. Phys. **80**(1996), 3024

6 A, di Bona et al., EPAC 96, Barcelona (Spain), 1475

7 R. A. Powell, W.E. Spicer, G. B. Fisher and P. Gregory, Phys. Rev. B **8** (1973), 3987.

8 J. W. Wang, 'RF Properties of Periodic Accelereting Structures for Linear Colliders', SLAC-Report-339.

9 P. Michelato, D. Sertore, and C. Gesmundo, 'High quantum efficiency preparation system for TTF Injector II', this conference.

10 P. Michelato et al. EPAC 96, Barcelona (Spain), 1510

11 S. Schreiber, D. Sertore, P. Michelato, M. Ferrario, G. von Walter and N. Walter, 'Measurement of Space Charge Effects and Laser Pulse Length in the TTF RF Gun using the Phase Scan Technique', this conference.

12 D. Bisero, G. J. Ernst, J.W.J. Verschuur, B.M. van Oerle and W. J. Witteman, Appl. Phys. Lett. **69** (1996) 3641

Development of Photon Beam Diagnostics for VUV Radiation from a SASE FEL

R. Treusch*, T. Lokajczyk, W. Xu†, U. Jastrow, U. Hahn, L. Bittner and J. Feldhaus
HASYLAB at DESY, Notkestr.85, D-22603 Hamburg, Germany
(September 13, 1999)

For the proof-of-principle experiment of self-amplified spontaneous emission (SASE) at short wavelengths on the VUV FEL at DESY a multi-facetted photon beam diagnostics experiment has been developed employing new detection concepts to measure all SASE specific properties on a single pulse basis. The present setup includes instrumentation for the measurement of the energy and the angular and spectral distribution of individual photon pulses. Different types of photon detectors such as PtSi-photodiodes and fast thermoelectric detectors based on YBaCuO-films are used to cover some five orders of magnitude of intensity from the level of spontaneous emission to FEL radiation at saturation. A 1 m normal incidence monochromator in combination with a fast intensified CCD camera allows to select single photon pulses and to record the full spectrum at high resolution to resolve the fine structure due to the start-up from noise.

PACS: 41.60.Cr, 42.60.Jf
Keywords: SASE, Free Electron Laser, X-ray laser, VUV, photon beam characterisation, detectors

I. INTRODUCTION

In 1995 DESY proposed to make use of the unique electron beam properties of the TESLA Test Facility (TTF) and to construct a VUV FEL based on self-amplification of spontaneous emission (SASE)[1]. Since the initial work of Kondratenko et al.[2,3], Bonifacio et al.[4] and Pellegrini[5], the SASE theory has been elaborated for short wavelength radiation down to 0.1 nm ([6,7] and references therein). These calculations serve as a sound basis for the experimental verification of the SASE principle. For given electron beam and undulator parameters they predict the gain, the photon beam profile and the SASE-typical fine-structure in the temporal and energy distribution which is caused by the startup from noise[8].

*Corresponding author. Phone: +49 40 8998 2693; Fax: +49 40 8998 4475; e-mail: rolf.treusch@desy.de
†present address: Institute of High Energy Physics, Beijing 100039, China

II. EXPERIMENTAL SETUP

The first phase of the DESY project is considered a proof-of-principle experiment for SASE at VUV wavelengths. For the complete characterisation of the photon beam a multi-facetted experiment has been designed (Fig. 1), providing all the instrumentation necessary to measure the photon pulse intensity and its angular, spectral and temporal distribution. Due to the unique properties of the VUV FEL beam, particularly the extremely high power, the short pulse length and the unusual pulse timing (Table I), new concepts have been developed to measure the SASE specific properties on a single pulse basis. The present part of the experiment required for the initial commissioning and characterisation of the FEL has been designed, constructed and installed by HASYLAB. It comprises all the components shown in Fig. 1 except the left-hand branch (10) (looking downstream) and the very last little chamber in the straight direction which will be added later for a regenerative amplifier FEL experiment[9].

Due to the strong absorption of VUV radiation by any material, all devices for beam diagnostics are operated under ultra-high-vacuum (UHV) conditions, and no windows can be used to separate the diagnostics from the undulator and the accelerator vacuum.

	Energy	
	Minimum	**Maximum**
Electron Beam Properties:		
Energy [MeV]	230	390
Bunch Length (rms) [μm]	240 ≡ 800 fs	
Minimum Bunch Separation [ns]	111	
Max. No. of Bunches per Macropulse	7200	
Macropulse Repetition Rate [Hz]	10	
Undulator Properties:		
Length [m]	13.5	
Magnetic Gap [mm]	12	
Undulator Period [mm]	27.3	
Peak Magnetic Field [T]	0.497	
Photon Beam Properties:		
Energy [eV]	10.2	29.3
Wavelength [nm]	121.7	42.3
Spectral Bandwidth (rms) [%]	0.46	0.28
Pulse Length (rms) [fs]	564	
Photons per Bunch	2×10^{14}	1.5×10^{14}
Peak Power [GW]	0.23	0.5
Average Power (at 72000 pulses/s) [W]	23.5	51.1
Energy/Pulse [μJ]	325	707

TABLE I. *Parameters of the TTF Phase 1 VUV FEL at DESY. Photon intensities and power are saturation values calculated for a normalized electron beam emittance of 2π mm mrad (rms) and an electron energy spread of 500keV (rms). Saturation is expected only for long photon wavelengths.*

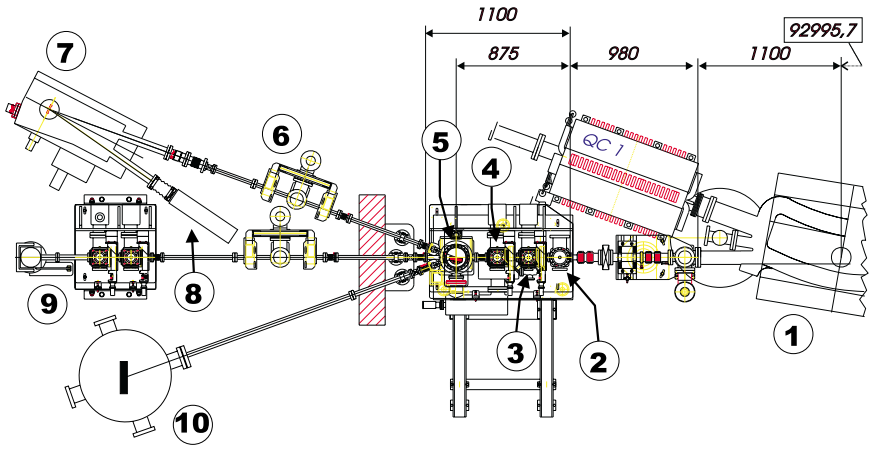

FIG. 1. *Layout of the experimental area for photon beam diagnostics.* **1:** *bending magnet to deflect the electron beam,* **2:** *alignment laser,* **3:** *aperture unit,* **4:** *detector unit,* **5:** *deflecting mirror,* **6:** *Titanium sublimation pump + ion pump unit,* **7:** *1 m normal incidence monochromator,* **8:** *CCD-camera,* **9:** *second chamber with aperture/detector unit and focusing mirror (optional),* **10:** *beamline for autocorrelation experiments and radiation damage investigations (schematic drawing)*

Therefore all components have been cleaned appropriately and assembled under cleanroom conditions to avoid dust particles which could migrate to the accelerator cavities. In addition the experiment is fully remote controlled because the radiation background in the accelerator tunnel prevents access during operation.

An external HeNe-laser, coupled in through a Suprasil (fused silica) viewport (Fig. 1, No. 2), is used to pre-align optical and other diagnostics components. A set of apertures (Fig. 1, No. 3) attached to a water cooled frame can be scanned across the beam profile and defines the photon beam cross section impinging on the detectors (No. 4) and the optical components downstream. A second set of apertures and detectors (No. 9) is available further downstream in the straight forward direction and can be used to determine the FEL beam direction and to align the HeNe-Laser. For the commissioning phase this second aperture/detector unit has actually been moved out of the direct beam into the left-hand branch in order to protect it from the hard γ radiation due to beam loss in the accelerator and from bremsstrahlung produced in the long undulator. Later this second set of apertures and detectors will be moved back into the position shown in Figure 1 and additional equipment will be added in the left-hand beamline (No. 10).

To cope with beam intensities varying over roughly five orders of magnitude, different types of detectors have been mounted on a cooled frame just behind the apertures (Fig. 2), including simple, electrically insulated metal plates and thin tungsten wires (50 μm diameter), PtSi-photodiodes[10] and thermopiles[11,12] based on the "Seebeck-Effect" of YBaCuO high-T_c superconductors (HTSCs)[12].

PtSi-photodiodes were preferred to Si- or GaAsP-diodes due to their radiation hardness. For $\lambda \leq 150$ nm, Si- and GaAsP-photodiodes deteriorate already at low exposure doses of several mJ/cm^2, i.e. after a few "shots" of the FEL, while PtSi does not even show significant damage at a hundred times higher irradiation[10]. The PtSi-photodiodes will be used for low to intermediate power densities of the FEL, starting with the spontaneous emission of the undulator. From investigations with a picosecond Nd:YLF laser at 527 nm wavelength we deduced that for pulses shorter than their response time of ≈ 500 ps the onset of saturation for PtSi-photodiodes lies around 1-2 μJ, i.e. two orders of magnitude below the saturation power of the VUV FEL. Using pinholes to reduce the cross section of the FEL beam, the range of operation of the photodiodes might be slightly extended.

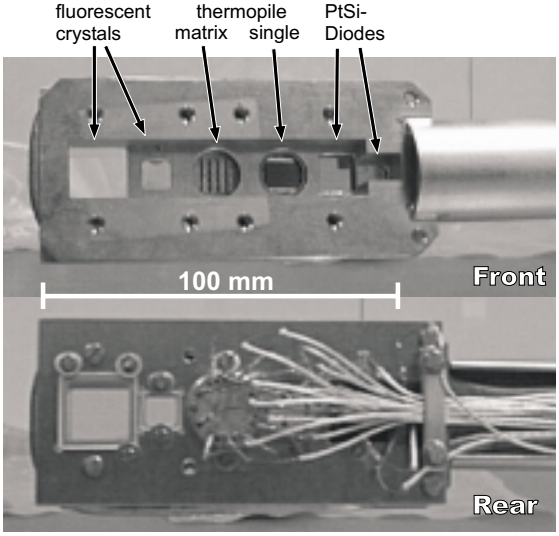

FIG. 2. *A set of detectors mounted on a water cooled Cu holder, ready for installation into the UHV chamber.*

The HTSC thermopiles fill the gap from intermediate power to saturation of the FEL (325–707 μJ in a 564 fs pulse, cf. Table I). They work at room temperature and are insensitive to temperature changes (0.5%/K). These especially designed thermopiles[11] combine a fast response time of $\approx$ 1 ns with linearity over 12 decades up to megawatts of power delivering an output signal of 1 V/mJ for short pulses. In addition to single thermopile elements, a special matrix detector with 4×4 elements, 2×2 mm^2 each (Fig. 3) has been developed for a coarse but fast measurement of the intensity distribution of individual photon pulses.

The matrix readout is done through delay lines with delays of 0, 25, 50, and 75 ns, respectively, so that each full column (4 elements) of the matrix can be combined and fed into one out of four channels of a 1 GHz digital oscilloscope (Fig. 3). Fast amplifiers are employed which also compensate for the signal drop due to the damping of the delay lines made from coaxial cables. The memory of the oscilloscope is sufficiently large to store the data from a high resolution sample of a full pulse train of 800 μs.

The detectors are complemented by fluorescence screens viewed by external CCD-cameras through Suprasil viewports. We have chosen Ce:YAG and $PbWO_4$ Crystals, because they have a fast fluorescence channel (80 ns and 2 ns lifetime, respectively), emit visible light (matching viewport transmission and camera sensitivity), and are very homogeneous, radiation hard and UHV compatible. $PbWO_4$ crystals are key materials for future use in enormous quantities in scintillation detectors for high energy particle calorimeters, e.g. at HERA (DESY) and at LHC (CERN). Like the Ce:YAG crystals[13], they have also been investigated for applications based on photon excited fluorescence[14]. The fluorescence screens are intended to be used for a coarse adjustment of the detectors and optical components with respect to the FEL beam and, in particular, to investigate the beam profile and its statistical fluctuations.

For the spectral characterisation, the photon beam is deflected by a plane mirror (Fig. 1, No. 5) into a commercial 1m normal incidence monochromator (Fig. 1, No. 7) in the right-hand branch-line. The monochromator contains a 1200 lines/mm spherical grating which will be replaced by one with 3600 lines/mm for high resolution measurements to resolve the details of the spectral fine structure. For technical reasons the latter grating is mounted on the holder at an angle in order to make the full spectral range of the Phase I VUV FEL (42-122 nm) accessible, and it is no longer possible to adjust the grating and calibrate the photon wavelength using the 0th order reflection. Therefore, a hollow cathode lamp[15] will be used for monochromator alignment and calibration: a noble gas discharge at well defined operating conditions yields a calibrated photon source covering the relevant range for Phase I FEL operation with a number of narrow lines of known flux.

The 3600 l/mm grating, in conjunction with a precise piezo-actuated entrance slit that can be closed down to less than 10 μm, results in a maximum resolving power of $E/\Delta E = 2\times10^4$ at $\lambda = 120$ nm, which should be sufficient to fully resolve the fine structure in the spectral distribution[8]. The complete FEL spectrum with a relative bandwidth of 0.3–0.5% rms can be recorded by a CCD-camera mounted in the focal plane of the spherical grating. Presently a thinned, back-illuminated UV-sensitive CCD with a pixel size of 24 μm is used[16], directly attached to the monochromator vacuum. Tests at an identical monochromator, using a laser produced plasma source with varying targets, revealed the potential of the camera (Fig. 4). This camera with its low electronic noise is ideally suited for the commissioning phase of the FEL at low to medium beam intensity.

High resolution measurements at high intensities will be carried out using a different camera equipped with a fast fluorescent screen in the focal plane of the monochromator, and a multi-channel-plate (MCP) intensifier[17]. While the pixel size of the CCD is 6.7 μm, the "effective" pixel size of the whole system (including the MCP and some lenses) amounts to $\approx$ 12 μm. This results in a spectral resolution twice as large as that of the back-illuminated CCD camera and close to the aberration limit of the monochromator. The MCP is used as a fast shutter enabling exposure times down to 5 ns. This makes it possible to select a single pulse from a sequence of pulses and to study a possible change of electron beam parameters for the first couple of bunches in a bunch train (macrobunch), even at the minimum bunch/pulse separation of 111 ns.

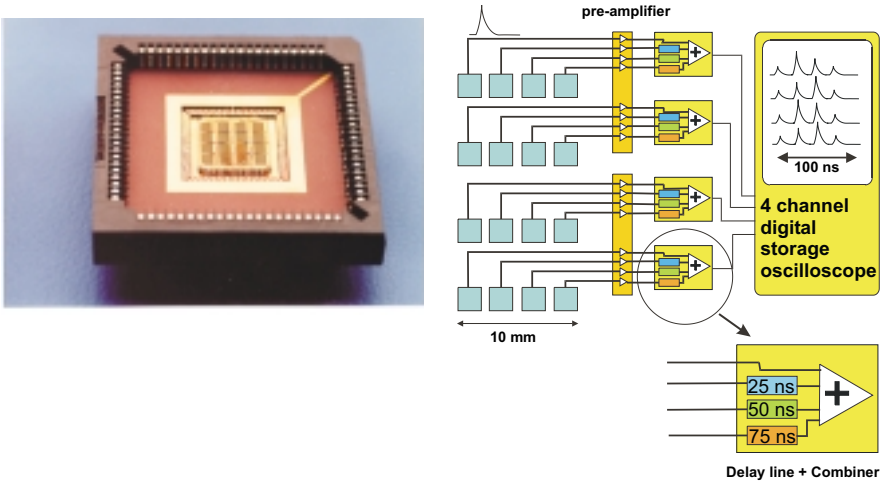

FIG. 3. *Thermopile 4 × 4 matrix detector and design of the readout scheme.*

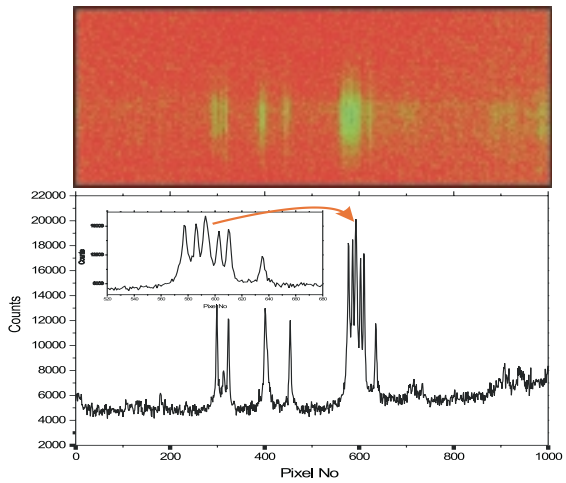

FIG. 4. *Typical spectrum of a laser produced plasma source measured with a 1 m normal incidence monochromator using a 1200 lines/mm grating and the back-illuminated CCD-camera. In this setup, the CCD covers a wavelength range of ± 10 nm, here centered around 147 nm. The experiments were performed in collaboration with the Centre for Laser Plasma Research, Dublin City University.*

The left-hand beamline (Fig. 1, No. 10) will accomodate different experiments which will be installed after the initial characterisation of the FEL beam using the diagnostics in the other two beamlines. Groups from the Research Centre Jülich and the University of Jena are presently designing two separate autocorrelation experiments to study the properties of the FEL beam in the time domain[18]. Later on it is intended to investigate the radiation damage of materials such as optical components in a specially designed UHV chamber containing a focusing mirror and time-of-flight spectrometers for electrons and ions. This experiment is in preparation at the Polish Academy of Sciences, Warszawa. The groups from Jülich, Jena and Warszawa will also be involved in the more detailed characterisation of the FEL radiation, together with groups from Dublin City University, Hamburg University, LURE (Orsay, France) and MAX-Lab/Lund Laser Centre (Lund, Sweden).

III. SUMMARY

New concepts of photon beam diagnostics have been developed to measure the unique properties of the VUV radiation from a SASE FEL on a single pulse basis. A variety of detectors is employed to cover the full range of intensity from spontaneous undulator emission to SASE in saturation. Apart from the photon beam diagnostics task this will also be a benchmark experiment for several new types of detectors. The knowledge gained with the present setup will be very valuable to develop instrumentation for online photon beam characterisation which is indispensable at future FEL user facilities.

ACKNOWLEDGEMENTS

The authors would like to thank Frank Ruhl for his contributions in the early stages of the project and G. Zimmerer for lending his 1 m normal incidence monochromator. We gratefully acknowledge many stimulating discussions with E. L. Saldin, E. A. Schneidmiller, M. V. Yurkov, and many other colleagues involved in the FEL project at DESY.

[1] A VUV Free Electron Laser at the TESLA Test Facility at DESY, Conceptual Design Report, DESY Print, June 1995, TESLA-FEL 95-03; J. Roßbach, Nucl. Instr. and Meth. A **375** (1996) 269
[2] A. M. Kondratenko and E. L. Saldin, Part. Acc. **10** (1980) 207
[3] Ya. S. Derbenev, A. M. Kondratenko, and E. L. Saldin, Nucl. Instrum. and Meth. **193** (1982) 415
[4] R. Bonifacio, C. Pellegrini and L. M. Narducci, Opt. Commun. **50** (1984) 373
[5] C. Pellegrini, J. Opt. Soc. Am. **52** (1985) 259
[6] J. Roßbach, E. L. Saldin, E. A. Schneidmiller, and M. V. Yurkow, Nucl. Instrum. and Meth. A **393** (1997) 152
[7] E. L. Saldin, E. A. Schneidmiller, and M. V. Yurkow, Nucl. Instrum. and Meth. A **393** (1997) 157
[8] E. L. Saldin, E. A. Schneidmiller, and M. V. Yurkow, Opt. Commun. **148** (1998) 383
[9] B. Faatz, J. Feldhaus, J. Krzywinski, E. L. Saldin, E. A. Schneidmiller, and M. V. Yurkov, DESY Print TESLA-FEL 97-07 (1997)
[10] K. Solt, H. Melchior, U. Kroth, P. Kuschnerus, V. Persch, H. Rabus, M. Richter, and G. Ulm, Appl. Phys. Lett. **69** (1996) 3662
[11] patented design, FORTECH HTS GmbH, D-93170 Bernhardswald, Germany, for details see: M. Kauf, S. Schuberth, J. Hutfless, J. Betz, S. Zeuner, and H. Lengfellner, Laser Magazin **5**, (1994) 12 (in German)
[12] S. Zeuner, W. Prettl, and H. Lengfellner, Appl. Phys. Lett. **66** (1995) 1833
[13] C. M. Wong, S. R. Rotman, and C. Warde, Appl. Phys. Lett. **44** (1984) 1083
[14] A. N. Belsky, V. V. Mikhailin, A. N. Vasil'ev, I. Dafinei, P. Lecoq, C. Pedrini, P. Chevallier, P. Dhez, and P. Martin, Chem. Phys. Lett. **243** (1995) 552
[15] K. Danzmann, M. Günther, J. Fischer, M. Kock, and M. Kühne, Appl. Opt. **27** (1988) 4947; see also http://www.pmp.uni-hannover.de/arbeitsgruppen/Gruppe-Kock/Kock_Gruppe_engl.html
[16] CCD camera system ATC 300 L from Photometrics, Tucson, Arizona 85706
[17] CCD camera Nanostar S25 from LaVision, Göttingen, Germany
[18] B. Sonntag, J. Feldhaus, HASYLAB Annual Report 1997, pp. 95

Wakefield induced correlated energy spread and emittance growth at TTF FEL

Feng ZHOU, Martin DOHLUS

DESY-MPY, Notkestr.85, 22603 Hamburg, Germany. E-mail:zhouf@mail.desy.de

Abstract

An electron beam with a small energy spread (0.1%) and a small normalized emittance (2 mm.mrad) is required to drive a Free Electron Laser at the TESLA Test Facility (TTF) at DESY [1]. During FEL operations, the longitudinal and transverse wakefields which are generated by vacuum components, principally by RF cavities, bellows and valves, will induce an additional energy spread and emittance growth, respectively. This paper presents the wakefields and its induced correlated energy spread and emittance growth at the TTF FEL of phase I and phase II.

1. Correlated energy spread due to longitudinal wakefield

1.1 Longitudinal wakefield

The longitudinal wakefield of main vacuum components at TTF Linac except the undulator pipe, e.g, RF cavities, bellows and valves, is estimated in this section. The wakefield of undulator pipe has been calculated in detail [2].

1.1.1 TESLA cavity

TESLA superconducting cavities are used to accelerator the beam along TTF linac. One cryomodule is composed of 8 cavities, one of which is composed of 9-cell cavity. At TTF linac the bunch length is shortened initially from 2 mm to 0.8 mm by the first stage bunch compression, from 0.8 mm to 0.25 mm, and finally from 0.25 mm to 0.05 mm by the second and third stage bunch compression, respectively. For the cavity wakefield with the bunch larger than 1 mm, the field pattern of the first cavity is almost the same as the eighth one, and thus the wakefield of the first cavity is equal to the eighth one. However, for shorter bunches, the field pattern changes tremendously after a passage through a cavity. Obviously, the wakefield of the first cavity is different from the eighth one with the shorter bunch. In this case, its wakefield of the first 3 cavities are directly calculated by MAFIA, while the following 5 cavities are obtained from the green function [3]:

$$W_{11}{}^{\delta}(s) = 38.5(1.18\times\exp(-0.577\sqrt{s}) - 0.18) \qquad (1)$$

where s is the distance from the point charge. The wakefield of the bunch can be derived from the wake green function by:

$$W_{11}(s) = \int \rho(s')\cdot W_{11}{}^{\delta}(s-s')ds' \qquad (2)$$

where $W_{11}(s)$ is the wakefield of the bunch, $\rho(s)$ is the bunch distribution. Such approximations are reasonable since the difference of the energy spread induced by the cavity #3 and #8 is only about 5% [4].

1.1.2 Bellows and valves

There are several types of bellows in the TTF Linac with different number of waves and different beam pipe radius. Its wakefield with 4 waves are easily calculated by MAFIA. The wakefield of other types bellows can then be simply scaled from it, since its wakefield is linear with the number of the waves and inverse to the square of the beam pipe radius.

A valve in the TTF linac beamline is like a rectangular cavity when it is open. The structure of the valve used in the calculation is simplified with a square cross-section and a gap of 25 mm. In the calculations, the square cross section of the outer valve pipe can be considered as the circular one, since the corners contribute less to the wakefield. One has studied the wakefields of the bellows and valves in detail [4].

1.2 Correlated energy spread

The correlated energy spread due to the longitudinal wakefield is:

$$\delta E = qe\sqrt{\int ds \cdot \rho(s) \cdot W_{11}{}^2(s) - k_{11}{}^2} \qquad (3)$$

where k_{11} is the loss factor. The loss factor and its correlated energy spread are presented in Table 1.

Table 1: The loss factor and its energy spread

Vacuum components	k_{11} (V/pC)	δE (keV)
cavity (phase I)	321.7	102.1
cavity (phase II)	1314.2	502.1
Bellows (phase I)	128.6	64.3
Bellows (phase II)	532.6	266.3
Valves (phase I)	19.8	9.89
Valves (phase II)	59.8	29.89
Energy spread (phase I)	0.05%(380 MeV)	
energy spread (phase II)	0.08% (1.0 GeV)	

2. Transverse wakefield induced emittance growth

The emittance growth due to the wakefield can be expressed as [5]:

$$\gamma\Delta\varepsilon_x = \frac{< x >^2 L \cdot < \beta >}{2\gamma(0)G_f}\left(\frac{e^2 N_e W_\perp(z)}{m_0 c^2}\right)^2 \qquad (4)$$

where $\gamma\Delta\varepsilon_x$ is the normalized transverse emittance, $< x >$ is the accelerating structure transverse offset in unit of meter, L is the structure length (m), $< \beta >$ is the betatron function (m), $\gamma(0)$ is the normalized initial energy, $W_\perp(z)$ is the transverse wakefield per unit length at the tail of the bunch, usually at $2\sigma_z$ in unit of V/pC/m/m, and G_f is given by:

$$G_f = (\gamma(s)/\gamma(0) - 1)/s,$$

where s is the total length of accelerating structures. In the TTF Linac, the beam is accelerated from the initial energy 5 MeV to the final 1.0 GeV with the accelerating gradient of 15 MV/m. The accelerating length of one cavity is 1 m, and the average beta function is about 10 m and $W_\perp(2\sigma_z) = 76$ V/pC/m/m at $\sigma_z = 2$ mm. Substituting these parameters into Equation (4), the emittance growth induced by the transverse wakefield is:

$$\gamma\Delta\varepsilon_x = 2.75\times10^{-3} < x >^2 \text{ (m.rad)} \qquad (5)$$

Considering the beam offset 1 mm and cavity offset 1 mm, the emittance growth is about 1.2%, which agrees well the tracking results [1].

3. Dispersion induced emittance growth

For simplicity we consider a longitudinal positions s with maximum dispersion ($\eta' = 0$). Its emittance can then be written as:

$$\varepsilon = \varepsilon_0 + \Delta\varepsilon_{wf}(s) + \Delta\varepsilon_{disp}(s)$$

where the second term in the right side of the equation is the wakefield induced emittance growth, and the third term is the dispersion induced emittance growth, which can be calculated as follow:

$$\Delta\varepsilon_{disp} \approx \frac{\eta^2(s)\cdot\delta^2(s)}{< \beta >}$$

where η is the centroid dispersion, δ is the energy spread, and $< \beta >$ is the beta-function. In the TTF FEL, since $\delta \approx 0.1\%$, $< \beta >\approx 10$ m, and the dispersion is very small, obviously the dispersion induced emittance growth can be neglected.

4. Summary

The correlated energy spread of TTF Linac except undulators is below 0.1% and its transverse wakefield induced emittance growth is near 1.0%.

REFERENCES:

[1]. VUV free electron laser at the TESLA Test Facility at DESY, TESLA-FEL 95-03, 1995.
[2]. M.Dohlus, et al., Estimation of longitudinal wakefield effects in the TESLA-TTF FEL undulator beam pipe and diagnostic section, TESLA-FEL 98-02, 1998.
[3]. A.Novokhatski et al., wakefield dynamics in quasi periodic structures, EPAC98, 1998.
[4]. F.Zhou, wakefield induced energy spread and emittance growth at TTF FEL, TESLA-FEL 99-05.
[5]. J.Gao, Analytical treatment of the emittance growth in the main linac of future colliders, LAL-SERA-99-82

Emittance calculations for the TTF FEL injector

Feng ZHOU

DESY-MPY, Notkestr.85, 22603 Hamburg, Germany. e-mail: zhouf@mail.desy.de

Abstract

The Free Electron Laser at the TESLA Test Facility (TTF FEL)[1] [2] is based on the principle of the so-called self amplified spontaneous emission, which requires an electron beam with very high phase space density. In order to meet the requirements an rf gun is under test at DESY. In this paper the emittance of the electron beam as function of the charge is investigated by means of PARMELA simulations. The effect of solenoid offset and of beam offsets at the cathode onto the beam emittance is discussed. The emittance growth due to field unbalance in the gun is mentioned and the frequency difference between π-mode and 0-mode as function of the field balance is presented.

1. Emittance with different bunch charge

The design bunch charge for the FEL operation is 1 nC. However, experiments will be made also with other bunch charges. PARMELA simulations were carried out to find scaling laws for the transverse and longitudinal emittance in the range of 0.5-8 nC bunch charge. The TTF FEL photoinjector consists of a 1.5 cells RF gun, a focusing solenoid which surrounds the full cell for the compensation of emittance blow up, and the capture cavity which is a 9-cell superconducting cavity for the further acceleration and focusing of the bunch. The bucking coil behind the RF gun is used to compensate the solenoid field on the cathode. Our emittance calculation is up to 355 cm from the cathode, since the emittance is close to the minimum value at this point. Table 1 lists the PARMELA settings.

Table 1: The PARMELA settings

bunch charge	0.5-8 nC
initial bunch radius at the cathode	1-5 mm
RMS laser pulse length (gaussian)	5 ps
maximum accel. grad. at the cathode	50 MV/m
aver. accel. grad. in the capture cavity	12 MV/m

Using these settings and then optimizing the phases of the RF gun and the capture cavity, one can obtain the energy at the exit of the RF gun and the capture cavity of, 5.3 MeV and 16.4 MeV, respectively. The optimized transverse and longitudinal emittances for a longitudinal gaussian laser pulse are as:

$$\varepsilon_{x,y} = 2.015Q + 0.024\,(\text{mm.mrad}),$$

$$\varepsilon_{z} = 27.13Q^{0.493}\,(\text{mm.keV}),$$

where the $\varepsilon_{x,y}$ and ε_z mean the normalized transverse emittance and longitudinal emittance, respectively, and Q is the bunch charge in unit of nC.

2. Emittance and beam offset vs transverse solenoid offset

2.1 Emittance vs transverse solenoid offset

The longitudinal magnetic field of the focusing solenoid at the transverse offset can be expressed as:

$$B_z(r) = B_z(0) - \frac{1}{4}\left.\frac{\partial^2 B_z}{\partial z^2}\right|_{r=0} \cdot r^2 \qquad (1)$$

The second order term component in equation (1) is of small magnitude. Especially at the cathode $\frac{\partial^2 B_z}{\partial z^2} \approx 0$, since Bz is almost linear in z due to the solenoid-bucking coil arrangement. Therefore, from the qualitative analysis the longitudinal magnetic fields with and without a transverse offset are equal. And, the transverse magnetic field with a transverse offset $B_r(r) \propto r$. Applying the Liouville theorem, the phase space should be kept constant in such linear field. It is also shown in the PARMELA simulations that both the transverse and longitudinal emittances with different transverse solenoid offsets is the same as that of no solenoid offset, respectively.

The transverse wakefield effects on the emittance dilution have been neglected due to the low RF frequency of the TTF cavity and hence the weak wakefield.

2.2 Transverse beam offset vs transverse solenoid offset

The transverse magnetic field at different transverse offset is proportional to the transverse offset and the transverse force can result in a transverse shift of the bunch. PARMELA simulation results show the beam transverse position vs transverse solenoid offset, as listed in Table 2. It is shown that the beam transverse offset at 355 cm is amplified from the exit of the RF gun. These can be explained as follows: In the solenoid field region, due to $B_r(r) \propto r$, there exists a transverse momentum p_r, which will result in a small angle, $\theta = \frac{p_r}{p_z}$, where p_z is the longitudinal momentum. In the drift beam line between the RF gun exit and the beginning of the capture cavity, the solenoid field gradually decreases down to zero, but the smaller angle still exists in the rest of the drift where the solenoid field is zero.

Table 2 beam offset vs transverse solenoid offset

	Beam offset at 355 cm	
Sole. Offset (mm)	Horizontal (mm)	Vertical (mm)
0.2	0.7	0.7
0.8	3.0	3.0

If the angle is θ and the length of rest drift is l_0, the transverse beam shift $\propto l_0 \cdot \theta$. Therefore, only if the angle is constant in the rest drift, the transverse bunch shift is larger at a longitudinal position far from the cathode.

3. Emittance vs transverse bunch offset at the cathode

If the bunch has a transverse offset from the axis at the cathode, what about its emittance growth? According to the MAFIA TS3 simulations, the transverse emittance at the exit of the RF-gun is almost not changed, i.e., the emittance growth is only below 5.0%, when the initial bunch transverse offset at the cathode is below 10 mm. When the initial bunch transverse offset is larger than 20 mm, the bunch can not be monitored at the exit of the RF gun in the simulations. In this case, the bunch may hit the iris of the RF gun due to the limited iris radius of 25 mm. In such case, the longitudinal electric field is not changed and the transverse field is linear with the offset. Therefore, the phase space is near constant.

4. RF field uniformity of the RF gun and its correlated emittance growth

In order to minimize the emittance growth in the RF gun, the ratio of the π-mode field in the half cell (E_h) to the full cell (E_f) should be kept around 1.0 at the resonance frequency [1]. If the field amplitude in the half cell is different from the one in the full cell, the emittance might blow up due to the discontinuous RF field. Simulations show that $E_h / E_f = 1 \pm 0.25$ will cause larger than 75% emittance growth [3].

The field balance can not be directly monitored during operation, however, the field ratio E_h / E_f is related to frequency difference between the π and zero modes, $\Delta f_{0\pi}$, which can be directly measured during operation. Thus, in order to monitor the field balance it is useful to build up the relation between $\Delta f_{0\pi}$ and the field ratio E_h / E_f. With MAFIA, the curve of the field uniformity uf $(=(|E_h|-|E_f|)/(|E_h|+|E_f|))$ with $\Delta f_{0\pi}$ is shown in Figure 1.

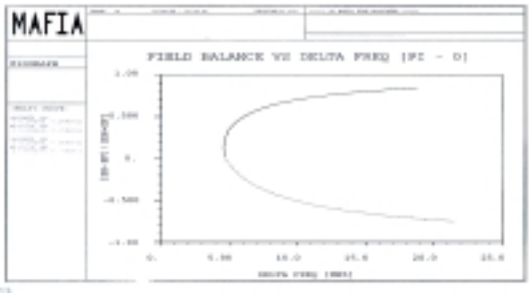

REFERENCES:

[1]. VUV free electron laser at the TESLA Test Facility at DESY-Conceptual design report, DESY Print June 1995, TESLA-FEL 95-03.

[2]. M.Zhang, The TESLA free electron laser, The 1st ACFA conference, KEK, 1998.

[3]. M.Zhang, private communication, Sep.1998